LBL-30843

Lawrence Berkeley Laboratory
UNIVERSITY OF CALIFORNIA

Materials & Chemical
Sciences Division

Studies on the Development of Mossy Zinc Electrodeposits from Flowing Alkaline Electrolytes

L. Mc Vay
(Ph.D. Thesis)

July 1991

Prepared for the U.S. Department of Energy under Contract Number DE-AC03-76SF00098

DISCLAIMER

LBL- 30843

Studies on the Development of Mossy Zinc Electrodeposits from Flowing Alkaline Electrolytes

Laura Mc Vay
Ph.D. Thesis

Chemical Engineering Department
University of California

and

Chemical Sciences Division
Lawrence Berkeley Laboratory
University of California
Berkeley, CA 94720

July, 1991

This work was supported by the Assistant Secretary for Conservation and Renewable Energy, Office of Transportaion Technologies, Electric and Hybrid Propulsion Division of the U. S. Department of Energy under Contract No. DE-AC03-76SF00098.

Studies on the Development of Mossy Zinc Electrodeposits from Flowing Alkaline Electrolytes

Laura Mc Vay

(PhD thesis)

Lawrence Berkeley Laboratory
and
Chemical Engineering Department
University of California at Berkeley,

ABSTRACT

The initiation and characteristics of mossy zinc electrodeposits have been investigated. Batteries with zinc electrodes are candidates for electric vehicle applications; however, this electrode is prone to form non-compact deposits that contribute to capacity loss and battery failure. Moss is deposited when the current density is far from the limiting current. This morphology first appears only after the bulk deposit is approximately 1 μm thick. In this investigation, the effects of flow rate (Re= 0- 4000), current density (0-50 mA/cm^2), concentration of the the electroactive species (0.25 and 0.5 M), and the concentration of supporting electrolyte (3, 6, and 12 M) on the initiation of moss were examined. The rotating concentric cylinder electrode was employed for most of the experiments; and a flow channel was used to study the development of morphology. After the experiment, the deposit was characterized using microscopic, x-ray diffraction, and profilometric techniques.

Moss is distinguished by a loose conglomeration of elongated crystals having a porosity of about 90%, independent of the deposition conditions. Transmission electron microscopic observations show that the moss consists of zinc crystals with no oxide inclusions. With increasing deposit thickness, the average roughness of the zinc compact layer rises to about 10 μm and the roughness wavelength declines to about 50 μm, after which the morphological type changes from flat to mossy. The mossy structure begins to grow both around large protrusions and in the crevices between growing crystal grains. X-ray diffraction data show that the fraction of the $\{10\bar{1}3\}$ and $\{0002\}$ crystal habits increase drastically when moss is

initiated. Once moss appears, a change in the deposition conditions doesn't reverse the morphology to a compact deposit; however, the transition from compact to mossy deposit formation can be delayed by an increase in the current density if moss hasn't yet formed. Videomicroscopy provides evidence that the initiation period of moss is short; subsequently, the islands of moss cover the surface.

The transition from a compact to a mossy texture is influenced by process conditions. Generally, any change in the deposition parameters that increases the average surface roughness will simultaneously promote the initiation of mossy zinc. Decreasing the zincate concentration or increasing the supporting electrolyte concentration ([KOH]) promotes mossy zinc growth. At a constant fraction of the limiting current, moss appears more readily when the current density is low. When the fraction of the limiting current is kept constant, raising the current density and the flow rate delays the onset of mossy growth.

Poor mass transport and a surface topography dominated by large protrusions favor the initiation of moss. When zinc is reduced from basic electrolytes, hydroxide ions build up at the electrode, particularly between growing protrusions, and affect the reaction parameters. This change in the kinetic and thermodynamic properties of the zinc deposition reaction results in the initiation of moss. Finally, once mossy zinc nodules become large (20-40 μm), they become sinks for current preventing further growth of the compact layer.

ACKNOWLEDGEMENTS

Many years ago, I performed an exercise in which I was given 24 hours of complete freedom. There was only one catch: I could not impinge upon anyone else's right to live as they wished. I found that there was nothing that I could do that would not compromise other's liberties. During this thesis, I have compromised many people's freedoms, and at this time, I would like to acknowledge them.

First of all, I would like to thank my family, who forgave me for the tax deduction that they lost on account of my late birth, who raised me through my adolescence, and who put up with me through my extended adolescence. Yes, I have finally grown up. Well, maybe.

I would also like to thank Professors Tobias and Muller for their financial support and helpful discussions on topics ranging from research to my weight. The members of the Tobias/Muller group past and present, have provided me with a collegial and all too pleasant atmosphere to work in.

I would never have survived this thesis if it had not been for my friends who kept me sane. Thanks to Steve and Kathryne Oliphant for their unconditional love. Thanks also to Eileen Burke, Steve Sabram, Steve Frezza, Larry Feinberg, Jennifer Anderson, Stewart Howe, Craig Carter, Lee Carter, Tom Huguenin, and Fred Hollander.

I also appreciated the efforts of the LBL support staff, who were always available for consultations and to bail me out when I got into trouble. Thanks especially to staff scientists Crispin Heatherington for his help with the TEM and Dan Schwartz for his help with RAMAN.

This work was supported by the Assistant Secretary for Conservation and Renewable Energy, Office of Transportation Technologies, Electric and Hybrid Propulsion Division of the U. S. Department of Energy under Contract No. DE-AC03-76SF00098.

TABLE OF CONTENTS

INTRODUCTION

Zinc is crucially important to modern society, because of its easy availability, low cost, and negative standard potential (-0.76 V). Since ancient times, this metal has been employed by man in applications such as brass manufacture. In the last two centuries, cathodic protection, galvanizing, and die casting processes as well as use in primary batteries, have caused the demand for zinc to increase. Most recently, the development of electric cars and novel electrochemical storage applications has sparked interest in rechargeable zinc batteries(1). However, zinc readily forms undesirable dendritic and mossy deposits, which are detrimental to battery performance.

1.1 Purpose and Scope of This Study

Shape change is a major cause of failure in alkaline, zinc secondary batteries. An important component of this phenomenon is the formation of a porous deposit known as mossy or spongy zinc(2). This morphology is initiated only after the passage of a substantial amount of charge even when the process parameters are kept constant. A factor in the initiation of mossy zinc may be a local change in the deposition conditions that results in the formation of a crystal habit more favored for growth. One goal of this research was to investigate the questions of why the morphology changes and how the morphology changes. The crystal structure was characterized on a microscopic scale, to augment the comprehension of roughness development.

The use of electrolyte flow results in lowered battery size and greater efficiency. In these cells, forced convection dominates any effects of natural convection and diffusion. A continuous supply of reactant is provided to the electrode, thereby maintaining steady state conditions on the electrode side. It is known that the morphology of the electrodeposited zinc is

dependent on the interfacial concentration and on the mass transport conditions (1). By using appropriate combinations of flow rate, concentration, and current density, it is possible to vary the interfacial concentration of the zincate electroactive species. In this investigation, the effects of flow rate, current density and concentration of the the electroactive species and the supporting electrolyte were examined. The development of morphology was observed in-situ using videomicroscopy. After the experiment, the zinc electrodeposit was characterized using electron microscopy, x-ray diffraction, and profilometry.

1.2 Aspects of Zinc Chemistry

Zinc is a member of group IIb of the periodic table, a group that also includes cadmium and mercury. The electronic configuration of zinc in the metallic form is $[Ar]4s^2 3d^{10}$. When ionized, zinc loses electrons from only the 4s orbital; therefore, ligand bonds with this metal do not use the d orbitals, and hence zinc is not considered a transition metal(3). The members of group IIb are softer and melt at a lower temperature than the coinage metals, copper, silver, and gold (3). The reduction potentials of zinc and cadmium (-0.76 V and -0.40 V vs. SHE) are considerably more negative than their nearest neighbors, copper and silver; however, the reduction potential of mercury, the third member of the IIb group, is very high (0.79 V vs. SHE). The bonding observed with zinc(II) and cadmium(II) ions parallels the behavior of Mg^{+2}, rather than that of copper and silver.

Because the +1 electronic configuration ($[Ar]4s^1 3d^{10}$) is highly unstable, only the zinc(II) oxidation state is important. The existence of the univalent state of zinc as Zn_2^{+2} has been reported, but not confirmed, although the mercury(I) ion has the same configuration. No stable compounds or complexes of Zinc(I) have been found (3).

Although the bonding of the group IIb metals is different, zinc resembles the transition metals in its ability to form compounds and complexes. Like the transition metals, zinc forms

stable compounds with halogen, oxygen, cyanide, sulfate, and chlorate ions(3). The primary coordination number of zinc is 4, and because the d orbitals remain filled, no higher coordination numbers are known(3). Zinc forms tetrahedrally coordinated complexes that enhance the solubility of zinc salts in both alkaline and acidic media. A distribution diagram of the alkaline zinc complexes, taken from Mc Breen and Cairns (1), is shown in Figure 1.1. Zinc complexes are generally weaker than those of the transition metals, because the d orbitals are not used in bonding, and no complexes form with carbonyls, nitrosyls or olefins, even though these groups bond with the transition metals.

1.3 Zinc Crystallography

The unit cell of zinc is a hexagonally close packed (hcp) structure, shown in Figure 1.2. The unit cell dimensions are c=4.94Å and a=2.66 Å (4), giving a c/a ratio of 1.85, a value substantially larger than that reported for most hcp metals, 1.62. This larger c/a ratio establishes that the zinc unit cell is elongated in the direction of the c axis and/or more closely packed in the basal plane, implying that anisotropy may exist in the crystal growth behavior of zinc (4). This anisotropy is evidenced by the differences in crystallization potential of the different planes of zinc, which are shown in Table 1 (5, 6). Each zinc atom has twelve nearest neighbors, six on the basal plane at a distance of 2.66 Å, three above and three below the basal plane at a distance of 2.91 Å. Because the atoms are closer together in the basal plane, the metallic bonds in this plane are stronger than those between hexagonal planes.

As the stacking sequence in zinc is ABABABAB, only extrinsic stacking faults bounded by partial dislocations are formed. Previous studies have shown the existence of several types of crystal imperfections including twins, interstitial atoms, vacancies, and dislocations.

Figure Captions

1.1 Distribution of the zinc hydroxide complexes with hydroxide concentration, after (1).

1.2 Schematic of the zinc crystal lattice; c = 4.94 Å and a = 2.66 Å.

Table 1- Approximate equilibrium potential differences (mV) between various zinc crystal surfaces in hydroxide electrolytes, after (5)

surface	amalgamated	1011	1211	0001	1010	1120
potential difference with respect to polycrystalline	0	+8	+4	+1	0	-2

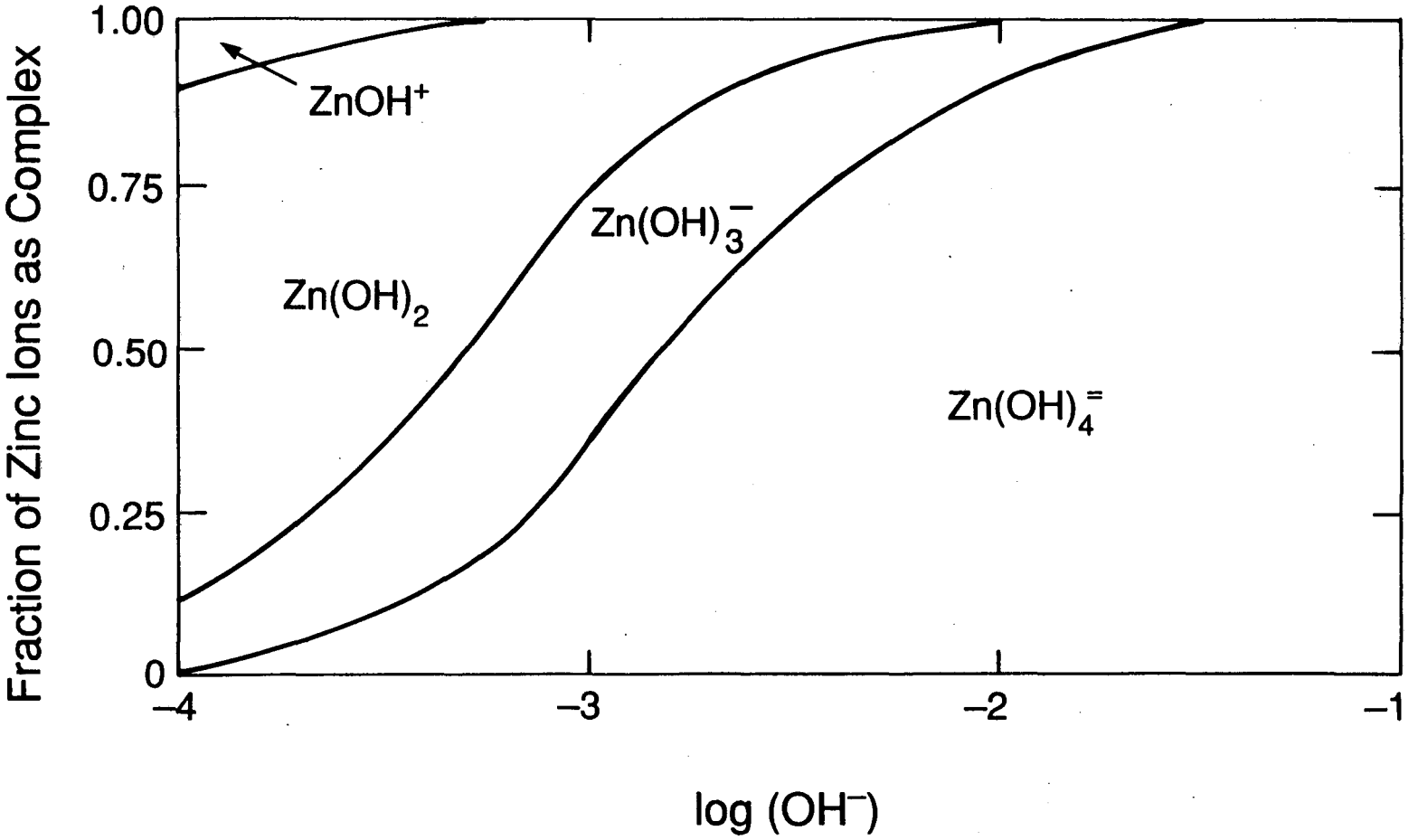

XBL 905 – 6378

Figure 1.1

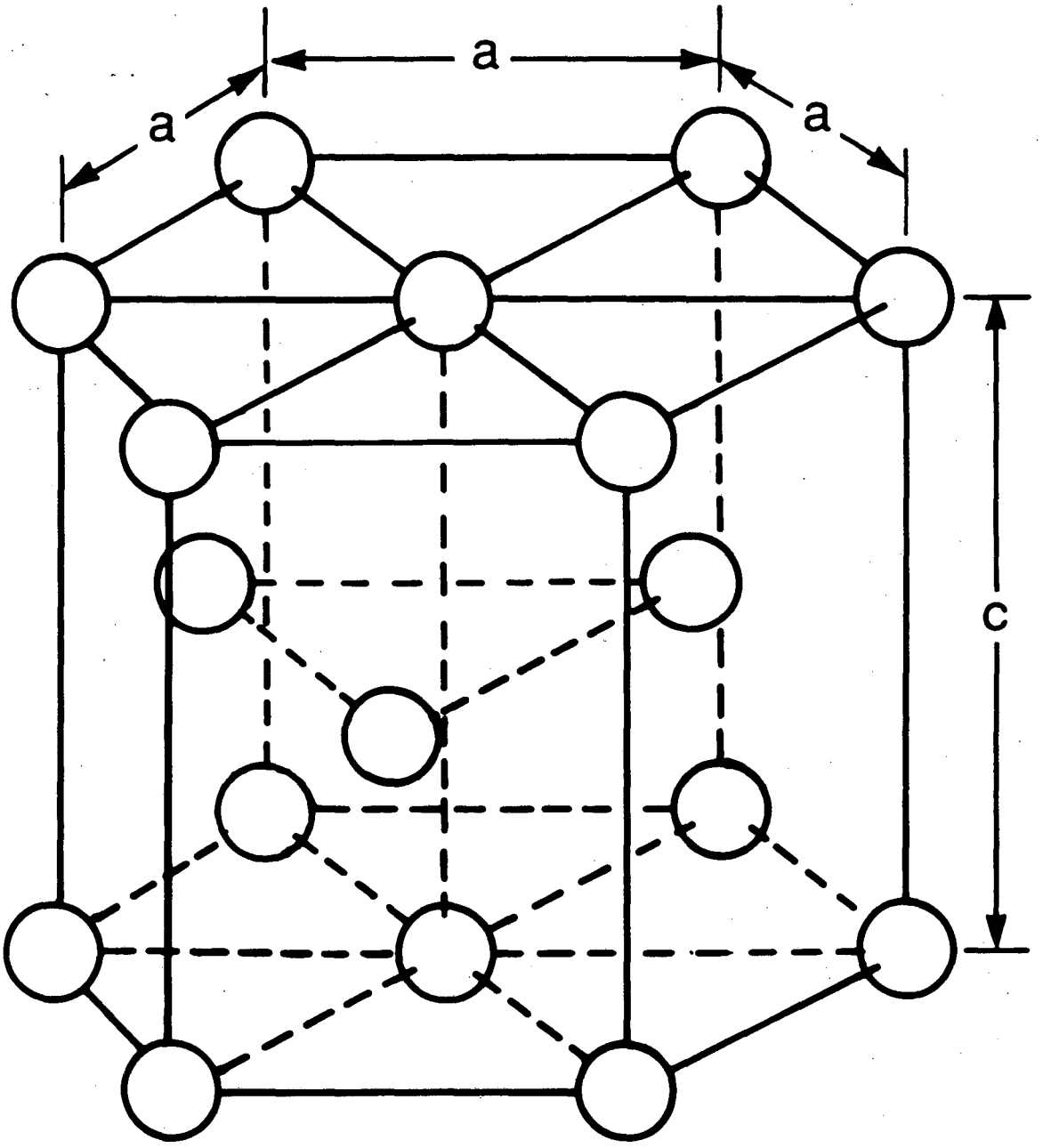

XBL 905-6379

Figure 1.2

LITERATURE REVIEW

2.1 Special Aspects of Electrocrystallization

Crystallization from a vapor and electrocrystallization from solution are distinctly different operations. In the deposition of a metal from the vapor phase, metal atoms adsorb on the surface, diffuse to a kink site and are incorporated into the crystal lattice, as shown in Figure 2.1 (a) (7). In electrocrystallization, complexed or solvated ions deposit at kink site, *after* charge transfer occurs, and frequently, the electroactive species is not the dominant complex in solution. Characteristically, electrochemical systems contain a double layer at the metal/electrolyte interface, and surface active agents (e.g. additives) may also be adsorbed on the surface (both of which are shown in Figure 2.1 (7)). For charge transfer to occur, all layers must be displaced, and if the anion is strongly adsorbing at kink sites, the metal ion may have to deposit at a less favorable site causing a change in crystal orientation. Changing the supporting anion (e.g. from Cl^- to OH^-) may influence the overpotential required for deposition depending on either the strength of complex adsorption or if the counter ion adsorbs.

2.2 The Deposition of Mossy Zinc From Alkaline Electrolytes

The formation of mossy or spongy zinc electrodeposits is not a novel question, as these types of deposits were reported in the literature as early as 1903(8). More recently, however, the need for high specific power, high specific energy batteries has resulted in renewed interest in this problem.

The deposition of non-compact layers can be either beneficial or detrimental to battery performance. Ideally, the formation of an even, adherent porous plate is desirable when charging, because the average current density is reduced, and it is possible that the cycle life

can be extended. Although normally a decreased current density is beneficial to the cycle life of the battery, mossy zinc is non-adherent, and the capacity loss caused by the detachment of zinc from the cathode far outweighs any possible increase in cycle life(9).

Sponges encompass a wide variety of morphological types and they form in the electrodeposition of a number of metals (10). Moss is created at low rates of convection at both high and low current densities. The case of sponge formation at high current densities was discussed extensively by Ibl(11) and is clearly a mass transport limited situation; therefore, it will not be discussed here further. The low current density case represents an unusual situation. Under these conditions, a smooth deposit is expected because the crystal growth is dominated by 2 dimensional nuclei formation and the extension of layers. When moss is formed, the roughness decreases with increasing current density, contrary to expectations. This situation is also unique because at low current densities, moss occurs only in the electrodeposition of zinc and cadmium (for a further discussion of cadmium moss, see Appendix 3).

2.3 Early Studies on Zinc Moss Formation

Wranglen (10) found that spongy zinc deposits appeared under three sets of conditions: (1) in acids at high current densities and room temperature, (2) in neutral solutions at low current densities and elevated temperatures, and (3) in alkaline media at high current densities and low temperatures. Under conditions (1) and (3), sponge was alleged to be initiated because of cation depletion, a reasonable conclusion. In the case of type (1) or type (3) sponge, the tendency toward moss formation was lessened as the current density was lowered and the temperature raised. No explanation was offered for type (2) sponge.

Naybour(12) performed a systematic study of zinc deposition onto single crystal zinc substrates, using current densities from 4-100 mA/cm^2 and stagnant electrolytes. For all of the crystal surfaces the trend in morphology was the same. At both high and low current

densities, the deposit was very rough, and there was a small intermediate range in which the deposit was smooth. In the current density range in which moss was obtained, the density of the moss nodules varied with the crystal plane by several orders of magnitude, being 10^3 nodules/cm^2 on either a $\{0001\}$ or a $\{10\bar{1}0\}$ type of plane. When a $\{11\bar{2}0\}$ plane was the substrate, the density of moss was 10^5 nodules/cm^2.

In an extension of the above study, Naybour (13) considered the effect of flow on the morphology of electrodeposited zinc and found that forced convection greatly modified the deposit structure, presumably because of improved mass transport to the electrode surface. Three types of morphology were obtained: (1) flat, which included mossy growth, (2) bulbous, a type that is not found in stationary electrolytes, and (3) dendritic. The threshold above which moss is not obtained was approximately a linear function of the Reynolds' number. Interestingly, the ratio of protuberance height to deposit thickness appeared to be an inverse function of the current density until mass transport limited conditions were reached.

Arouete and co-workers(9) deposited zinc galvanostatically from a highly alkaline potassium hydroxide electrolyte to investigate the effects of pulsing and current reversal on the onset of moss. When the current was pulsed and the pulses were small in magnitude, the deposit was initially compact but later became mossy. Once the deposit morphology changed, the adherency decreased markedly. When the current density exceeded a critical value, the experimental results were dependent on the pulse length. When the pulse length was greater than 10 milliseconds, dendritic deposits were obtained, probably because of cation depletion. Shorter pulse lengths resulted in compact deposits. Using periodic current reversal, a relatively even deposit was obtained, although only a small net cathodic charge was passed. The authors concluded that the absence of moss when pulses and current reversal were used resulted from the dissolution of the active mossy deposit during the anodic periods. However, only small quantities of charge were passed, and it cannot be said with certainty that moss would not have been formed at a later time.

Different results were obtained by Mc Breen and co-workers(14) who studied the effects of square wave pulsed current on the morphology. Superimposition of alternating current (AC) on a low direct current (DC) enhanced the formation of moss. When AC was imposed on higher DC currents, no change in morphology was observed.

2.4 Theories of Mossy Zinc Deposition

Several theories have been proposed to explain why zinc moss is produced, although none can completely account for the experimental observations. An interesting clue to the formation of mossy zinc lies in the fact that the conditions under which mossy zinc is formed are very different from the circumstances under which sponges of other metals are produced, with the sole exception of cadmium. In contrast to powder deposition, moss forms in current density ranges in which the deposition is *clearly* kinetically controlled. *This type of morphology only appears after the passage of a substantial amount of charge, so the deposit initially forms a "compact layer" on top of which moss is initiated.* Zinc sponges are initiated with both flowing and non-flowing electrolytes; the magnitude of the fluid velocity can determine the loading at which the transition from a compact to a mossy deposit occurs(13). Deposition using pulsed current or current reversal affects the initiation of moss, although the use of modified charging methods does not necessarily suppress sponge formation.

It has been said (2, 15-19) that moss forms at points on the cathode where colloidal zinc salt particles are deposited. These basic hydroxide salts can be introduced into the electrolyte in three ways: (1) at the anode because of corrosion mechanisms caused by inhomogeneities in the anode surface, (2) at the cathode because of the change in pH caused by hydrogen evolution, (3) by differential aeration at the cathode, that would cause corrosion of the zinc deposit. Kudryavtsev (15-19) hypothesized that colloids formed at the anode would migrate toward the cathode by electrophoresis.

This hypothesis is supported by the following experimental observations(2): (1) moss is not formed at low current densities if an insoluble anode and purified solutions are used; (2) moss is formed if zinc dust is added to the electrolyte; (3) moss is initially formed at the air/electrolyte interface; (4) there is no change in overpotential; (5) small amounts of noble metals inhibit moss formation. However, later workers disputed all of Kurdyastev's observations. Other workers (2) found that neither the substrate nor the anode had an effect on whether moss appeared. The overpotential was found to decrease or stay constant after moss became visible, and the equilibrium potential shifted cathodically about 5- 10 mV. In concentrated zincate electrolytes, the dominant complex is $Zn(OH)_4^{-2}$ (1) and this species would migrate toward the anode. Moss also forms when non-colloidal electrolytes are used(2). Therefore, it is unlikely that colloidal particles play a role in mossy zinc deposition.

Epelboin and co-workers (20, 21) postulated that surface diffusion of an adsorbed Zn^+ species leads to variations in the current distribution on the microscale, causing the formation of isolated packs of moss. The main observation supporting this theory is that lead impurities in the electrolyte inhibit moss formation. Small additions of lead do not affect the transport of zincate ions; however, the kinetics are drastically changed. Tsuda(22) noted that the addition of lead raises the activation overpotential for nucleation, so the growth and coalescence of existing protrusions are favored.

Neither the existence of a substantial compact layer that is deposited before moss is initiated nor the apparent absence of moss with increasing overpotential is explained by the surface diffusion theory. If surface diffusion was a factor, a substantially thick compact layer would not be formed. When the current density is raised, the secondary current distribution is rendered less uniform, and the current density in the highest regions does not change. Consequently, the random crystalline habit of moss should be preserved if surface diffusion was the cause of mossy zinc deposition.

To explain the drastic change in crystalline habit that occurs when moss is formed, Epelboin and co-workers postulated the existence of an unknown, stable species, Zn^+. This ion has an electronic configuration of $[Ar]4s^1$ and is very unstable because of the half filled s shell. Even when stabilizing anions are present, this species has *never* been detected; therefore, it is highly unlikely that its surface diffusion can play a controlling role in the deposition of zinc.

Popov and co-workers (23, 24, 25) proposed that spongy zinc formation was the result of the deposition process being under mass transport control while the nucleation density is low. They deposited zinc onto stationary, vertical copper cylindrical cathodes using both constant and pulsating overpotentials. When the overpotential was below 80 mV(23), the deposits were compact; otherwise, dendrites were formed, a result that is in general agreement with Arouete's findings(9). When the potential was low and held constant ($<$ 40 mV) spongy deposits were initiated after an induction time on the order of minutes. At cathodic overpotentials between 40 and 80 mV, sponge formed after a much longer induction time.

Popov and co-workers(24) hypothesized about the growth of moss using an activation-diffusion control argument. The relationship between the current density (i) and the overpotential (η) developed using this argument was:

$$i = i_0 \frac{[\exp \alpha_c \eta \frac{nF}{RT} - \exp -\alpha_a \eta \frac{nF}{RT}]}{1 + \frac{i_0}{i_l} \exp \alpha_c \eta \frac{nF}{RT}} \qquad (2\text{-}1)$$

They stated that the deposition process was activation controlled if the ratio of the exchange current density to the limiting current density, i_0/i_l, was much less than 1 and diffusion controlled if $i_0/i_l >> 1$.

At low densities of nuclei, the individual protrusions grow independently, and the diffusion limiting current to the growth center is inversely proportional to its radius(23).

Popov and co-workers assumed that the electrolysis process was under mixed control when i $>=$ 0.2 i_l, therefore the induction time for mossy zinc initiation is given by:

$$t_i = \frac{i_l}{{i_0}^2} nF \frac{\delta}{V_m[\exp\alpha_c\eta\frac{Fn}{RT} - \exp-\alpha_a\eta\frac{Fn}{RT}][4\exp\alpha_c\eta\frac{Fn}{RT} - 5\exp-\alpha_a\eta\frac{Fn}{RT}]} \quad (2\text{-}2)$$

This equation implies that as the magnitude of the overpotential increases, the induction time for moss formation decreases, and that as the diffusion layer thickness becomes smaller, moss formation is more likely.

Neither of these findings are supported by the author's own results. When the overpotential is between 40 to 80 mV, a mossy or dendritic deposit was formed after a much longer induction time than that represented by equation (2-2). When the overpotential was lower, the initiation time was not of the order of magnitude predicted by theory. Poor control of the experimental conditions is a possible cause of the discrepancy, since the experimental cathode was a stationary, vertical copper cylinder, a system subject to natural convection effects. The fact that the induction time increases, rather than decreases with overpotential, indicates that the theory is not satisfactory.

Popov and co-workers' conclusion that spongy deposit formation on an inert substrate is caused by mass transport limitations when the density of nuclei is low is also contradicted by results obtained in flowing media. According to Popov, the induction time is directly related to the thickness of the mass transport boundary layer, yet when electrolyte flow is used, a substantial compact layer is formed before the onset of moss(13). The conclusion that mass transport control is involved in mossy deposit initiation, is refuted by the result that moss is found in systems employing flow in which the current density is far below the limiting current.

Wiart and co-workers (26, 27, 28, 29, 30) proposed a theory that postulates that zinc deposition takes place through a conductive oxide sublayer, and the ion diffusion process is

mass transport controlled. The oxide layer was purported to be ZnO, which was formed as a result of the self discharge of the zinc deposit(30). The blocking effect of this semiconducting film results in the reduction of the interfacial area available for charge transfer and the formation of scattered packs of spongy deposits. Increasing the current density caused the oxide to break down, resulting in a larger surface area available for deposition. When anodically dissolved zinc ions are in the electrolyte the growth of spongy deposits is favored purportedly because the oxide sublayer through which deposition takes place is thinner(26).

To support those hypotheses, they presented the current transients from potentiostatic experiments that were performed in a potential range that ensured kinetic control of the electrodeposition process. They found that the current transients decayed to a single value, independent of both the time and of the rotation rate, that, according to them, was a result of the slow blocking of the electrode surface with time. However, if a protective film were formed, the time that it took to form this layer would be heavily dependent on the rotation rate, since a substantial supersaturation of the zincate species is necessary for zinc oxide to be nucleated. Furthermore, the solubility of zincate in potassium hydroxide increases with pH in the range studied (1), so the formation of an oxide layer is unlikely. It is more reasonable to conclude that the decay of the current to a single value is caused by the development of roughness on the surface and the initiation of moss.

Scratching the electrode surface with a macroscopic probe resulted in the induction of a new transient; however, this process induces defects on the surface, resulting in sites for the renewed nucleation of crystals. Thus, it is not unusual that there was a new transient recorded.

In Figure 2.2, a figure is reproduced from Wiart and co-workers(28). They used this data to determine that the charge transfer was controlled by ion diffusion through a porous layer and cited the work of Vorkapic(31) to support their arguments. However, Vorkapic clearly stated that the corrosion rate of zinc in KOH electrolytes *increased* with the support-

ing electrolyte concentration and furthermore, passivation of the zinc electrode occurred faster in quiescent media. Therefore, if an oxide layer is to cover the zinc surface, this layer would form faster as the current density is raised (since the local concentration of KOH would be greater), and the resistance should be high. When an experiment is conducted under potentiostatic conditions, the slope of the resistance vs. current density curve should decrease with time.

Wiart also stated that the formation of anodically dissolved species caused the initiation of mossy deposits, in an argument similar to that presented by Kudryavtsev (15-19). However, Oswin and Blurton (2) mentioned that the use of a dissimilar anode had no effect on the transition time to mossy zinc formation.

Lead was shown to inhibit the growth of mossy zinc. However, lead is known to influence the kinetics of zinc deposition by enhancing the rate of hydrogen bubble formation and inhibiting the nucleation of new nodules(22). Lead ions are not known to influence the self-discharge rate of the zinc electrode, so if the growth of an oxide layer was the cause of mossy zinc formation, lead ions should not have an effect on the transition from a compact to a mossy deposit.

Additional doubt on the proposed mechanism was presented by Hamnett and Mortimer (32), who performed cyclic voltammetry coupled with ellipsometry on zinc electrodes. While they found that zinc oxide formed upon oxidation of the zinc electrode, that layer was reduced at potentials less negative than zinc electrodeposition. When zinc was being deposited from neutral solutions, no oxide was detected. These results were confirmed using the Raman technique by Hugot-LeGoff (29).

2.5 Stability in Crystallization Processes

The amplification of surface roughness can have drastic effects on the concentration profile and current distribution on a growing surface. Stability analyses have served to clarify our understanding of the processes that affect the rate of growth of perturbations. Electrodeposition processes, at any economically practical conditions, are inherently unstable; however, conditions of meta- stability can be realized with the appropriate combinations of experimental conditions. Stability criteria can help to select the optimum conditions for deposition.

The first rigorous stability analysis was performed by Mullins and Sekerka (33, 34, 35), who studied phase transformations induced by heat or supersaturation. A perturbation analysis employing Laplace's equation to describe the concentration or temperature gradients was used to test the stability of both planar and flat surfaces. It was assumed that the surfaces were isotropic, that a steady state existed, and that there was local equilibria at the surface. Their stability criterion was simple: if the perturbation increased in magnitude, the surface was unstable. Increasing the gradients of either heat or mass resulted in an unstable surface. Conversely, surface tension could help to stabilize the surface- although in electrochemical processes, this effect is overwhelmed by convection(36). An aggregate of several spheres could remain stable because of the interactions between the spheres.

Aogaki and co-workers (37, 38) applied the principles advanced by Mullins and Sekerka to electrochemical processes with the goal of explaining why a crystal begins and why it continues to grow on a planar surface. Using the same perturbation methods, they found that under mass transport controlled conditions, electrodeposition processes are always unstable. However, they acknowledged that there were systems in which a stable, planar growth was attained. They stated that this could occur for two reasons: (1) the growth time constant is so small that any roughness develops very slowly, or (2) the growth time constant takes

positive values in a wavelength range that is so large that the actual system cannot allow the perturbation to grow. Forced or natural convection disturbances were found to have a stabilizing effect on the deposit characteristics.

Aogaki and co-workers (37, 38) used their analysis to explain the growth of silver powders. They looked at three cases: (1) -50 mV, that was said to be far below the limiting current plateau, (2) -200 mV, that was at the initial part of the limiting current plateau, and (3) -400 mV that was higher than the limiting current plateau. They calculated the time to achieve the maximum growth constant and found that it was 244 s, 10 s, and 0.22 s for the three overpotentials specified. When the induction time is very large, as in the first case, the perturbation will grow very slowly, because it is cancelled out by other disturbances; thus, no powder will appear. The analysis predicts that there will be an induction time before silver powders are initiated, a result that is in agreement with experimental observations. The powder formation rate was enhanced by increasing the cathodic polarization, the concentration or the flow rate. However, the analysis was valid only for mass transport controlled situations, and increasing the latter two parameters results in the onset of kinetic control. The tendency to form powders lessened with rising temperature. Under galvanostatic conditions, powder formation was enhanced by increasing the current density, decreasing the bulk concentration or decreasing the temperature.

Landau and Shyu(36) extended the Mullins and Sekerka analysis to include both concentration and kinetic overpotentials. They found that, under practical conditions, electrodeposition processes are unstable. However, there is a region in which the induction time for significant roughness initiation is very large, so some electrodeposition processes can be performed at conditions of pseudo-stability. The induction time for roughness initiation is a very strong function of the exchange current density, and it was found that as this parameter increased, roughness developed both faster and at lower overpotentials. The critical overpotential was found to be only a weak function of the surface energy. The interfacial concentra-

tion was also shown to have an effect on the development of roughness; as it increased, roughness was less likely to occur, although if the concentration at the metal/solution interface was raised by augmenting the bulk concentration, then the effect is much smaller.

Barkey and Tobias (39, 40, 41) extended the Landau analysis to include ohmic effects. Laplace's equation was solved for both the concentration and the potential for a sinusoidal perturbation of the surface. The governing equations are shown in Figure 2.3, taken from the PhD thesis of Barkey(39). It was assumed that both the diffusion boundary layer thickness, δ, and the wavelength of roughness, $2\pi/\omega$, were much larger than the roughness amplitude, A. Surface motion was neglected, an assumption that introduced a small error in the results. Using a steady state analysis, it was found that the concentration and potential fields could be described by:

$$C=C^0+C^pA[e^{-\sqrt{2\omega}z}-e^{\sqrt{2\omega}z-\sqrt{2\omega}\delta}]\sin(\omega_x x)\sin(\omega_y y) \tag{2-3}$$

$$\phi=\phi^0+\phi^pA[e^{-\sqrt{2\omega}z}]\sin(\omega_x x)\sin(\omega_y y) \tag{2-4}$$

C^0 and ϕ^0 are the solutions to Laplace's equation for a flat surface

$$C^0=C_b[1-\frac{i_a}{i_l}(1-\frac{z}{\delta})] \tag{2-5}$$

$$\phi^0=\frac{RT}{\alpha nF}\ln(\frac{i_a}{i_o})+\frac{RT}{nF}\ln(1-\frac{i_a}{i_l})+i_a\frac{z}{\kappa} \tag{2-6}$$

and C^p and ϕ^p are constants described by:

$$C^p=\frac{\kappa}{nFD}\frac{1}{(1+e^{-2\sqrt{2\omega}\delta})}\phi^p \tag{2-7}$$

$$\phi^{p}=-\frac{\frac{i_a}{\kappa}+RT\frac{i_a}{n^2F^2DC_b(1-\frac{i_a}{i_l})}-2\nu\gamma\frac{\omega^2}{nF}}{1+RT\frac{\sqrt{2}}{nF(i_l-i_a)}\kappa\omega+RT\frac{\sqrt{2}}{i_a nF\alpha}\kappa\omega} \qquad (2\text{-}8)$$

Barkey and Tobias confirmed that the transition to unstable growth occurs at very small spatial periods. The model predicted that the spatial period of roughness will decrease with increasing current density and with a smaller fraction of the limiting current. The ohmic effects reduced the margin of stability during electrodeposition.

2.6 The Effect of $[OH]^-$ *on the Electrodeposition of Zinc*

While stability analyses can give us an idea of what parameters will affect growth of protrusions, they cannot cause a change in crystal structure. Although the instability of the surface may *provide* the conditions under which the morphology will change, it cannot alone *cause* a change in crystalline habit. However, the development of surface roughness can lead to perturbations in the concentration and potential fields that will affect the kinetics of the zinc reaction, thus causing a change in crystal habit.

Farr and Hampson(42) determined the value of the steady state overpotential for a range of current densities. From their Tafel plot, they determined the value of the transfer coefficient, α, and of the exchange current density i_o. The exchange current density was independent of the zinc ion concentration for the range studied; however it was directly related to the hydroxide concentration. These researchers hypothesized that the dependence of the exchange current density on the pH indicated a "considerable interaction between that ion and the electrode surface". By assuming a mechanism for the zinc reaction and calculating the theoretical exchange current density, they were able to conclude that hydroxide is adsorbed onto the surface and that a two step charge transfer process was likely. The adsorption of the OH^- ion was confirmed by impedance measurements (43).

Similar results were obtained by Bockris, Nagy and Damjanovic (44); however, they also found that the exchange current density was a strong function of the zinc concentration. Their explanation for the purported independence stated that the conductivity of the electrolyte did not change. However, Farr and Hampson used much higher concentrations of zinc than Bockris and co-workers, and in that range, the zincate complex concentration varied little with total zincate concentration. Therefore, it is reasonable to assert that although the total zincate concentration varied, the concentration of the active species remained approximately the same (shown in Figure 2.4) and so there would only a negligible effect of total zinc concentration on the exchange current density.

Dirkse (45) measured the EMF of the zinc electrode in alkaline media of varying strengths. As shown in Figure 2.5, for a solution having the same ionic strength, it was found that the zinc electrode potential shifted cathodically as much as 30 mV (from -1.36 V vs. Hg/HgO to -1.39 V vs. Hg/HgO) as the KOH concentration increased from 2.8 M to 6.69 M. The zinc electrode exhibited non-nernstian behavior; this was attributed to the low concentration of supporting electrolyte. Only the tetrahedral zincate ion governed the potential of the zinc electrode, an expected result, since this ion is the dominant complex in the electrolyte (shown in Fig 2.4).

These results were confirmed by Isaacson, Mc Larnon, and Cairns(46, 47), who also calculated the activity coefficients from the potential data. The KOH–$K_2Zn(OH)_4$–H_2O electrolytes were found to be highly non-ideal except at a low concentrations of KOH. The activity coefficient decreases with increasing $K_2Zn(OH)_4$ concentration. In a later publication (47), they measured local potential changes during charging and discharging cycles and calculated the interfacial concentrations of the reacting species. Although the OH^- molality is nearly constant (but slightly above the bulk concentration) during the initial part of charge, it increases drastically during the last stages of the charging cycle. During the discharge cycle, the hydroxide concentration varies from 5.8 to 5.4 M.

Achmetow and Wosdwishenskij (6) examined the equilibrium potential of zinc single crystal electrodes in several electrolytes. They found that in sulfate media, the basal plane had a more positive potential than the sides of the unit cell, the $\{10\bar{1}0\}$ planes. They attributed this experimental observation to the bonding of the zinc atoms to each other- that is, it is stronger on the basal plane, and the bound atoms have less ability to pass into solution. In contrast, in 25% KOH, the basal plane, {0001}, had a lower potential than the side faces; a result that the researchers stated was unexpected. They attributed this observation to the complexing of zinc with hydroxide ions, saying that it was easier for the bound basal plane atoms to enter the solution.

2.7 Summary

Although many mechanisms have been proposed to explain the onset of mossy zinc formation at low current densities, none of the current theories account for the experimental results. Several observations appear to be well established:

(1) After a substantial compact layer is formed, nodules of moss are initiated

(2) At low fractions of the limiting current, spongy or mossy deposits form only when depositing zinc or cadmium, both chemically similar, group IIb metals.

(3) Raising the current density inhibits moss formation.

(4) The exchange current density is directly related to the free hydroxide concentration.

An important factor appears to be the crystal properties of the group IIb metals, specifically anisotropies between the growth rates and the potential of the crystal planes. Also, the stability of the growing metal electrodeposit surface may contribute to perturbations in the current distribution that, in turn, may cause the formation of a faster- growing crystalline plane.

Figure Captions

2.1 Differences between: (a) crystallization from a vapor; (b) electrocrystallization from solution, after (7).

2.2 Variations of the resistance, R_t, and capacitance, C^*, with current density during the layer formation. Time in minutes is indicated inside circles and arrows correspond to the electrode ageing. Electrolyte: 1 M ZnO with 8 M KOH, $\eta = 1$mV, after (28).

2.3 Equations and boundary conditions for current distribution on a sinusoidal profile, after (40).

2.4 Distribution of zinc complexes in alkaline media as calculated from equilibrium constants.

2.5 Variation of EMF with hydroxide concentration at room temperature, after (45): (a) 2.8 M; (b) 4.08 M; (c) 6.69 M. The zincate concentration was 0.01 M and the total ionic strength was 6.1 M.

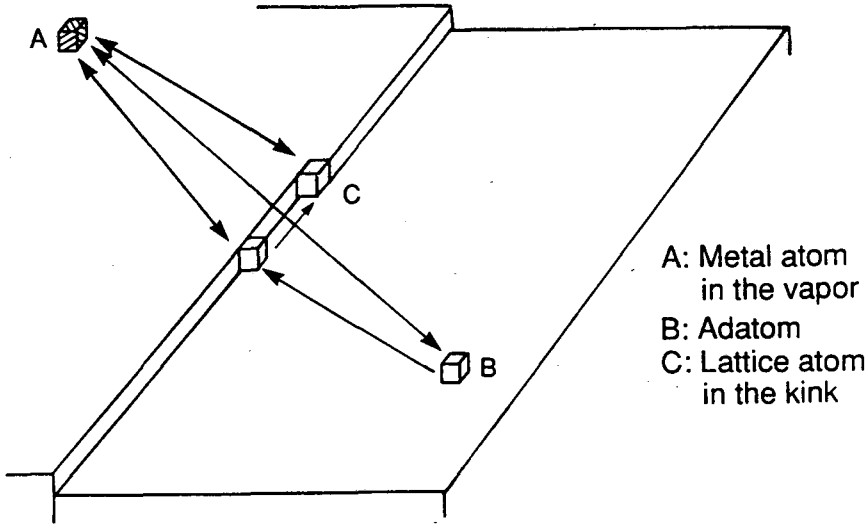

(a)

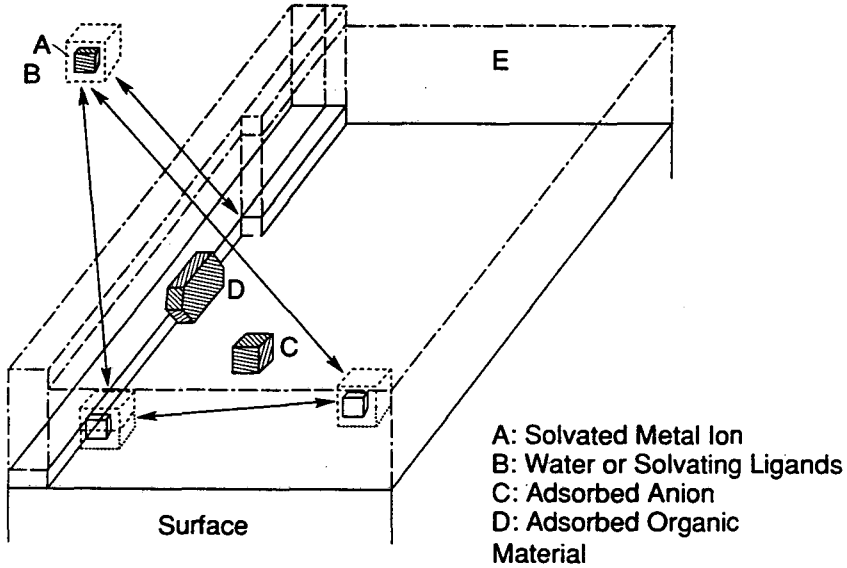

(b)

XBL 906-6421 A

Figure 2.1

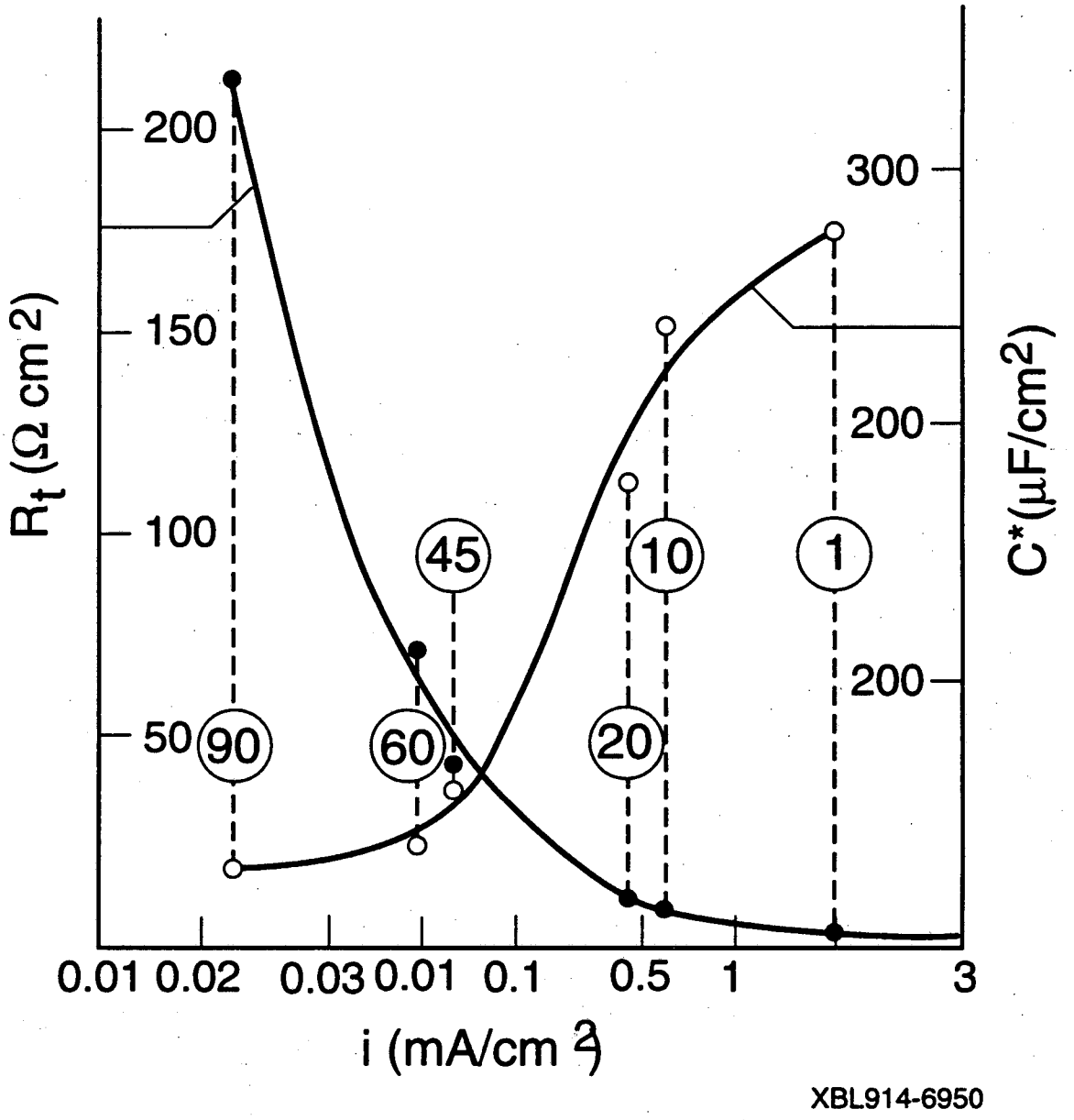
200
150
100
50
R_t (Ω cm^2)
300
200
200
C*(μF/cm^2)
90
60
45
20
10
1
0.01 0.02 0.03 0.01 0.1 0.5 1 3
i (mA/cm^2)
XBL914-6950

Figure 2.2

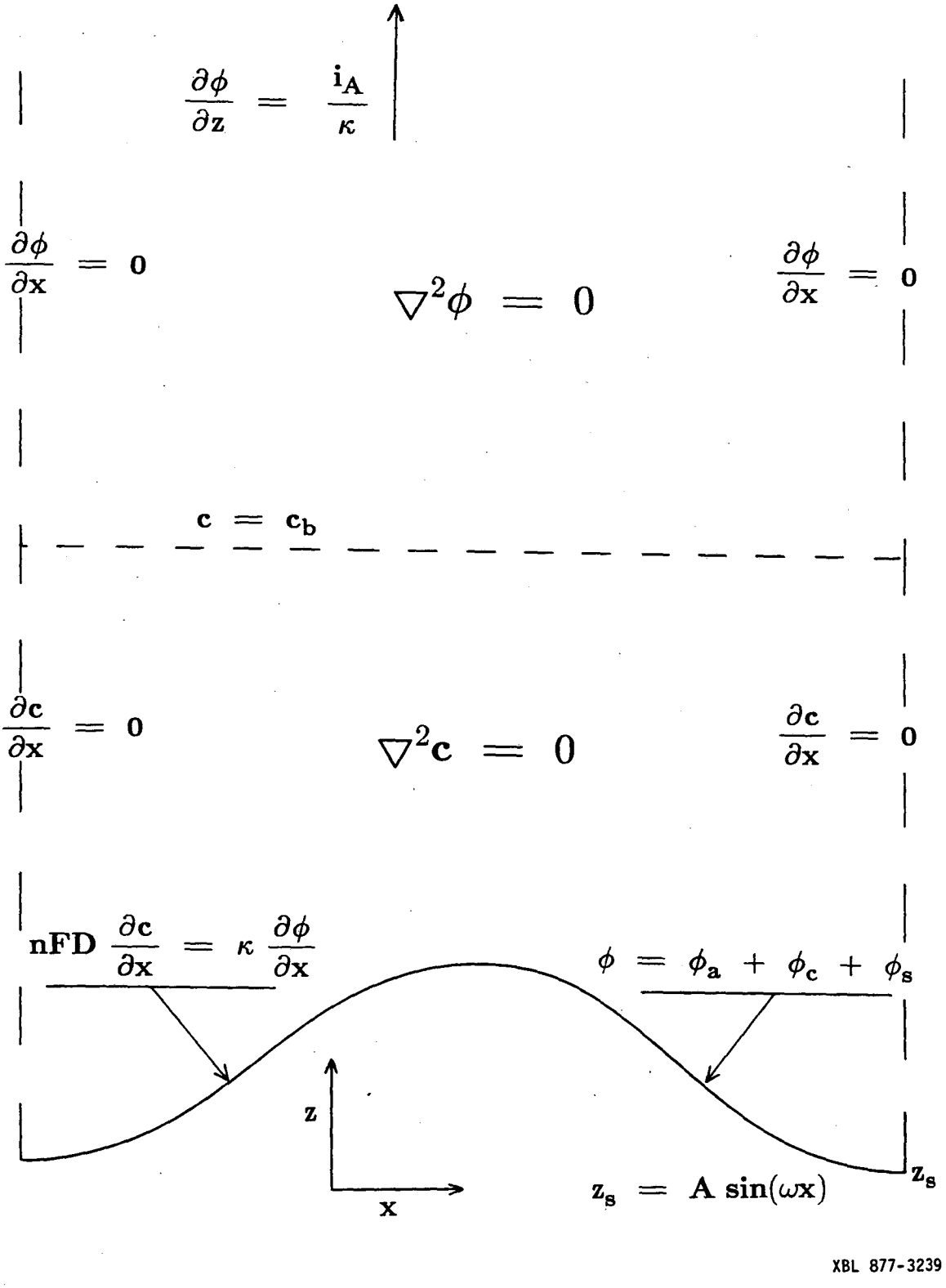
$\frac{\partial \phi}{\partial z} = \frac{i_A}{\kappa}$
$\frac{\partial \phi}{\partial x} = 0$
$\nabla^2 \phi = 0$
$\frac{\partial \phi}{\partial x} = 0$
$c = c_b$
$\frac{\partial c}{\partial x} = 0$
$\nabla^2 c = 0$
$\frac{\partial c}{\partial x} = 0$
nFD $\frac{\partial c}{\partial x} = \kappa \frac{\partial \phi}{\partial x}$
$\phi = \phi_a + \phi_c + \phi_s$
z
x
$z_s = A \sin(\omega x)$
z_s
XBL 877-3239

Figure 2.3

Zinc Complex Distribution for a total ZnO concentration of 0.5 M

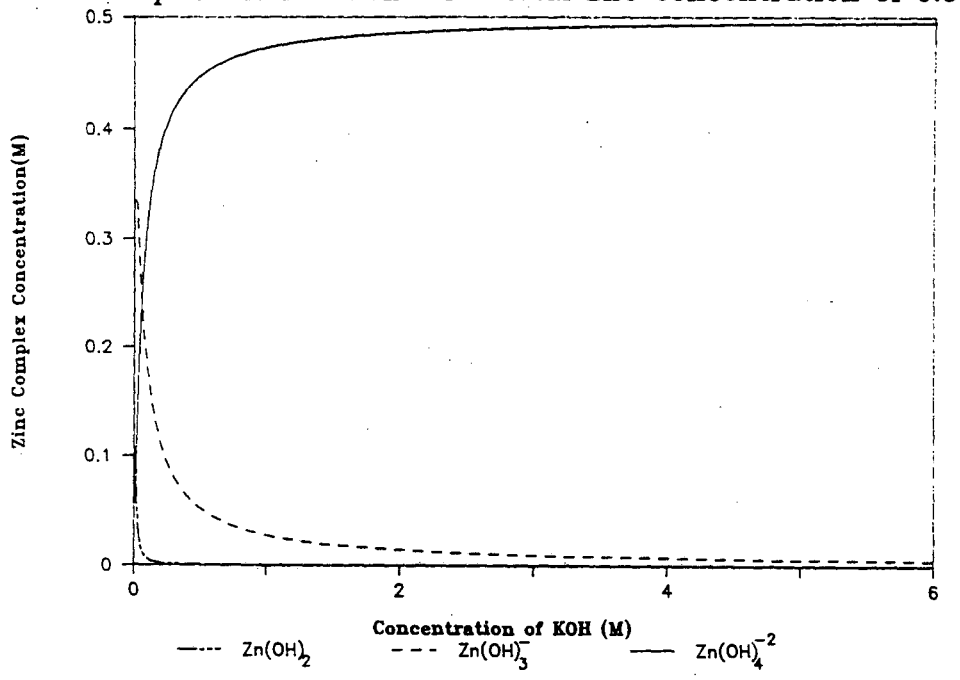

Distribution of Zinc Complexes for a total KOH concentration of 6 M

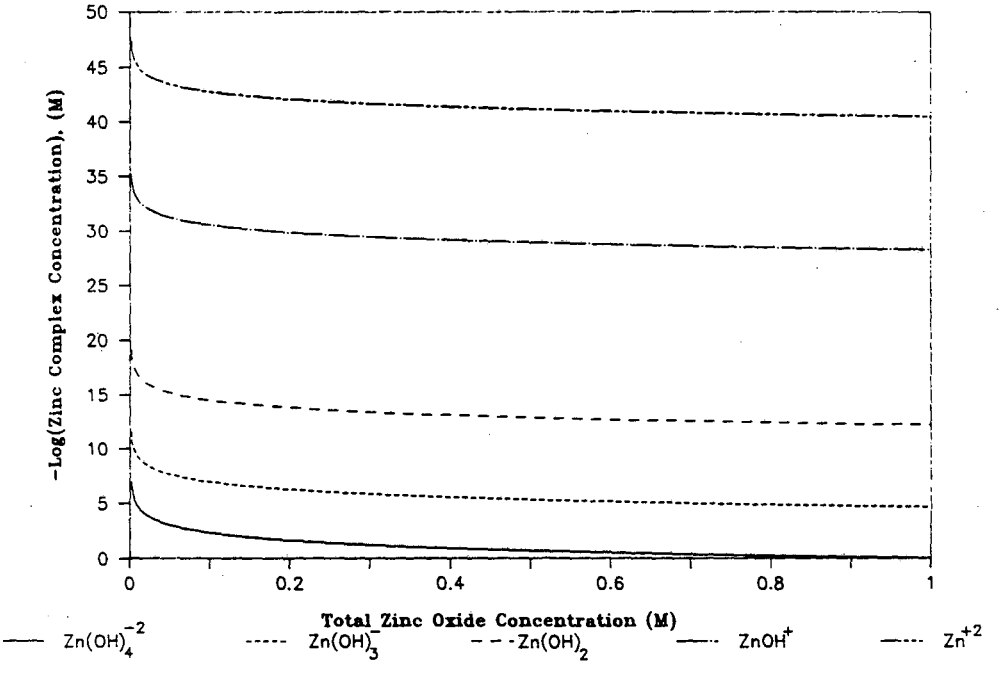

XBL 8811-3831 A

Figure 2.4

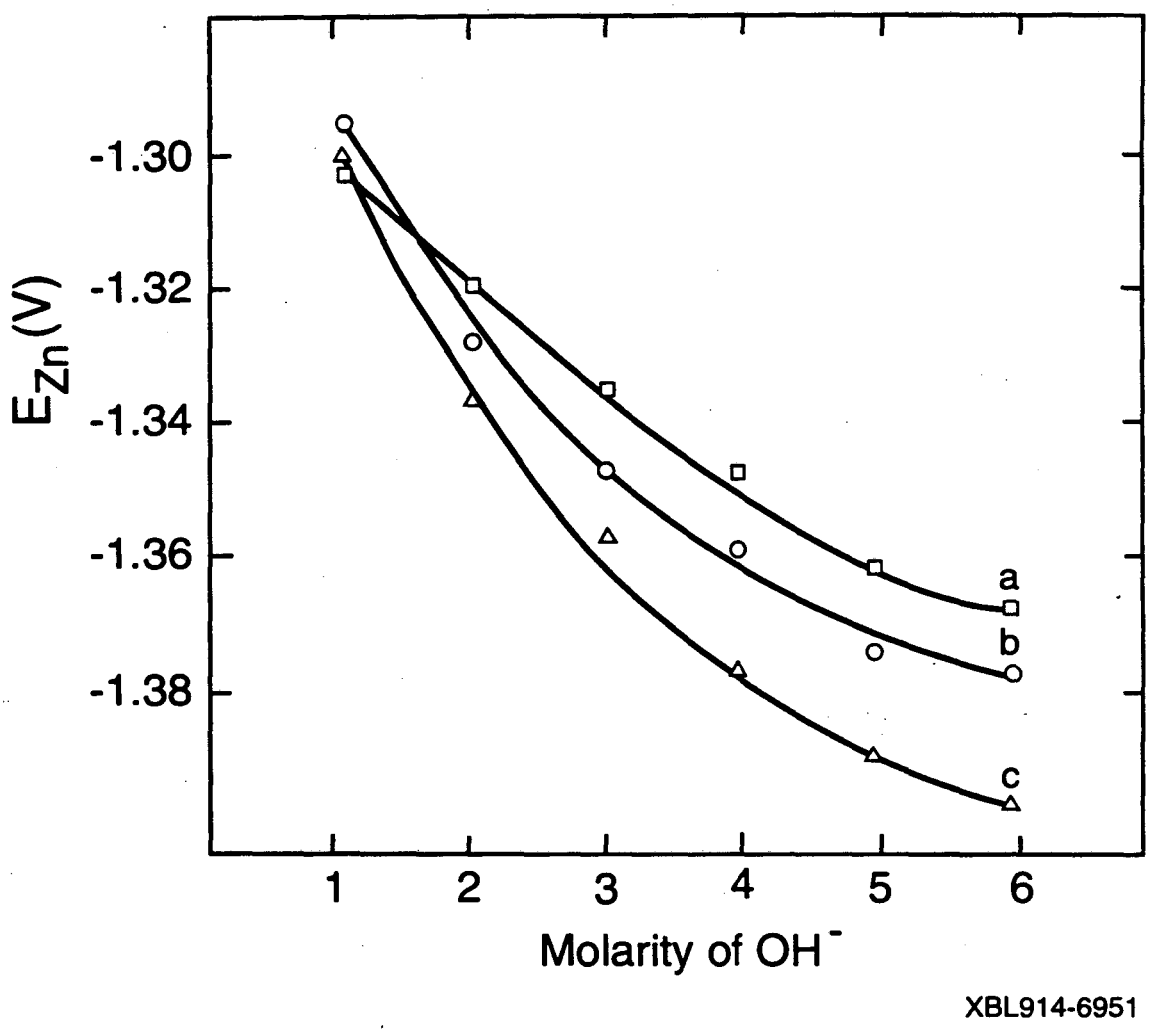
-1.30
-1.32
-1.34
-1.36
-1.38
E_{Zn}(V)
1
2
3
4
5
6
Molarity of OH^-
a
b
c
XBL914-6951

Figure 2.5

EXPERIMENTAL

3.1 Experimental Apparatus

A rotating cylinder cell and a channel flow cell were employed in this investigation. The rotating concentric cylinder cell, pictured in Figure 3.1, was used for most of the experiments. Both the primary and secondary current distributions are uniform in this system, and the ohmic drop can be accurately calculated(48). In addition, the mass transport characteristics of the rotating cylinder system are well known; the interfacial concentration is uniform and can be calculated. The channel flow cell, shown in Figure 3.2, was used for in-situ observations of developing deposits.

The rotating cylinder cell, represented in Figure 3.3, consists of two compartments: one for the working and counter electrode, the other for the reference electrode. The two sections are connected by a capillary filled with a thread of acrylic yarn that facilitates wetting in the capillary, thus ensuring electrical contact between the reference and working electrodes. The cell was made of Teflon, while the capillary was machined from Kel- F (a fluorinated polymer). As shown in Figure 3.3, the anode is placed around the inner surface of the working electrode compartment, while the cathode is mounted on an rotator (that had a brush connection) and lowered into the solution to achieve electrical contact. Electrical connection to the anode is provided by a gold plated steel bolt that is placed through a hole drilled in the Teflon wall of the working electrode compartment.

The channel flow cell has many useful features, which were required for the study of morphological development under controlled conditions. To assure fully developed flow at the electrode, a long entrance length is provided(50 cm). Contamination was prevented by using polypropylene, transparent polymethyl methacrylate, ethylene-propylene co-polymer, glass, and Teflon in the cell housing and piping system. All bolts holding the cell together were

gold plated, thus, potential sources of metallic impurities were eliminated. A five gallon overhead supply tank is used (shown in Figure 3.4), to minimize concentration changes. To enable the viewing of the deposition process while it is in progress, the cell body is bolted to a clear polymethyl- methacrylate cover. The cathode is mounted parallel to the cell cover, as shown in Figure 3.5. The anodes are placed in the bottom and top walls of the flow cell. A capillary connecting to an Hg/HgO reference electrode is placed halfway between the anode and cathode compartments in the insulating wall of the flow cell so that potentials could be measured; this is shown in the schematic of Figure 3.6. The channel cross section was 1.0 x 0.3 cm, thus allowing the use of high magnification, long working distance microscope objectives. A section of the cover plate was machined away to facilitate lighting of the surface; this is also pictured in Figure 3.5.

3.2 Electrodes

The cathodes of the rotating cylinder cell, depicted in Figure 3.7, were machined from 99.999% copper, zinc, or stainless steel rods 7 mm in diameter. To build this electrode, a 1.5 cm long piece was cut from a larger rod, and a hole was drilled on the circular face. A 4- 40 tap was made in the hole; using this threaded hole, the cylinder was connected to the rotator, and electrical connections were made to the rest of the circuit. When the cell was operating, the cathode's active area was bounded by a Teflon sleeve, that prevented wobbling of the electrode and provided a 1.5 cm^2 active surface. This Teflon cup was machined to fit in a cup at the bottom of the rotating cylinder cell.

The rotating cylinder cell anode is also shown in Figure 3.7. This 99.99% zinc electrode was machined to very precise tolerances. On one side of the ringed electrode, a small hole was drilled to accommodate the capillary for the reference electrode. On the other side of this electrode, a threaded hole was made through which the electrical connection was made.

The total active area of this anode is 19.6 cm^2.

The channel flow cell cathodes, represented in Figure 3.8, are composed of three pieces. The first two segments are buffer electrodes, which serve to diminish edge effects on the morphology. These pieces were cut from 1 mm thick copper foil. The micromorphology was studied on the central, main segment, which was encased in epoxy resin. This segment was constructed by attaching a 1.0 x 0.5 cm copper bar to a brass core using silver epoxy. The spaces between the electrode were then encased in non-conducting epoxy resin, and sanded to provide a flat surface.

The 99.99% zinc anodes of the channel flow cell are shown in Figure 3.8. These electrodes were cut from zinc foil in 2 layers and placed in the cell. The electrical connections were made using a silver wire, which was connected to the zinc sheet with silver epoxy. The back and sides of the anode were coated with non-conducting epoxy to insulate them from the electrolyte.

A Hg/HgO reference electrode is used to measure potentials in both cells and is shown in Figure 3.9. This electrode was constructed in- house, using platinum wire, mercury, mercuric oxide, and glass wool. The entire assembly is encased in a glass tube, which is then immersed in a container of 6 M KOH. The cell connection is made using a capillary tube, which was kept wet using an acrylic yarn.

3.3 Electrolytes

All solutions used in this study were prepared from analytical grade zinc oxide (Alfa products, 99.9% ZnO) and potassium hydroxide (J. T. Baker, 87.2% KOH). Water distilled in -house was used as the solvent. Before use, the electrolytes were purified using a zinc cementation process, which is described in more detail in the next chapter. The electrolytes were stored in polypropylene containers as a 1M ZnO, 12 M KOH stock solution, and were

diluted to the required concentration just before the start of the experiment.

3.4 Equipment

Overall views of the channel flow and the rotating concentric cylinder cells are shown in Figures 3.10 and 3.1. These systems include the cell, the flow loop, the electrical system, and the optics (channel flow cell). The optical system includes the following components:

(1) Microscope constructed in- house, consisting of a Bausch and Lomb microscope tube (160 mm) and an American Optical stage. This microscope was mounted with the tube in a horizontal orientation and a mirror was mounted inside the tube to direct the light rays to the appropriate eyepiece.

(2) Traveling control fabricated in- house. This controller has a maximum travel length of 3 cm and can achieve a speed of 6 cm/min.

(3) Leitz 50X ultra long focusing objective lens (N. A.=0.5, working distance 5.5 mm).

(4) Bausch and Lomb 7.5X hyperplane eyepiece.

(5) Sony MV-11 microscope adapter.

(6) Javelin metal oxide sensor camera (model no. JE2062).

(7) Sony VO-5800H 3/4" U-matic video recorder.

(8) Javelin VM-15 video monitor.

(9) American Optical fiber-optic light source, model number 1177 (150 W).

The following equipment was used for galvanostatic control in all experiments.

(1) Princeton Applied Research Model 371 potentiostat/ galvanostat.

(2) Princeton Applied Research Model 178 electrometer probe.

(3) Princeton Applied Research Model 276 interface.

(4) IBM computer, P/S 2- Model 50.

(5) IBM Plotter, Model 6180.

(6) National Instruments MC-GPIB IEEE-488 interface to connect PC to the potentiostat.

To achieve steady state mass transport conditions, flow was employed in all experiments. The equipment used to generate and measure flow is as follows:

(1) Gilmont Instruments shielded rotameter, which has a maximum flow rate of 9600 ml/min.

(2) Little Giant centrifugal magnetic drive pump (1/12 hp, model number 4-MD).

(3) Pine ASR2 analytical rotator and speed controller.

The electrode surface was characterized after deposition using profilometry, scanning electron microscopy, x-ray diffraction, and transmission electron microscopy. The following equipment was employed to analyze the electrode surface.

(1) ISI scanning electron microscope, model DS-130.

(2) ISI scanning electron microscope, model WB-6.

(3) Phillips transmission electron microscope, model 301.

(4) Clevite surfanalyzer, model number 15-632-7-20.

(5) DEC PDP 11/70 computer.

(6) Siemens Diffraktometer

Figure Captions

3.1 View of the rotating cylinder setup including the electrolyte compartment, the Hg/HgO reference electrode, the cathode, and the Pine rotator.

3.2 View of the Channel flow cell including the microscope, the videocamera, and part of the flow cell.

3.3 Schematic of the rotating cylinder cell.

3.4 Schematic of the flow loop for the flow cell, after (49).

3.5 Closeup of the electrode compartment of the channel flow cell showing the cover plate with the rectangular cutouts for illumination, the round cutout for the optical glass window, and the electrode compartment.

3.6 Cross section of the flow cell

3.7 Electrodes of the rotating cylinder cell including (from left to right) the zinc anode, a zinc cathode, and a copper cathode mounted in the Teflon sleeve.

3.8 Closeup of the electrodes in the channel flow cell including the rectangular cathode surrounded by 2 L-shaped buffer cathodes, and the anodes mounted in the cell walls.

3.9 Schematic of the mercury/ mercuric oxide reference electrode

3.10 Equipment for video studies of micromorphology of zinc deposits From left to right: Video screen showing image of developing deposit, (the width of the video screen corresponds to 0.8 mm on the electrode surface); video recorder; electrical instrumentation (potentiostat, ammeter); microscope with dual eyepiece; flow channel for deposition of zinc, from(50).

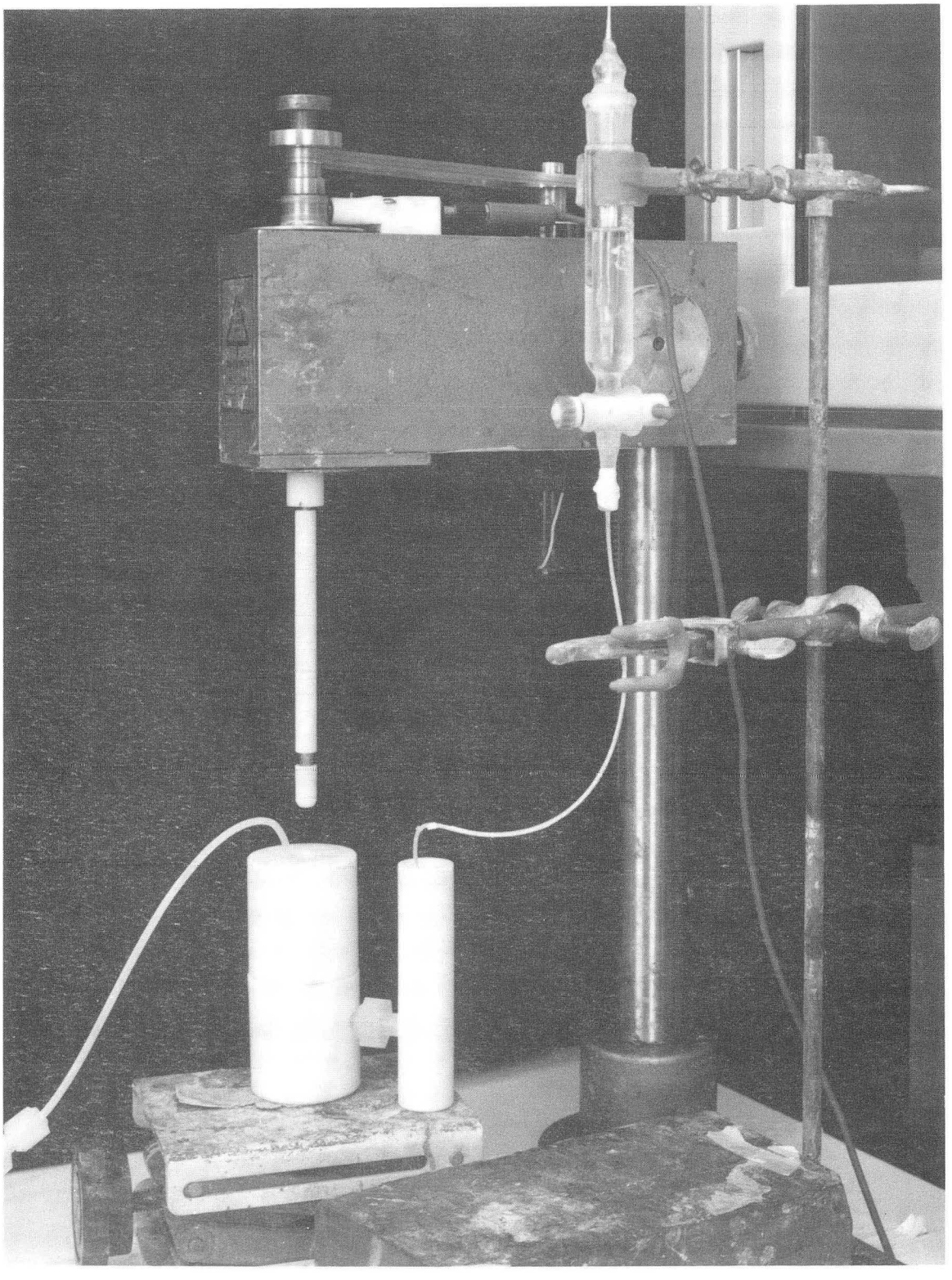

XBB 906-4634

Figure 3.1

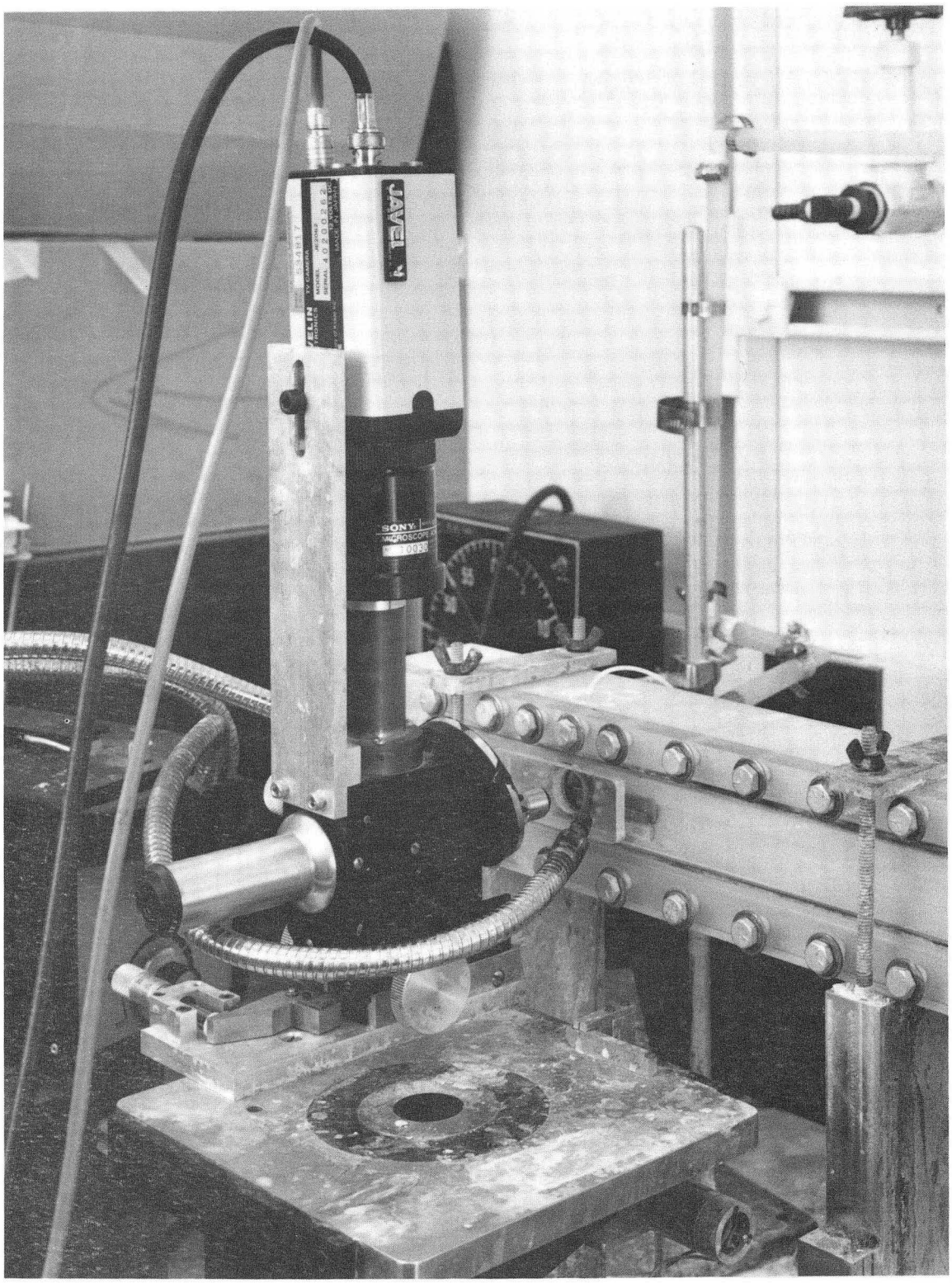

XBB 906-4633

Figure 3.2

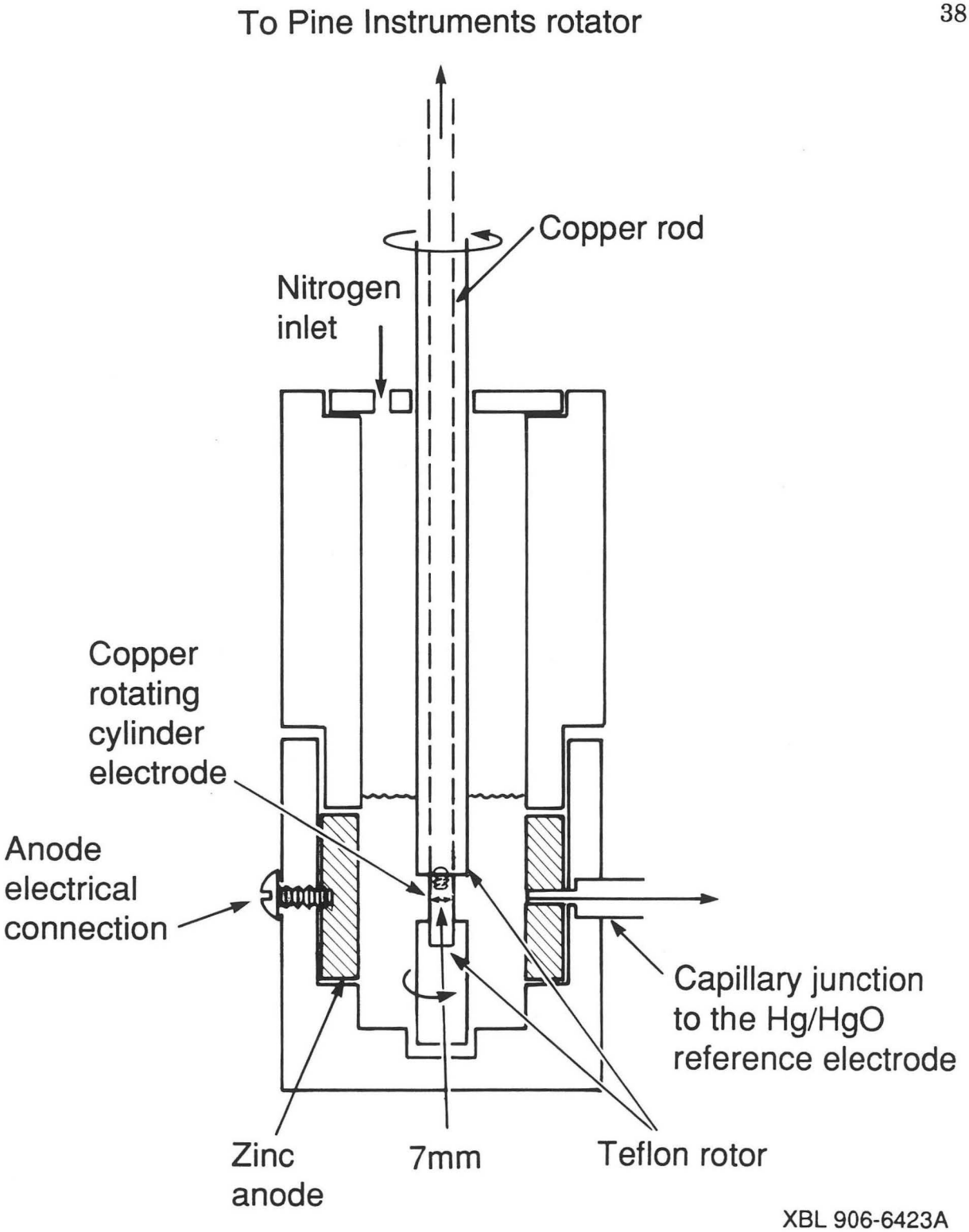
To Pine Instruments rotator
Copper rod
Nitrogen inlet
Copper rotating cylinder electrode
Anode electrical connection
Capillary junction to the Hg/HgO reference electrode
Zinc anode
7mm
Teflon rotor
XBL 906-6423A

Figure 3.3

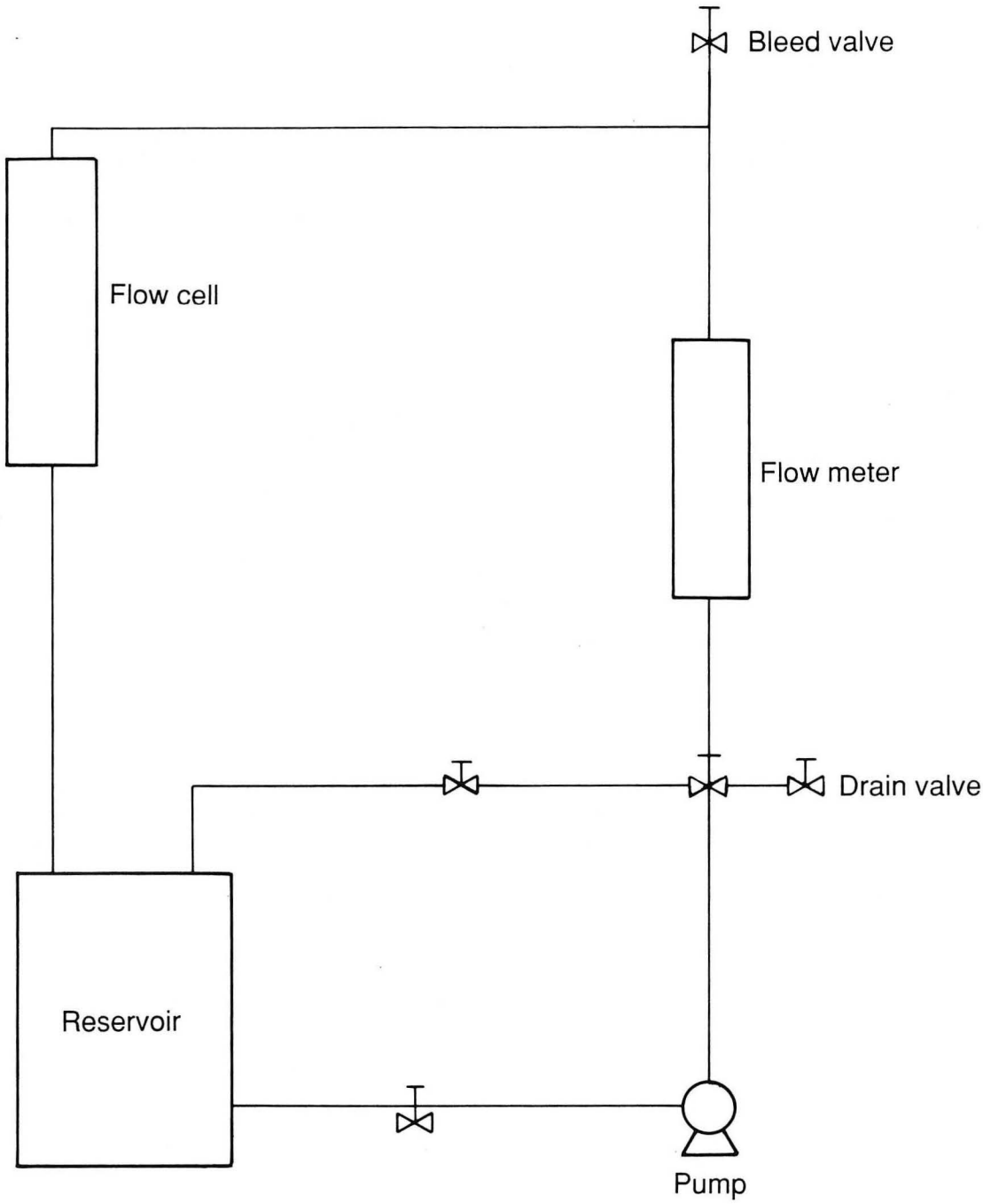
Bleed valve
Flow cell
Flow meter
Drain valve
Reservoir
Pump
XBL 907 – 6469

Figure 3.4

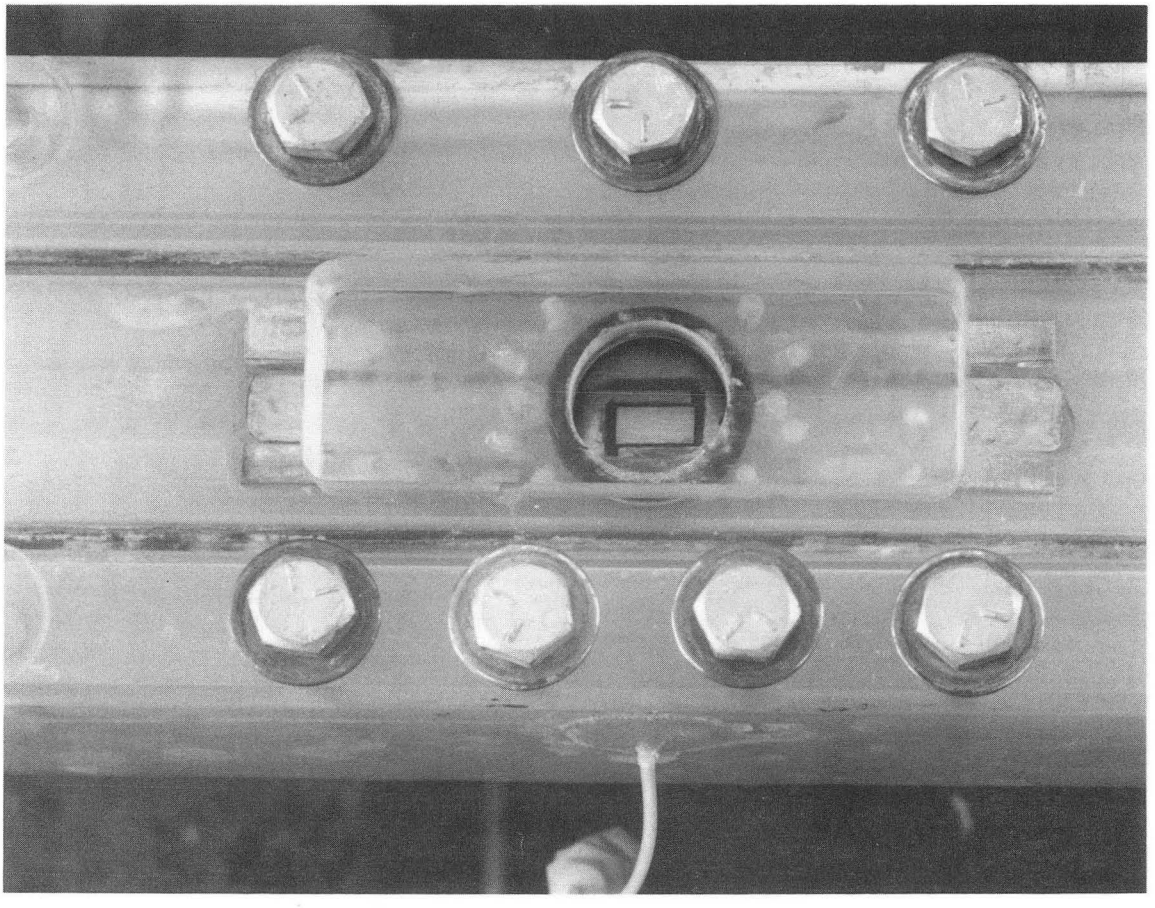

XBB 906-4630

Figure 3.5

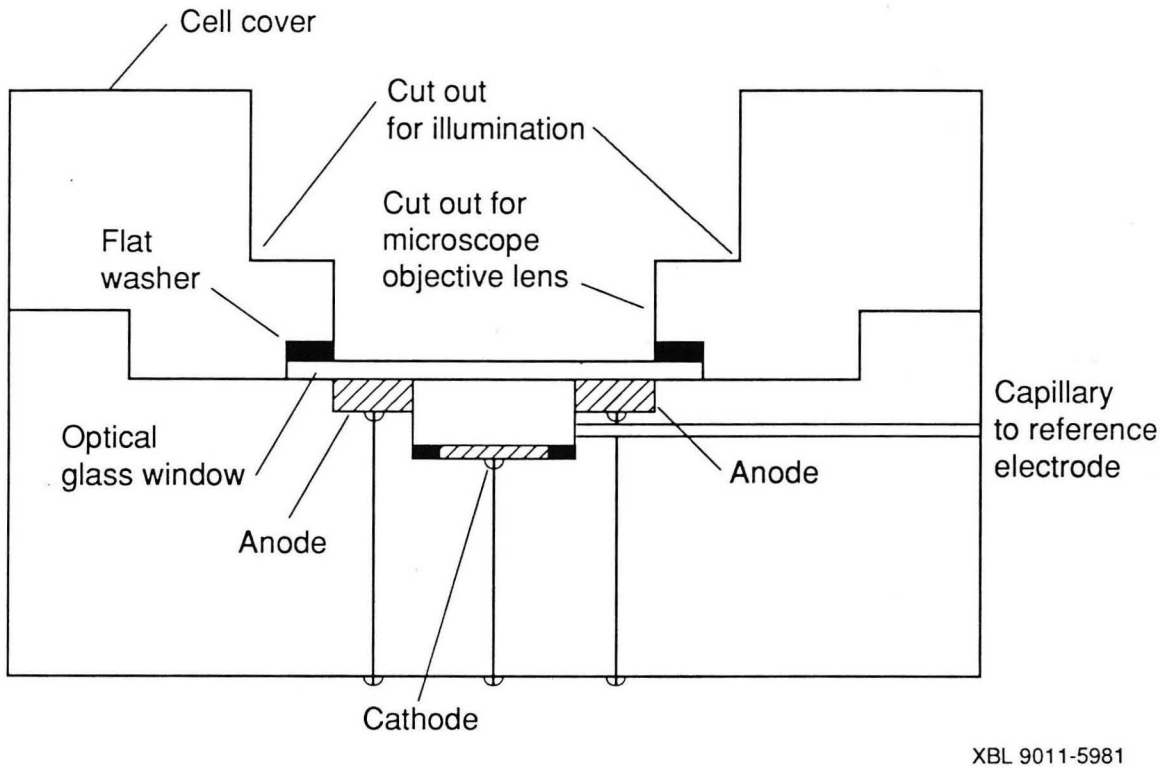
Cell cover
Cut out
for illumination
Cut out for
microscope
objective lens
Flat
washer
Capillary
to reference
electrode
Optical
glass window
Anode
Anode
Cathode
XBL 9011-5981

Figure 3.6

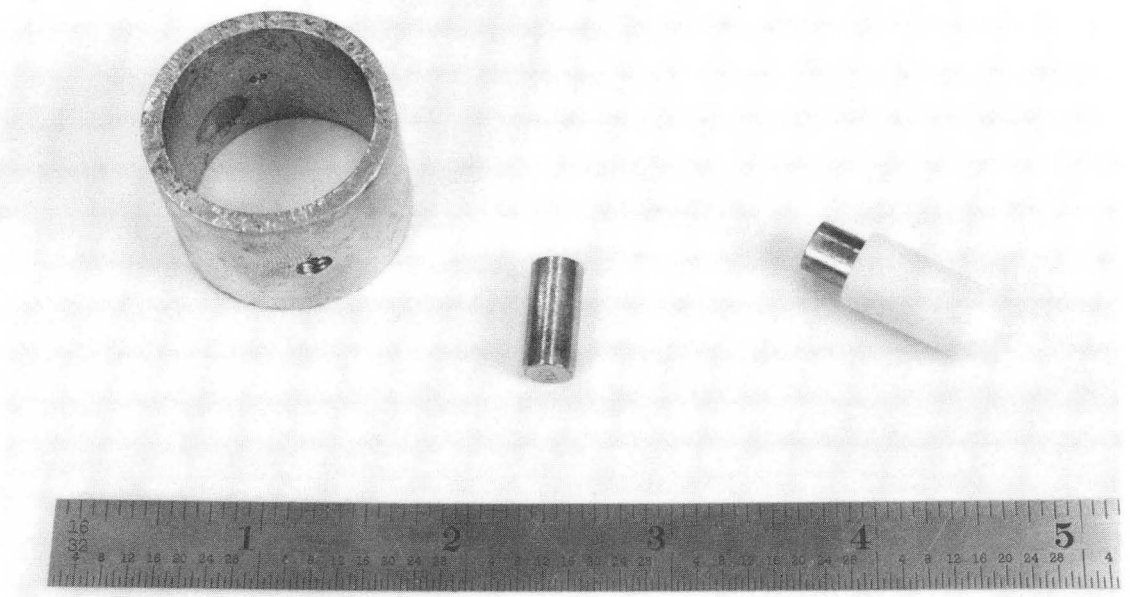

XBB 906-4629

Figure 3.7

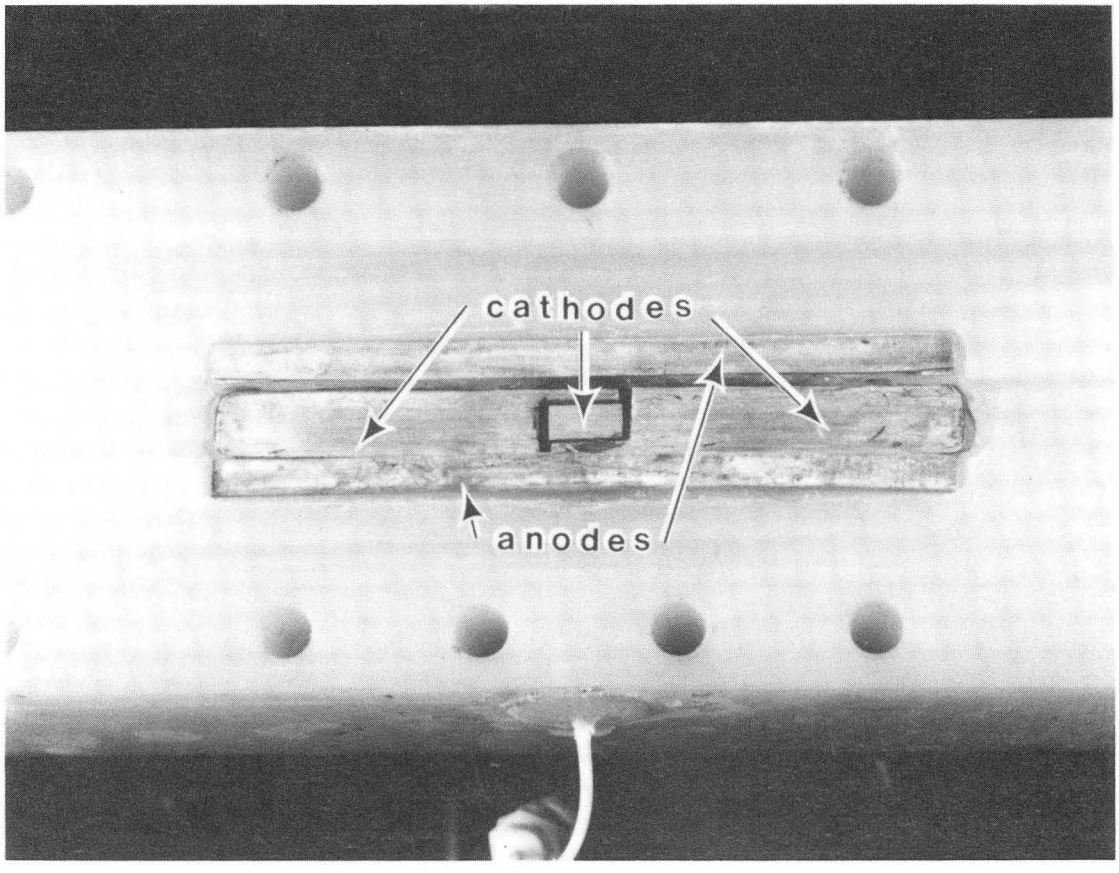

XBB 906-4631A

Figure 3.8

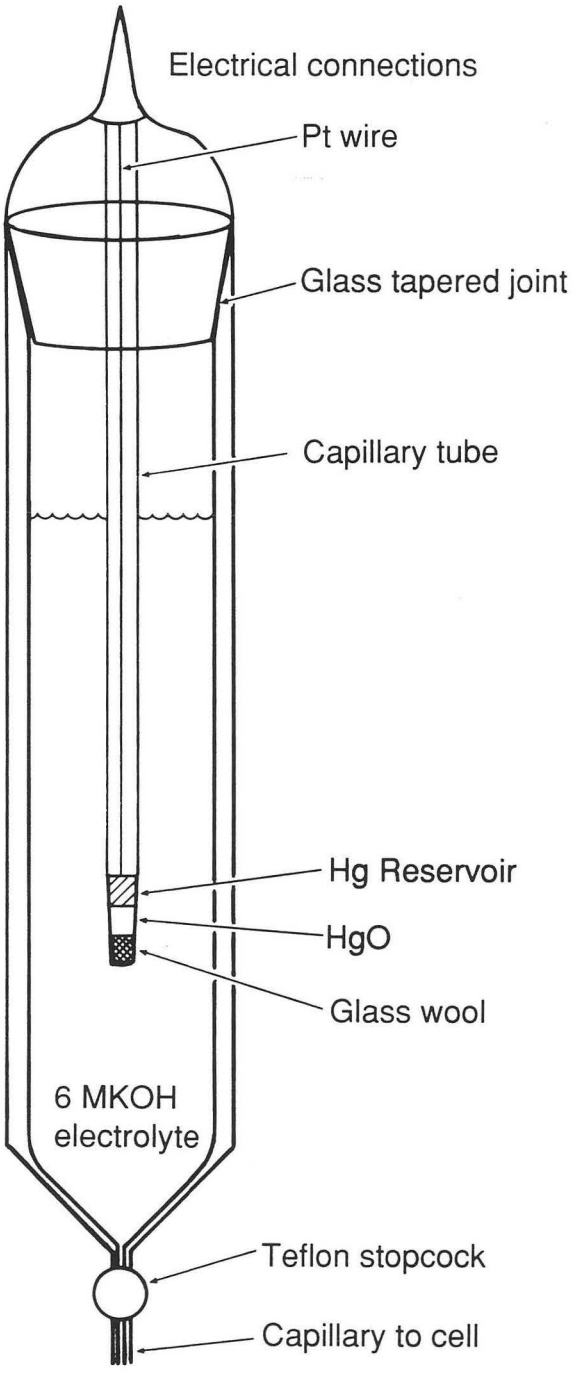

XBL 907 – 6468

Figure 3.9

BBC 856-4653

Figure 3.10

EXPERIMENTAL PROCEDURES

4.1 Electrode Preparation

The channel flow cell cathodes were sanded and polished after having been mounted in the cell, but before the electrical connections to the circuit were made. Successively finer grades of silicon carbide sandpaper (180, 240, 400, 600 grit) were employed in the sanding. Following each sanding step, the electrode was cleaned with water to remove large particles. After the sanding, the electrode was polished to a mirror like finish using a fine wire brush attached to a Dremel tool (Model 380). Subsequently, the electrodes were washed successively with ethanol, acetone, water, and methanol, after which the electrodes were dried using compressed air.

Before the rotating cylinder cathode was mounted, chemical and electrochemical polishing were performed. The electrodes were first soaked in a solution of 20% chromic acid, with 1.5% sodium sulfate added, and then washed in 20 % chromic acid (51). After the surface oxides were removed by chemical polishing, the electrodes were cleaned with water and placed into the electropolishing solution for 20 minutes. The electrochemical polishing was done in a solution of 85% phosphoric acid, with a cathode of copper foil, and an applied potential of 2.0 V (corresponded to about 50–100mA/cm^2)(51). The electrodes were then profiled and stored in a dust free environment until use. This preparation was designed to remove the portion of the surface that was damaged by mechanical working, leaving a stress free, reproducible metal surface.

4.2 Electrolyte Preparation

A stock solution of 1 M ZnO and 12M KOH was prepared by dissolving analytical grade zinc oxide in potassium hydroxide. This electrolyte was then purified using a zinc cementation technique, to remove metallic impurities. This procedure involved the heating of a suspension of electrolyte and zinc particles (30 mesh), while stirring the mixture. The electrolyte/zinc particle mixture was held at 90 ° C for 24 hours, and then filtered to remove the zinc particles. To replace water that was lost by evaporation, distilled water was added to the electrolyte.

After the electrolyte purification, the zinc concentration was measured by titrating the solution with EDTA. Eriochrome T indicator recorded the endpoint of the titration. This procedure takes advantage of the stronger bonding forces between zinc and EDTA than zinc and Erio T. When the concentration of EDTA is small, there is free zinc in the solution, thus, EDTA bonds to the available zinc. As the concentration of EDTA increases, the proportion of free zinc decreases; finally, no free zinc exists, and the addition of more EDTA causes the decomposition of the Erio T-zinc complexes. This decomposition causes a color change from purple to blue, marking the endpoint of the titration. Once the concentration of the electrolyte was determined, the solution was stored in a polypropylene container until use. Just before use, the stock solution was diluted to the required zinc and KOH concentrations using water or a KOH solution.

4.3 Details of Operation

Before operation, the electrolyte chambers of the channel flow cell or the rotating cylinder cell were sparged with 99% nitrogen for about 20 minutes, a procedure that stripped any dissolved oxygen or carbon dioxide out of the electrolyte. In the flow system, sparging

was applied in the reservoir throughout the experiment, keeping the level of gas flow low so that the bubbles would not influence the flow pattern. In the rotating cylinder cell, the cell was blanketed with nitrogen during the experiment.

After the rotating cylinder cell was sparged, the cathode was inserted, fastened into place, and electrolyte flow started. In the channel flow cell, the cathode was inserted and epoxied in place and then polished. When the polishing was completed, the electrode connections were checked, flow was started, and the valves were bled to remove any entrapped air. Once a constant flow condition was achieved and no air pockets remained in the cell, the flow rate was set by adjusting the entrance valve, and the current was started. Generally a charge of about 50- 100 coulombs/cm^2 was passed during the course of an experiment, although less charge was passed in runs designed for evaluating the surface profile. The charge was passed galvanostatically, and the potential was recorded. An IBM P/S 2 computer was used to control the experiments and record the transients. A charge density of 50 coulombs/ cm^2 corresponds to a deposit thickness of 25 μm if a compact deposit is formed; however, deposits were frequently thicker because of the porous nature of mossy deposits.

In the channel flow cell, the development of the deposit morphology was observed *in-situ* using a video recording system, which required additional procedures. First, the fiber-optic lights were turned on and adjusted to illuminate the sample. Then the video camera, monitor, and video recorder were activated, and the microscope was focused so that a clear image appeared on the video screen. The illumination was then adjusted to best reveal the substrate structure. The video recorder was then switched on, and the experiment begun. The recorder was almost always set to record in real time. Videotapes could be edited later to demonstrate the specific events.

4.4 Preparation of Samples for Surface Analysis and Electron Microscopy

Immediately after the experiment, the cathode was removed from the cell, washed in distilled water, and dried in acetone or methanol. The cathode was then screwed onto the profilometer jig, which is shown in figures 4.1 and 4.2, aligned, and the profile was taken. These data were collected using an IBM PS/2 computer for later analysis. The electrode was then stored in a dust free container before being prepared for scanning or transmission electron microscopy. In SEM, the emissive mode was used, and in TEM, the bright field, darkfield, and diffraction modes were employed.

The deposit cross section and the surface morphology were examined by scanning electron microscopy. X-ray diffraction was used to determine the changes in preferred orientation. No special preparation was necessary to observe the surface morphology nor to examine the crystallography. The cross section was prepared by mounting the electrode in Konductomet (Buehler) resin and cutting a cross section using an Buehler- diamond slow saw. The cross section was then polished, etched with 2% nital solution (4 ml HNO_3 in 196 ml ethanol), and mounted on a scanning electron microscope holder using colloidal graphite, which provided the necessary electrical connections. Micrographs were taken at several magnifications, generally not exceeding 2000X. The x-ray diffraction was performed using a diffraction range of 10-90 degrees, with a 0.1 degree step/second.

For transmission electron microscopy, a thin specimen had to be prepared. The procedure for preparing samples made up entirely of moss is very simple. The moss was scraped off the electrodeposit and placed in a pestle. The fragile deposit was then ground up so that only a powder remained. The powder was then suspended in methanol and picked up by an eyedropper; following which the suspension was poured through a 3 mm diameter carbon coated 200 mesh (62 μm hole size) copper grid. Some particles attached themselves to the grid: the edges of these particles were observed by the transmission electron microscope after

the solvent had dried.

Figure Captions

4.1 Profilometry setup showing profilometer, chart recorder and profilometry jig.

4.2 Closeup of the jig used to hold the rotating cylinder samples

XBB 906-4628

Figure 4.1

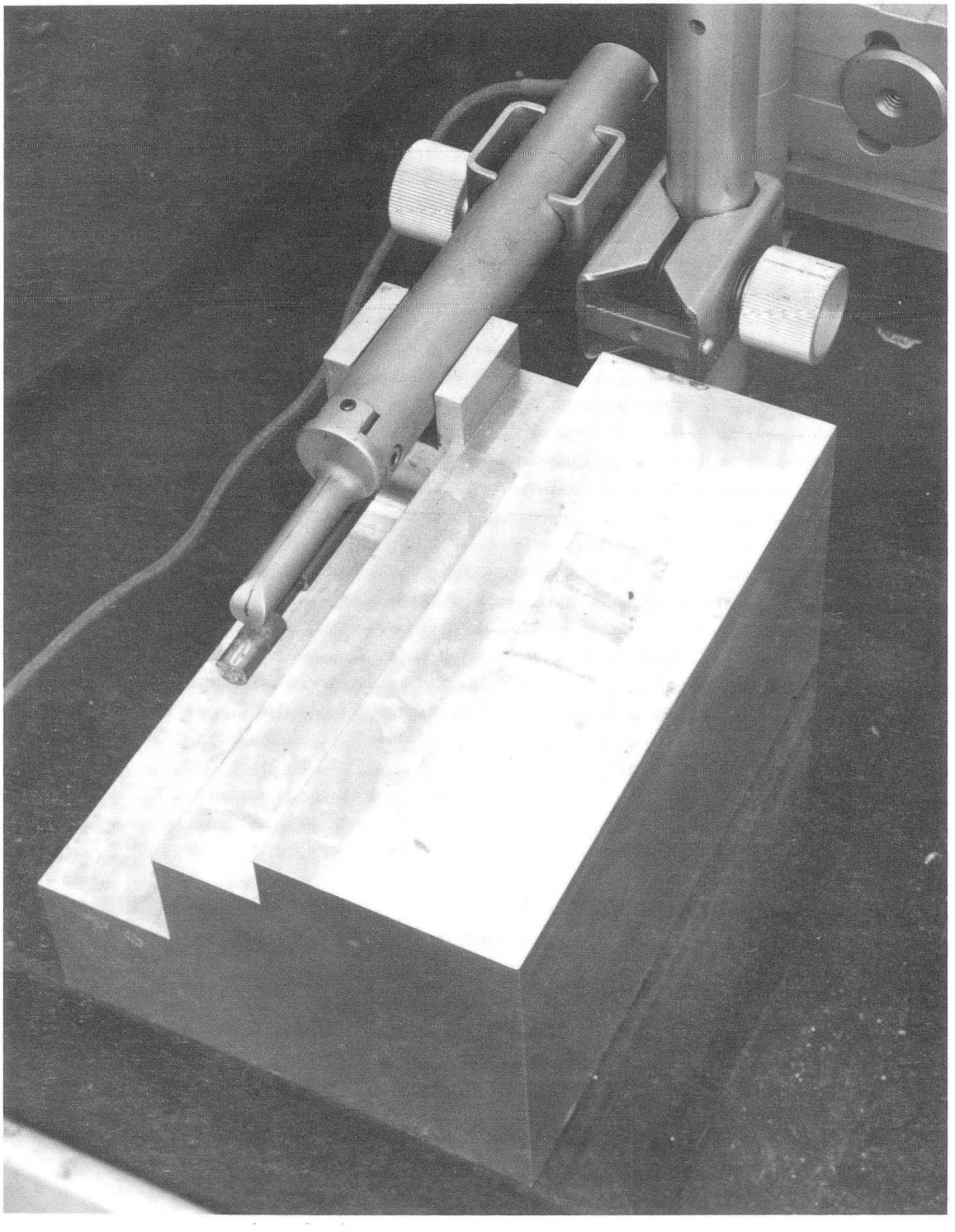

XBB 906-4632

Figure 4.2

RESULTS AND DISCUSSION

5.1 Types of Morphology Found in Alkaline Electrolytes

Many of the types of morphology that are seen in acidic electrolytes are also found in alkaline zincate media. As shown in Figure 5.1, striations are formed in alkaline electrolytes, a finding confirming that hydrogen evolution is not a criterion for striation formation(50). These striae are similar to the "flat" striations generated when using acidic media. There is no evidence of bubble evolution on the macroscopic scale nor is there any sign of self corrosion (which would be reflected by rounded crystal planes and less distinct surface features), unlike in the deposit produced from a bromide electrolyte that is also pictured in Figure 5.1.

On the microscopic scale, zinc deposits formed from alkaline electrolytes are initially characterized by well formed hexagonal crystallites, as shown in Figure 5.2. The number of crystallites is greater when depositing at a higher current density, and the average size of the roughness elements is smaller.

Moss can be seen in the deposit from alkaline media (Figure 5.1) and in Figure 5.2(e). This morphology has initiated in the area of both lowest current density and lowest flow rate, and is not found on the deposit taken from acidic media. As shown in Figure 5.2, moss appeared *earlier* when the current density is lower. These nodules are much higher than the rest of the surface, so it appears that the macroscopic roughness of the surface is *larger* as the current density is reduced, an unexpected result.

5.2 The Appearance of Zinc Moss

To ascertain that mossy zinc initiation is not merely the result of the cell geometry, moss was also generated in a channel flow cell. In the channel geometry, there are no stagnation points on the electrode surface, unlike in the rotating disk system (48). Moss consistently initiated at the lowest current density portions of the electrode, as shown in figure 5.3. As depicted in both Figures 5.3 and 5.4, the mossy portions of the deposit were characterized by a porous, filamentary structure, while the remaining deposit is distinguished by large zinc crystallites.

When running the flow cell experiments, the deposit appeared matte and grey colored to the naked eye for several hours before the black nodules characteristic of moss appeared. This observation is confirmed in Figure 5.5, which are three optical micrographs of a cross section of a zinc deposit made using a copper substrate. Three strata are evident in these low power micrographs (nominal magnification ~ 200X): (1) the copper substrate; (2) a well packed zinc deposit (hereafter referred to as the compact layer); and (3) a mossy layer. The compact layer is about 75 μm thick; the mossy layer is initiated on top of this formation, confirming the initial, visual observations.

5.3 The Characterization of Zinc Electrodeposits

Understanding the changes that are taking place may provide insights as to *why* the morphology switches drastically. As pictured in Figures 5.4 and 5.6, the initial crystalline deposit changes to a porous filamentary structure. The porosity of moss is estimated to be about 70-90%, regardless of deposition conditions. The approximate area of the moss (as estimated from a measurement of the pore sizes in Figure 5.6) is 6 $cm^2/\mu m$ deposited (0.8 m^2/g), a result in general agreement with the BET measurements done by Justinijanovic

and Despic (52), who stated that the specific surface area of their deposits ranged from 0.4 - 1.2 m^2/g. The major structural elements are zinc filaments that are about 100 nanometers in width. The electron diffraction pattern, shown in Figure 5.7 indicates that mossy zinc is mainly metallic zinc. This pattern, as indexed in Figure 5.7, is consistent with zinc metal oriented on the $\{2\bar{1}\bar{1}0\}$ zone axis. However, because of the method of sample preparation, the zone axis orientation is not indicative of the orientation relationship between moss and the substrate. The extra rings in the diffraction pattern are indicative of a surface layer of zinc oxide that is formed upon exposure to air.

Figure 5.8 shows a bright field transmission electron micrograph of a nodule of moss whose image was formed by allowing multiple beams to pass through the objective aperture of the microscope. The lattice fringes running vertically along the particle are spaced at a distance, in agreement with calculated values for the zinc lattice. While the moire fringes extending horizontally across the figure are also consistent with a zinc lattice, their discontinuity indicates that mossy zinc is heavily dislocated. The indistinct crescent shaped fringes running vertically may reveal the presence of dislocation loops.

Figures 5.9 and 5.10 depict the progress of deposition on a platinum surface together with the corresponding x-ray diffraction pattern. The diffraction patterns plotted are the average of five scans taken right after the zinc crystals were grown. Multiple scans were taken to ensure that a statistically significant number of crystallites were sampled to get the preferred orientation. Only peaks corresponding to platinum and zinc were detected, with the sole exception of a small zinc oxide peak that is not detected in the first scans and grew as more x-rays were taken. Therefore, it can be concluded that the latter peak is a result of exposure to air. As the deposit thickened, the peaks caused by platinum reflections decreased in intensity, while the total intensity of the zinc peaks increased. However, the relative intensities of the Zn $\{0002\}$ and $\{10\bar{1}3\}$ peaks increased dramatically in relation to other crystal planes, as shown in Figures 5.11, 5.12, and 5.13. As more charge is passed, some peak broadening is

observed, as depicted in Figures 5.14 and 5.15. This widening may be indicative of a reduction of the grain size. These defects would provide preferred nucleation sites for a new zinc crystal phase. Initially, the preferred orientation of the zinc crystal is $\{11\bar{2}0\}$ and $\{11\bar{2}2\}$, a result in agreement with the work function calculations of Pangaroff(53) and with the results of Mackinnon and co-workers(54). Once mossy zinc is initiated, the relative intensity of the $\{0002\}$ and $\{10\bar{1}3\}$ reflections became larger. As the relative intensity is dependent on the number of crystals in the sample, it can be concluded that the preferred orientation of moss is $\{0002\}$ and $\{10\bar{1}3\}$.

So far, it has been shown that the change in morphology is merely accompanied by a change in crystal orientation. This change occurs after the passage of a substantial amount of charge, and is characterized by the emergence of a small- grained, fast growing crystal. The next section will deal with the events occurring when moss is initiated.

5.4 The Initiation and Propagation of Moss

In figures 5.16 and 5.17, the initiation of moss is illustrated. Figure 5.16, taken from an in-situ videotape, shows that the surface becomes dominated by protrusions emerging from the fine roughness (an observation in accordance with Kindler's work (55)) and growth fronts, which are microscopic steps in the crystal (see Figure 5.3). Initially, these roughness elements merely grow in amplitude. Once the amplitude reaches a critical height, black masses appear at the base of the protrusion. These crystals grow over the existing protrusion, and become the initial elements of moss. In figure 5.17, this process is shown more clearly. The photos of the 20 μm deposit (showing the same protrusion at three different magnifications) indicate that the mossy structure first initiates at the base of a protrusion. As more charge is passed, the spongy deposit grows over the protrusion, forming a mushroom shaped deposit.

Once mossy nodules reach a critical height, they are favored for growth and cover the surface, a process that is depicted in Figures 5.18, 5.19, and 5.20. As shown in Figure 5.16, these nodules of moss grow at a rate of several hundred microns per hour when they are first initiated; in fact, the growth of moss nodules is visible to the naked eye. Once the mossy islands become visible, the growth of the compact layer is stopped in the immediate area of the protrusion but continues farther away. Under the deposition conditions reported in the legend of Figure 5.16, moss first appeared at the downstream edge after about 30 minutes, at which time the compact layer's thickness is nominally 8 μm, yet, in the area observed in Figure 5.16, the compact layer continued to grow until the moss element is about 50 μm in diameter.

As shown in Figure 5.18, mossy zinc nodules are initiated only over a short time interval locally, although the propagation time over the entire electrode can be long. Once mossy zinc nodules are initiated, they grow without regard to the direction of flow, as depicted in Figures 5.16 and 5.19. The initiation process only occurs over a short time interval because these nodules quickly grow to the height of the boundary layer and affect the flow to the surface (note that there is no new moss initiation in Figure 5.19). The largest nodules appear to grow at the fastest rate probably because they act as sinks for the zinc reactant. Even small nodules of moss can be swamped by the larger packs; this phenomenon is shown in Figures 5.18 and 5.19. At the end of one hour of deposition under the conditions noted in Figure 5.19, the moss nodules were about 85 μm high which is 5 times the average growth rate of the compact deposit (based on the current density). In comparison, the compact layer grew 9 μm over the same time period. Once the nodules are comparable in size to the boundary layer thickness, they affect the flow field in their vicinity. The resulting eddies increase the mass transport coefficient to the compact layer. If mossy zinc was caused by an inhibiting layer of zinc oxide blocking the surface, as alleged by Cachet and Wiart, this film would be dissolved in the vicinity of the eddies and the initiation of mossy zinc would be continuous. Mossy zinc nodules increase both the effective amplitude and wavelength of the roughness, effects that

will be discussed later.

5.5 The Effect of Roughness on the Development of Moss

In the previous section, it was shown that moss is initiated around existing large protrusions, that it acts as a sink for current preventing the compact layer from growing, inhibiting further moss nucleation, and that once initiated, it covers the surface. In this section, the appearance of the deposit will be correlated with changes in the profile parameters.

In Figure 5.21, the progression of moss over the surface is shown along with micrographs of mossy nodules and of the compact layer. In this case, moss is initiated very quickly, after less than 1 μm nominal deposit thickness was achieved. At these low current densities, the surface is dominated by large protrusions even when only a small amount of charge has been passed, as depicted in Figure 5.22 which shows the change in roughness as moss is initiated. When the average deposit thickness in about 1 μm, as depicted in the middle profile, the average roughness (the average deviation from the mean) is 8.5 μm and the average wavelength is 45 μm. This average deviation from the mean is less than 12% of the boundary layer thickness for the deposition conditions. The skewness, a measure of the symmetry of the profile about the mean line (56)

$$\text{skewness} = \frac{1}{(R_q)}\frac{1}{N}\sum_{1}^{N} Y_i^3 \qquad (5\text{-}1)$$

where: N= number of ordinates chosen in a profile length

Y_i= profile ordinate

R_q= root mean square roughness

is about 1 for the same profile (skew=0 indicates an evenly distributed profile), a finding

confirming that the main surface feature are large protrusions.

As the current density is raised, moss is initiated after the passage of a substantially greater amount of charge. In Figure 5.23, the progression of the deposit appearance from compact to mossy is shown. The deposit is initially matte to the naked eye, as shown in the photographs taken when 10 and 20 micrometers of zinc have been plated. As the nominal deposit thickness increases, nodules of moss start appearing on top of the compact layer. When 60 microns of zinc have been plated the surface is covered with nodules of moss and appears black to the naked eye.

The accompanying profiles, depicted in Figure 5.24, show a surface that is initially smooth and that steadily increases in roughness until moss is initiated (around 30 μm deposit thickness). Once the surface becomes mossy, the roughness becomes drastically greater, an expected result, because of the fast growth rate of mossy crystals and the high percentage of moss. The variation of the average roughness with deposit thickness is shown in Figure 5.25. As deposition commences, the roughness rises as the compact layer becomes thicker, because electrodeposition at most conditions is unstable unless additives are present(39). Once moss is initiated, the roughness increases at a slower rate until the spongy nodules are the dominant feature in the morphology, as indicated by the positive value of the skew (0.2). Subsequently, the roughness drastically rises with time.

The variation in the autocorrelation function, a measurement of the similarity between two identical but laterally shifted profiles (56), is presented in Figures 5.26 and 5.27. Initially, the autocorrelation function is characteristic of a brightly polished surface, as expected, since the surface was electropolished to a roughness amplitude of 1 μm. The correlation length, a wavelength sensitive parameter defined as the shift distance where the autocorrelation function or its envelope first drops to 10% of its value at the zero- shift position (56) and a measure of whether two points on the surface are independent of each other, is approximately 300 μm. The correlation length drops to about 40 μm when the dominant surface feature is small

zinc protrusions. Once moss becomes the prevailing surface morphology, the correlation length rises to around 100 μm.

The amplitude density function (the measure of the probability density of profile amplitudes (56)) corresponding to Figure 5.23 is depicted in Figure 5.28. The range of amplitude heights is initially around 5 μm, an expected result for a brightly polished surface. Once zinc deposition begins, the width of the gaussian curve widens and reaches about 20 μm when 30 μm have been deposited, after which it remains constant until moss covers the surface. The shapes of the amplitude density function and the autocorrelation function are characteristic of an amplitude modulated surface, as expected because of the random nature of zinc nucleation. The observation that the size range of the roughness elements remains constant together with the observed slight rise in the autocorrelation length may indicate that there is some merging of the roughness elements under these deposition conditions. In both the low and high current density cases, the wavelength and roughness reached critical values of approximately 10 μm roughness and 40 μm correlation length before mossy zinc is initiated. Therefore, it can be concluded that the roughness parameters of the surface are factors influencing the growth of mossy zinc.

5.6 The Effect of the Deposition Conditions on the Formation of Mossy Deposits

Is moss a single type of morphology or is it a conglomeration of several different structures? Figure 5.29 shows moss obtained at two drastically different deposition conditions: (1) 50mA/cm^2, 1000 rpm, that is about 40 % of the limiting current density, and (2) 4 mA/cm^2, no flow, that is a repeat of an experiment performed by Naybour(12). Both deposits show the same distinctive mossy zinc morphology characterized by a porous, filamentary structure.

As represented in Figure 5.30, moss exists in both saturated and unsaturated zincate electrolytes, where, if a passive oxide precipitate is a contributing factor to mossy zinc forma-

tion, this layer would *not* be formed when an unsaturated solution is used. In fact, the observed compact layer is significantly thinner when the solution is not saturated with zinc oxide.

Is the formation of the compact layer caused by depositing on a foreign substrate? Figure 5.31 shows representative cross sections of a zinc electrodeposit on two different substrates, copper and zinc. In spite of being next to each other in the periodic table, copper and zinc have drastically different lattice parameters(57). The average compact layer thickness, measured using data taken from several photographs is 17 and 19 μm for the copper and zinc substrates respectively. A similar compact layer thickness is obtained when a stainless steel substrate is used.

Figure 5.32 depicts the mossy structure when three different supporting electrolyte concentrations are used. In the deposit obtained using a 3 M supporting electrolyte, all three layers of the deposit are shown: the substrate, which appears as a uniformly dark, featureless surface, the compact layer, characterized by the hexagonal crystal planes, and the mossy zinc structure, distinguished by its porous structure.

In Figure 5.33 the corresponding cross sections for the 3 M and 12 M concentrations of KOH are depicted. When the supporting electrolyte concentration is 3 M, the compact layer is drastically larger than when a 12 M supporting electrolyte is employed. In the left hand photos of Figure 5.33, a nodule of moss clearly extends from a protrusion in the compact layer, confirming earlier results. The cross section measurements are depicted graphically in Figure 5.34, where it is also shown that the critical roughness needed to generate moss is much smaller when 12 M KOH is the supporting electrolyte. When 3-12 M KOH is the supporting electrolyte, the solution is well supported, so migration has no effect on the limiting current. Therefore, it appears that the free hydroxide concentration has a drastic effect on the deposition of moss, a result confirmed by the work of Putt (58).

Figure 5.35 shows that the compact layer is smaller at low fractions of the limiting current, an unusual result, because the roughness is expected to increase with current density. This result is in agreement with the work of Naybour (12) who found that mossy zinc is generated quickly at low current densities. It is also in agreement with the trends noted in Section 5.5. At low current densities, the morphology is dominated by large protrusions that grow independently; an observation noted by both Popov (23, 24, 25) and by Naybour (13). In this laboratory, Kindler (55) stated that *The percent of large protrusions decreases with increasing current density.* As the current density increases, more protrusions are nucleated and some of the roughness elements merge. As a result, the effective roughness amplitude increases at a slower rate than if a smaller current density is employed and the wavelength of roughness increases. Since the roughness is not increasing as quickly, the amount of charge passed before moss is initiated can be greater. As shown in figures 5.36 and 5.37, the roughness required before moss is initiated is independent of the current density, and much smaller than the boundary layer thickness (72 μm for a rotation rate of 250 rpm and 45 μm for a rotation rate of 500 rpm).

Figures 5.38 and 5.39 show the change in the compact layer thickness with current density at the same fraction of the limiting current. At low current densities, the compact layer is thin, because the nucleation density is small and the protrusions grow without melding with their neighbors. Therefore, roughness builds up to the critical point more quickly. As the current density is raised, more roughness elements exist, the average size is lower, as noted by Barkey (39), and there is melding of protrusions. These factors combine to lower the effective roughness and increase the effective wavelength of the profile. Figures 5.40 and 5.41 show similar results at a higher fraction of the limiting current density. Once again, the critical roughness before moss is initiated is approximately constant.

Figure 5.42 is a comparison of the variation in the compact layer thickness with fraction of the limiting current density for a low applied current density. When the applied current is

small, roughness elements grow independently, and the roughness amplitude increases with fraction of the limiting current density(39). Since the roughness amplitude increases at a greater rate when the fraction of the limiting current density is high, the compact layer will decrease in size, a result that is depicted in Figure 5.43.

The situation is reversed when the current density is high as illustrated in Figure 5.44. At these conditions, there is a much higher density of roughness elements that have a high tendency to meld, and the compact layer's thickness increases with the fraction of the limiting current density, as shown in Figure 5.45. The melding of roughness elements was confirmed by videomicroscopic records showing that the entire surface changed over a short time interval.

Can the thickness of the compact layer be influenced by using a modified charging method? Figure 5.46 shows the variation of the compact layer with changing current density. Cachet and Wiart (28) stated that there is a precipitated zinc oxide layer that gradually blocked the electrode. This layer is "activated" at high current densities, and so moss didn't form. Mayer (59) looked for the oxide layer using a sensitive RAMAN technique, and stated that: *During a cathodic sweep, the (oxide) film is observed down to -1.35 V and is not present at potentials where a cathodic current is passed.* This observation is in agreement with the work of Hamnett and Mortimer (32). If zinc deposition took place through an oxide sublayer, then moss would form immediately when the current is reduced from a regime when moss didn't form and would not initiate at all when the current density is raised. However, Figure 5.46 shows that there is no effect on the onset of moss when the current density is raised after deposition commenced at a lower current density. When the current density is lowered from a higher level, as shown in the left hand photos of Figure 5.46, the onset of moss is delayed, a finding which suggested that the roughness developed by depositing at the initial current density plays a role in the onset of moss and that Mayer's results are correct.

Oswin and Blurton (2) indicate that the equilibrium potential shifts cathodically when the deposit type changes from compact to mossy. This finding is in agreement with the work of Ashmetow and Wosdwishenskij(6) who found that the equilibrium potential of the basal plane is cathodic to the side planes. They stated that this shift is caused by the adsorption of hydroxide ions, that makes the dissolution of zinc easier. However, hydroxide ions have an effect on the potential of the zinc electrode as well. Dirske (45) found that as the bulk concentration of hydroxide increases, the potential for zinc electrodeposition shifts cathodically, therefore, if hydroxide ions play a role in the initiation of moss, there should be a cathodic shift in the electrode potential. Figure 5.47 shows the potential transient for a galvanostatic experiment. As the roughness increases, the potential becomes less cathodic; however, the rate of change slows drastically just before moss is initiated. Because the roughness is increasing drastically when moss is initiated, it can be concluded that the potential for zinc deposition must be shifting in the cathodic direction, otherwise, the recorded potential would become lower.

5.7 Analysis

The x-ray and SEM observations suggest that mossy zinc is a conglomeration of zinc crystals, that is, the nucleation rate of zinc crystals is higher at the base of a protrusion than it is at the peak (see Figure 5.17). According to Erdey-Gruz and Volmer(55), the rate of nucleation, J, is proportional to the nucleation overpotential, η_n, by the relation:

$$J \alpha \exp(-1/|\eta_n|) \qquad (5\text{-}2)$$

for 2-D nucleation, the extension of layers, or

$$J \alpha \exp(-1/|\eta_n^2|) \qquad (5\text{-}3)$$

for three dimensional nucleation. For J to increase, the magnitude of the nucleation overpotential, η_n, must become greater, so the nucleation overpotential must become more cathodic. Because the nucleation overpotential is a component of the total surface overpotential(7), it follows that the exchange current density must also increase. Furthermore, to keep an equipotential surface, the standard potential of the zinc reaction must increase in the cathodic direction.

The x-ray results indicate that when mossy zinc is deposited, there is a change in the structure of the depositing metal. Pangaroff(53) calculated the work function for the nucleation of crystal planes. It was found that in a hcp crystal, the predominant crystal orientations should be $\{11\bar{2}0\}$ and $\{10\bar{1}0\}$ when the overpotential is high, because the nucleation overpotential for deposition of these planes is the lowest. However, as the overpotential decreases, the formation of the $\{0002\}$ and the $\{10\bar{1}1\}$ planes becomes more favored, because the work function of the $\{11\bar{2}0\}$ and $\{10\bar{1}0\}$ planes rises faster with decreasing overpotential than the previously mentioned planes. Adsorption of surface active species can lower the nucleation overpotential for the less favored species, so it is possible that a difference in surface coverage may account for the change in crystal orientation. Since the effective crystal packing density in the crystal types associated with moss is greater, these would be favored for growth once nucleated (60).

The experimental data taken in this lab and by Putt (58) suggest that hydroxide ions play a role in mossy zinc initiation. While Grahame(61) found that hydroxide ions are not generally adsorbed, *zincate ions are specifically adsorbed* when zinc is reduced(1). The reduction of a single zinc atom from zincate leaves four hydroxide ions near the surface. After desorption, these ions are transported away at a rate limited only by the current density within the limits set by the mass transport conditions. However, is is possible that the rate at which these ions are transported away changes locally, causing a local change in the surface coverage of hydroxide ions. Additives are known to work in this manner; Kruglikov (62, 63)

demonstrated *that the flux of an additive to the surface and not the bulk concentration* determined the change in polarization. In this case, the hydroxide ions would enhance both the rate of nucleation and the rate of growth. Deposition to a partially blocked surface was studied by Jordan(62); this would be an analogous problem. Even a small change in the concentration of hydroxide ions can cause a drastic change in the reaction characteristics, as is the case for additives, which typically have concentrations on the order of mM.

Both Farr et. al.(42, 43) and Bockris et. al.(44) found that the exchange current density increases with the hydroxide concentration. Dirkse (45) and Isaacson (46, 47) confirmed that the potential of the zinc reaction shifted in the negative direction as the concentration of supporting electrolyte became greater. Both of these trends in the reaction parameters are predicted by the analysis at the beginning of this section. Therefore, a local change in the hydroxide concentration can have several effects: (1) it can lower the nucleation overpotential for the less favored planes; (2) it can enhance the rate of the zinc deposition reaction; (3) it can shift the local equilibrium, causing a lowering of the interfacial zinc concentration; and (4) it shifts the potential of the zinc reaction cathodically.

Using Barkey's model(39), the differences in the hydroxide concentration between the peaks and the valleys can be estimated. Laplace's equation applies for both the potential and the zinc concentration, and the hydroxide flux, N_{OH^-}, is related to the zinc flux, $N_{Zn(OH)_4^{-2}}$, at the surface using the relation:

$$N_{OH^-} = -4N_{Zn(OH)_4^{-2}} \qquad (5\text{-}4)$$

Because the solution is well supported, the migration component of the zinc flux can be neglected; however, migration must be included in the calculation of the hydroxide flux. Therefore equation 5-4 becomes:

$$i\frac{t_{OH^-}}{nF} + D_{OH^-}\frac{\partial C_{OH^-}}{\partial z} = -4D_{Zn(OH)_4^{-2}}\frac{\partial C_{Zn(OH)_4^{-2}}}{\partial z} \qquad (5\text{-}5)$$

Using the Barkey solution for the concentration and the potential and concentration fields, the hydroxide concentration at the peaks and the valleys can be determined by substituting into equation 5-5. The difference in hydroxide concentration is given by the following relation:

$$\Delta C_{OH^-}(\text{peak–valley}) = -4\frac{D_{Zn(OH)_4^{-2}}}{D_{OH^-}}\Delta C_{Zn(OH)_4^{-2}} - (i_p - i_v)t_{OH^-}\frac{\delta}{nFD_{OH^-}} \qquad (5\text{-}6)$$

This equation assumes that the boundary layer thickness (δ) is much greater than the amplitude of roughness (A) an assumption supported by the results presented in Figures 5.36 and 5.37. The boundary layer thickness, as calculated from well known correlations, is typically 4-10 times the measured roughness of the scraped profile (cf. Figures 5.36 and 5.37). Equation 5-5 also assumes that the solution is well supported, and the validity of this assumption is confirmed by the magnitude of the transference number for the "free" zinc ion species, which was calculated to be on the order of 0.01.

The difference in current density between the peaks and the valleys, $i_p - i_v$, can be evaluated by calculating the value of the relation

$$i - i_a = -\sqrt{2}\kappa\omega\phi^p A\sin(\omega_x x)\sin(\omega_y y) \qquad (5\text{-}7)$$

at both the peaks and at the valleys(39). The above equation is derived from Barkey's solution to Laplace's equation for the potential and for the concentration. When this term is evaluated, the equation for the difference in the hydroxide concentration becomes:

$$\Delta C_{OH^-}(\text{peak–valley}) = -4\frac{D_{Zn(OH)_4^{-2}}}{D_{OH^-}}\Delta C_{Zn(OH)_4^{-2}} + 2\sqrt{2}\kappa\omega\phi^p At\frac{\delta}{nFD_{OH^-}} \tag{5-8}$$

where

$$\Delta C_{Zn(OH)_4^{-2}}(\text{peak–valley}) = 2C^pA(1 - \exp(-\sqrt{2}\omega\delta)) \tag{5-9}$$

and the perturbation constants are

$$C^p = \frac{\kappa}{nFD_{Zn(OH)_4^{-2}}}\frac{1}{(1+e^{-2\sqrt{2}\omega\delta})}\phi^p \tag{5-10}$$

$$\phi^p = -\frac{\frac{i_a}{\kappa} + RT\frac{i_a}{n^2F^2D_{Zn(OH)_4^{-2}}C_{bZn(OH)_4^{-2}}(1-\frac{i_a}{i_l})} - 2\nu\gamma\frac{\omega^2}{nF}}{1 + RT\frac{\sqrt{2}}{nF(i_l - i_a)}\kappa\omega + RT\frac{\sqrt{2}}{i_a nF\alpha}\kappa\omega} \tag{5-11}$$

as defined in Chapter 2 (39). The change in the hydroxide concentration between the peaks and the valleys of a profile is a function of the boundary layer thickness (δ), the current density (i), the roughness amplitude (A), the wavelength ($2\pi/\omega$), and the fraction of the limiting current density (i/i_l). In addition, the physical properties of the electrolyte are determined by the zinc and supporting electrolyte concentrations. The next few paragraphs will discuss the local changes in hydroxide concentration with these physical properties.

As represented in Figure 5.30, moss is found in both saturated and unsaturated zincate electrolytes. The observed compact layer for deposition at about 40% i_l in a 0.25 M ZnO, 6 M KOH electrolyte is about 3 μm. When deposition is performed using a either 0.5 M ZnO electrolyte at the same fraction of the limiting current density or the same current density, the compact layer thickness is about 15 μm. These results demonstrate that the compact

layer thickness is lower when the electrolyte is farther from saturation, implying that the difference in the hydroxide concentration is greater when a less saturated electrolyte is used. Figure 5.48 confirms that the change in hydroxide ion concentration is more pronounced when the zincate concentration is lower. This greater difference has the added effect that the percentage change in the zincate concentration caused by the shift in the equilibrium would be larger, further promoting the initiation of moss, so it is not surprising that the compact layer decreases dramatically.

Figure 5.49 depicts the dependence of the change in hydroxide concentration on the amount of the supporting electrolyte present. As more supporting electrolyte is added, the diffusion coefficient of the hydroxide ion decreases, while the density and viscosity of the solution increases. As a result, the change in the hydroxide ion concentration between the peaks and the valleys becomes more marked as the supporting electrolyte concentration increases, implying that the compact layer thickness and the roughness required to initiate mossy zinc should decrease. This hypothesis is in agreement with the experimental results presented by Putt (58) and with the results of this investigation as shown in Figures 5.32- 5.34.

As the current density rises, the model predicts that the difference in hydroxide ion concentration will also become greater, a result shown in Figure 5.50. At first glance, this prediction conflicts with both the results in the literature (12) and with the experimental results depicted in Figures 5.35-5.37. When zinc is deposited at low current densities, protrusions grow independently and the average roughness increases quickly with charge passed as shown in Figure 5.22. When the applied current density is raised (see Figure 5.24) there are more protrusions on the surface- these grow and meld with their neighbors, lowering the average roughness and increasing the wavelength. Therefore, when depositing zinc far from the limiting current, the roughness will increase at a slower rate when a higher current density is passed, contrary to what is normally seen in electrodeposition processes in general but conforming with previous work done on zinc in acidic media (22, 49, 50). In addition, the work

function calculations of Pangaroff (53) show that the growth of the predominant crystal planes in mossy zinc is more favored when the current density is lower, suggesting that a smaller difference in hydroxide concentration is required to initiate moss. Both of these factors can result in a higher compact layer thickness or in no growth of moss at all when the current density is raised.

When the interfacial concentration is held constant, the compact layer thickness increases with the applied current density. This result is in agreement with Barkey (39) who found that, at the same fraction of the limiting current density, the roughness is lower when the applied current density is higher. In addition, the buildup of hydroxide is worsened when the current density is lower (at the same fraction of the limiting current density), presumably because of the diminished rate of mass transport away from the electrode. This result is depicted in Figure 5.51. Therefore, it is not surprising that it is easier to obtain moss when the current density and the flow rate are lowered.

Barkey(39) found that the roughness increased with fraction of the limiting current density when the same applied current is used. As shown in Figure 5.52, this analysis indicates that the difference in hydroxide ion concentration is also greater with a higher fraction of the limiting current, so the compact layer would be smaller, a result confirmed by Figure 5.43. When the applied current density is high, the thickness of the compact layer becomes larger with fraction of the limiting current density; however, the roughness results presented earlier show that the average roughness amplitude increases at a slower rate because of the merging of roughness elements.

Figure 5.52 also confirms the observation made by Naybour(12) that moss is not found when the flow rate is high. At high flow rates, the hydroxide builds up on the peaks instead of the valleys, and would undoubtedly be convected away. Therefore, at high flow rates, there would be no buildup of hydroxide ions, and *moss would not form.* This prediction was confirmed on many occasions in our flow cell, where the morphology is dominated by macros-

teps and striations that propagate in the direction of flow.

Why does the compact layer quit growing? Figure 5.53 shows the change in the current density between the peaks and the valleys as protrusions grow. As the roughness amplitude increases, $i_p - i_v$ becomes greater *regardless of the wavelength of the roughness.* This was confirmed in the videomicroscopic experiments where both small nodules of moss cease growing and where the outward growth of moss dominates the lateral growth of moss at long times (see Figure 5.19). In addition, the surface area of moss is at least 6 times the nominal area of the compact layer, so even a small amount of moss can dramatically raise the electrode area. The growth rate of the moss is not limited by mass transport to the electrode, because the surface movement provides additional transport of zincate to the moss, enabling it to grow at a "dynamic" limiting current density, a concept advanced by Barkey and co-workers (64, 65). It can be concluded that the moss acts as a sink for electrons in the metal, driving the compact layer's current density to zero, thus preventing the further growth of the small features.

5.8 Summary

Mossy zinc is a conglomeration of needlelike zinc crystals. It initiates at the least accessible parts of the electrode and grows significantly faster than the compact layer to cover the surface. A substantial surface roughness must exist before mossy zinc deposition commences; varying any process parameters that favor the increase of the roughness amplitude will promote the initiation of a mossy deposit. Once moss is initiated, the process cannot be reversed; however, this transition can be delayed somewhat by the use of modified charging methods that affect the wavelength and magnitude of the roughness(9). Mossy zinc is ohmically advantaged, so the compact layer's growth stops once the moss becomes the dominant surface feature.

It has been shown that a buildup of hydroxide ions in the valleys of a profile play a role in the initiation of mossy zinc. The following process conditions affect the growth of moss:

(1) Increasing the supporting electrolyte concentration **enhances** the hydroxide buildup and **promotes** the growth of moss.

(2) Increasing the current density, while maintaining the same *mass transport coefficient,* results in a lower amplitude and wavelength of roughness, which **decrease** the hydroxide buildup and **discourages** mossy zinc growth.

(3) Increasing the current density, while maintaining the same *interfacial concentration,* results in both less roughness and in a **lower** buildup of hydroxide ions. These two factors combine to **deter** mossy zinc formation.

(4) Lowering the zinc oxide concentration **aggravates** the hydroxide buildup and **encourages** the initiation of moss.

(5) At a constant current density, increasing the mass transport coefficient **decreases** the hydroxide ion buildup and can **prevent** mossy zinc formation.

(6) The use of either a copper, zinc, or a stainless steel substrate **does not affect** the initiation of mossy zinc.

Figure Captions

5.1 Appearance of striations in alkaline solution: top two photos, 0.5 M ZnO, 6 M KOH, Pt substrate, 30 mA/cm^2, 2 hrs, 20 min, Re= 4000, 1600 rpm; bottom photo, 500 g/l $ZnBr_2$, same deposition conditions, 30 min. Rotating disk system: Electrode has a 1 cm^2 area.

5.2 The effect of current density on the deposit appearance: Pt substrate, 0.5 M ZnO, 6 M KOH, Re= 4000, right hand side, 100 mA/cm^2, left hand side, 30 mA/cm^2.

5.3 Appearance of mossy deposits in the center of a flow channel electrode: Cu substrate, 0.5 M ZnO, 6 M KOH, Re= 4000, 3 hrs, 45 min.

5.4 Differences in morphological structure between mossy and non-mossy areas: Cu substrate, 0.5 M ZnO, 6 M KOH, Re= 4000, 3 hrs, 45 min.

5.5 Cross section of a zinc electrodeposit: Cu substrate, 0.5 M ZnO, 6 M KOH, Re= 4000, 3 hrs, 45 min. Top: leading edge; Center: center of the electrode; Bottom: trailing edge.

5.6 Structure of moss at high magnification: 0.5 M ZnO, 6 M KOH, 20 mA/cm^2, 500 rpm, 27% i_l.

5.7 Crystalline structure of zinc moss: 0.5 M ZnO, 6 M KOH, 2.3mA/cm^2, 5% i_l, Re= 275, Ta = 4 X 10^5.

5.8 Lattice fringes in a nodule of zinc moss: 0.5 M ZnO, 6 M KOH, 2.3mA/cm^2, 5% i_l, Re= 275, Ta = 4 X 10^5. 1 cm = 130 Å.

5.9 Progression of zinc moss on a platinum substrate. Process conditions: 0.5 M ZnO, 6 M KOH, 500 rpm, 30 mA/cm^2. (a) after 5 minutes (4μm = nominal deposit thickness); (b) after 10 minutes (8μm = nominal deposit thickness); (c) after 30 minutes (24μm = nominal deposit thickness). Left column: 14.5 X; Right column: 300 X.

5.10 X- ray diffractogram of zinc deposition on a platinum substrate, all peaks of the 10 minute and 30 minute specimens shown in Figure 5.9.

5.11 Variation of peak relative intensity with time: {0002}, {$10\bar{1}0$}, and {$10\bar{1}1$} planes. Conditions are the same as in Figure 5.9.

5.12 Variation of peak relative intensity with time: {$10\bar{1}2$}, {$10\bar{1}3$}, and {$10\bar{2}0$} planes. Conditions are the same as in Figure 5.9.

5.13 Variation of peak relative intensity with time: {0004}, {$11\bar{2}2$}, and {$20\bar{2}1$} planes. Conditions are the same as in Figure 5.9.

5.14 X-ray diffractogram of zinc deposition on a platinum substrate; {0002} peak. Conditions are the same as in Figure 5.9.

5.15 X-ray diffractogram of zinc deposition on a platinum substrate; {$10\bar{1}3$} and {$11\bar{2}0$} peaks. Conditions are the same as in Figure 5.9.

5.16 In situ micrograph of the initiation of moss in a flow channel; 0.5 M ZnO, 12 M KOH (45% KOH), 10 mA/cm^2, Re= 250, V= 12 cm/s, 40% i_l. Flow direction is from left to right.

5.17 Initiation of moss: 0.5 M ZnO, 6 M KOH, 50mA/cm^2, 42% i_l, Re= 1100, Ta = 6.2 X 10^6. These protrusions are of the same protrusion at three different magnifications. Right hand photos: 20 μm deposit thickness; Left hand photos: 40 μm deposit thickness.

5.18 Growth of mossy zinc nodules: 2 mA/cm^2, 0.5 M ZnO, 6 M KOH, Re= 500, V= 24 cm/s, 2% i_l. Flow direction is from left to right.

5.19 Growth of mossy zinc nodules: 10 mA/cm^2, 0.5 M ZnO, 12 M KOH, Re= 250, V= 12 cm/s. Flow direction is from left to right.

5.20 Progression of moss with increasing time: 0.25 M ZnO, 6 M KOH, 15 mA/cm^2.

5.21 Moss at low current density: 0.5 M ZnO, 6 M KOH, 2.3mA/cm^2, 5% i_l, Re= 275, Ta = 4 X 10^5.

5.22 Progression of roughness with increasing deposit thickness: 0.5 M ZnO, 6 M KOH, 2.3mA/cm^2, 5% i_l, Re= 275, Ta = 4 X 10^5.

5.23 Change in morphology with increasing deposit thickness: 0.5 M ZnO, 6 M KOH, 50mA/cm^2, 66% i_l, Re= 550, Ta = 1.6 X 10^6.

5.24 Change in profile with increasing deposit thickness: 0.5 M ZnO, 6 M KOH, 50mA/cm^2, 66% i_l, Re= 550, Ta = 1.6 X 10^6. Rotating concentric cylinder electrode: L= 0.668 cm, D= 0.7 cm.

5.25 Variation of the average roughness with increasing deposit thickness: 0.5 M ZnO, 6 M KOH, 50mA/cm^2, 66% i_l, Re= 550, Ta = 1.6 X 10^6.

5.26 Change in the autocorrelation function with increasing deposit thickness: 0.5 M ZnO, 6 M KOH, 50mA/cm^2, 66% i_l, Re= 550, Ta = 1.6 X 10^6.

5.27 Variation of the correlation length with increasing deposit thickness: 0.5 M ZnO, 6 M KOH, 50mA/cm^2, 66% i_l, Re= 550, Ta = 1.6 X 10^6.

5.28 Change in the amplitude density function with increasing deposit thickness: 0.5 M ZnO, 6 M KOH, 50mA/cm^2, 66% i_l, Re= 550, Ta = 1.6 X 10^6.

5.29 Comparison of the structure of moss in flowing and non-flowing media: 0.5 M ZnO, 6 M KOH.

5.30 Moss in saturated and unsaturated media

mA/cm^2

5.46 Comparison of the compact layer thickness with varying current density

5.47 Potential response to an applied current

5.48 Change in hydroxide concentration with roughness amplitude- effect of zinc concentration: 30 mA/cm^2, 500 rpm, 6 M KOH, $\lambda = 50\ \mu m$. Results calculated from Equation 5-8.

5.49 Dependence of the change in hydroxide concentration on the concentration of KOH: 0.25 M ZnO, 30 mA/cm^2, 500 rpm, $\lambda = 50\ \mu m$. Results calculated from Equation 5-8.

5.50 Dependence of the change in hydroxide concentration on current density: 0.5 M ZnO, 6 M KOH, 500 rpm, $R_a = 10\ \mu m$, $\lambda = 50\ \mu m$. Results calculated from Equation 5-8.

5.51 Change in hydroxide concentration with roughness amplitude: 0.5 M ZnO, 6 M KOH, 500 rpm, 30% i_l. Results calculated from Equation 5-8.

5.52 Dependence of the change in hydroxide concentration on rotation rate: 0.5 M ZnO, 6 M KOH, 30 mA/cm^2, $R_a = 10\ \mu m$,$\lambda = 50\ \mu m$. Results calculated from Equation 5-8.

5.53 Change in $i_p - i_v$ with roughness amplitude: 0.5 M ZnO, 6 M KOH, 30 mA/cm^2, 500 rpm, $\lambda = 50\mu m$. Results calculated from Equation 5-7.

APPEARANCE OF STRIATIONS IN ALKALINE SOLUTION

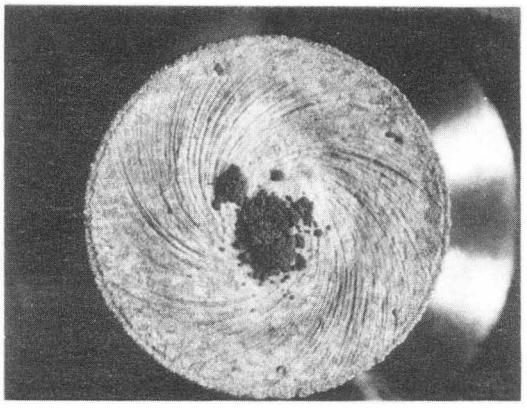

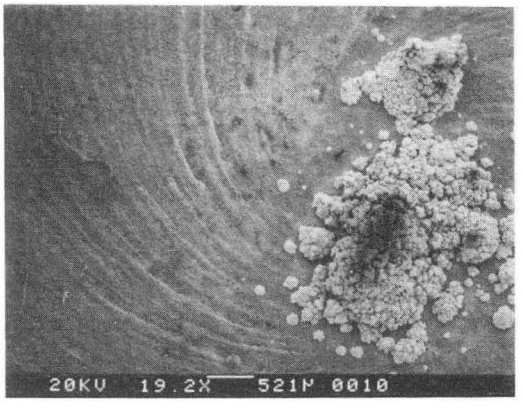

49 g/l ZnO +6M KOH
Platinum substrate, 30 mA/cm**2, 2 hours, 20 minutes, Re=4000.

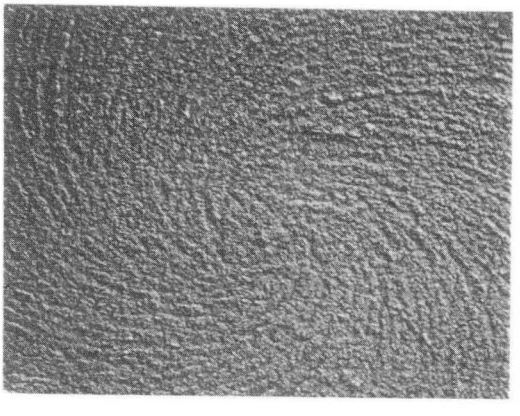

500 g/l $ZnBr_2$
Platinum substrate, 30 mA/cm**2, 30 minutes, Re=4000

XBB 869-6991

Figure 5.1

THE EFFECT OF CURRENT ON THE DEPOSIT APPEARANCE

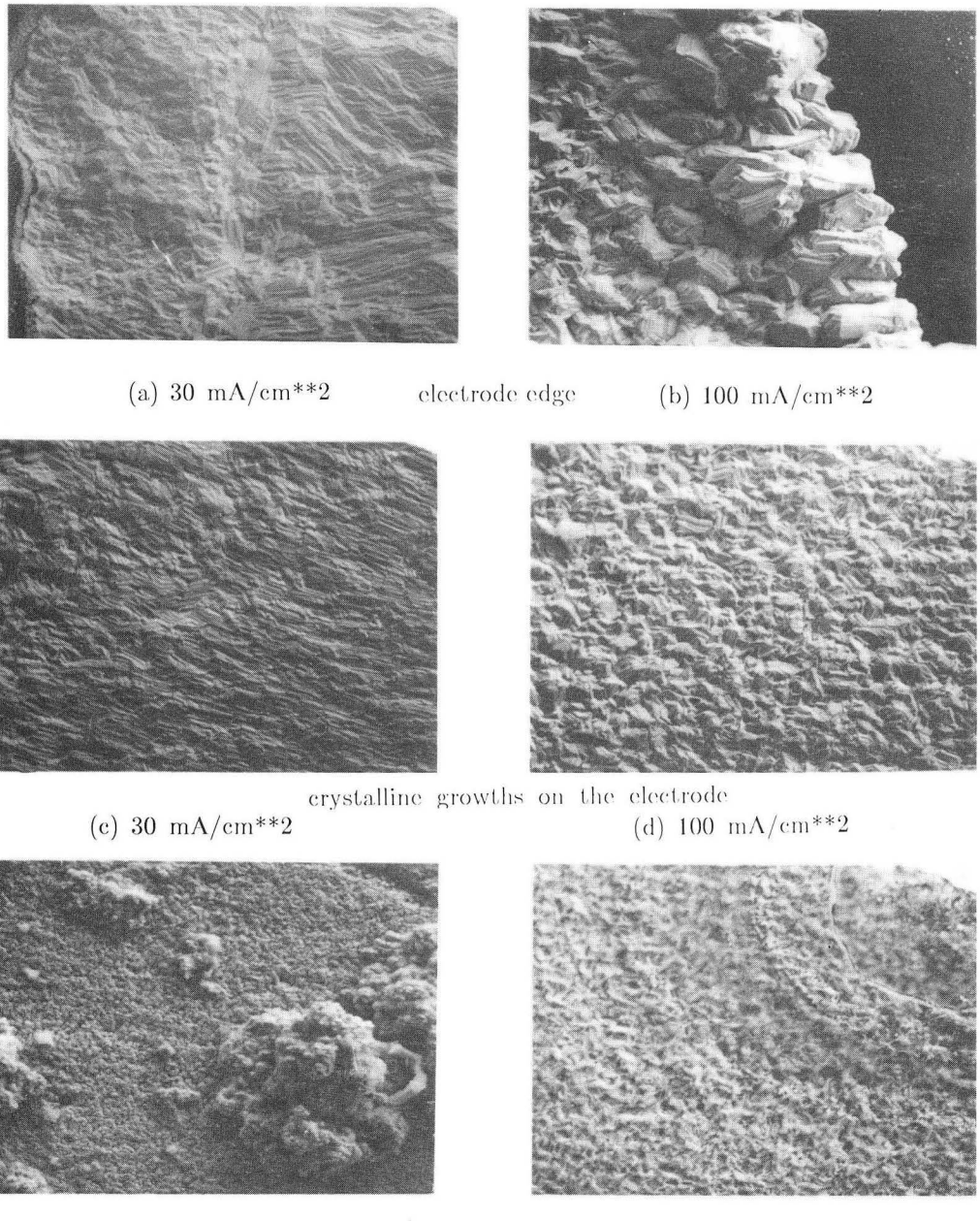

XBB 869-6990

Figure 5.2

APPEARANCE OF MOSSY DEPOSITS

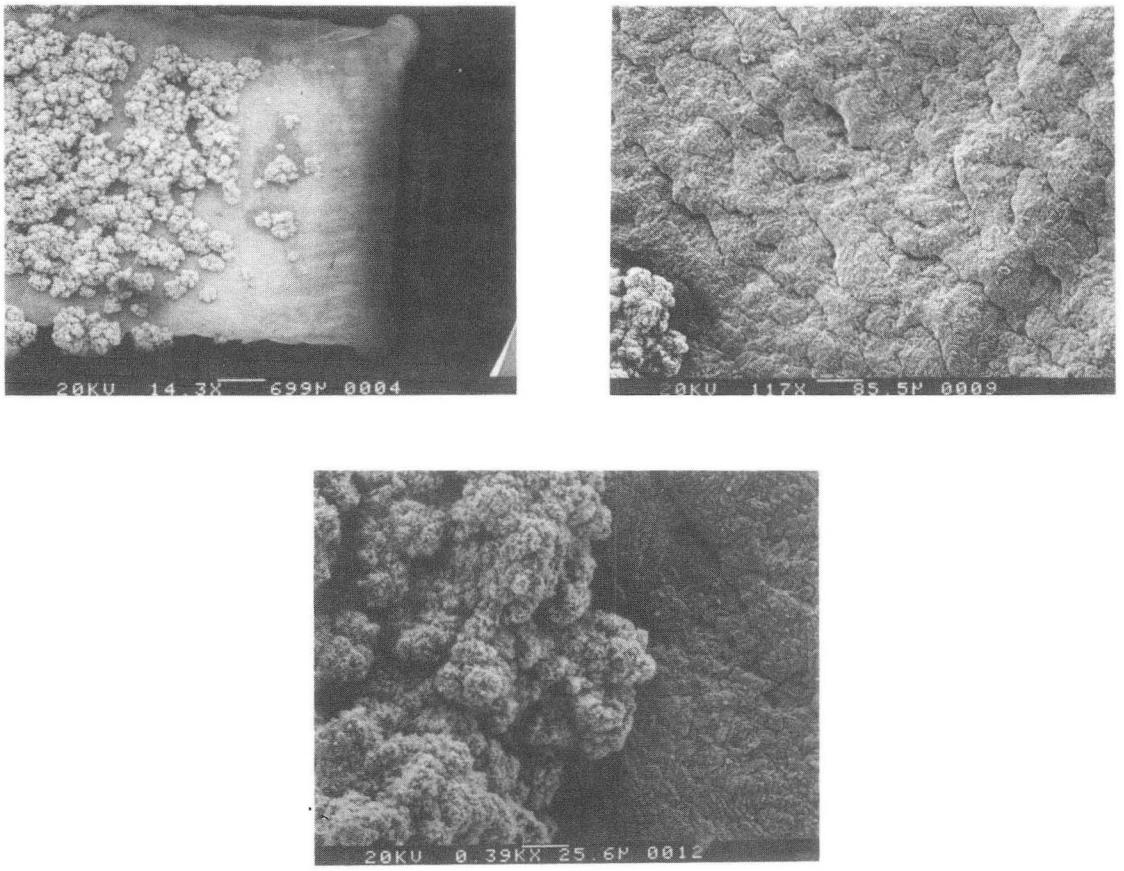

Copper substrate, mossy and non-mossy zinc deposit
30 mA/cm**2, Re=4000, 3 hours, 45 minutes,
49 g/l ZnO +6M KOH

← flow direction

XBB 869-6992

Figure 5.3

DIFFERENCES IN MORPHOLOGICAL STRUCTURE BETWEEN MOSSY AND NON-MOSSY AREAS

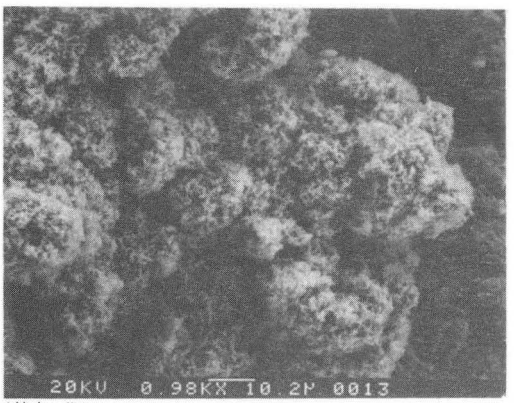

mossy deposit

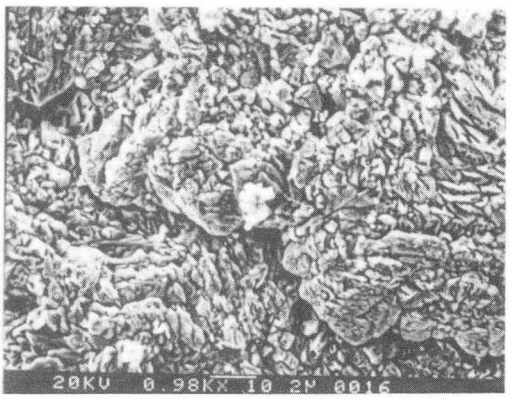

non-mossy deposit

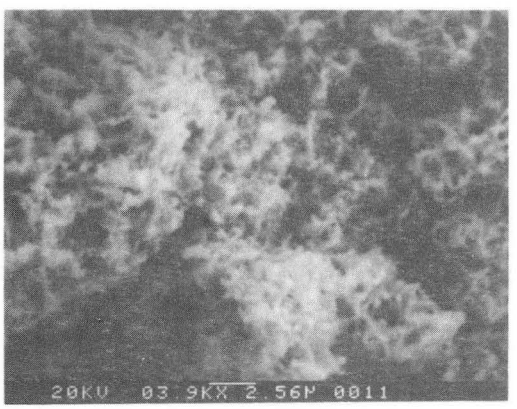

mossy deposit

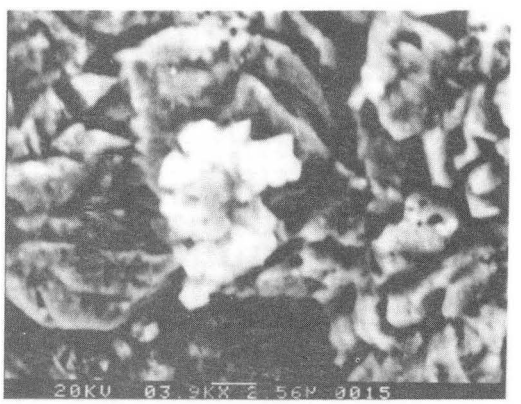

non-mossy deposit

copper substrate, 49 g/l zinc oxide + 6M KOH, 30 mA/cm**2, 3 hours, 45 minutes, Re=4000

XBB 869-6993

Figure 5.4

CROSS SECTION OF ZINC ELECTRODEPOSIT

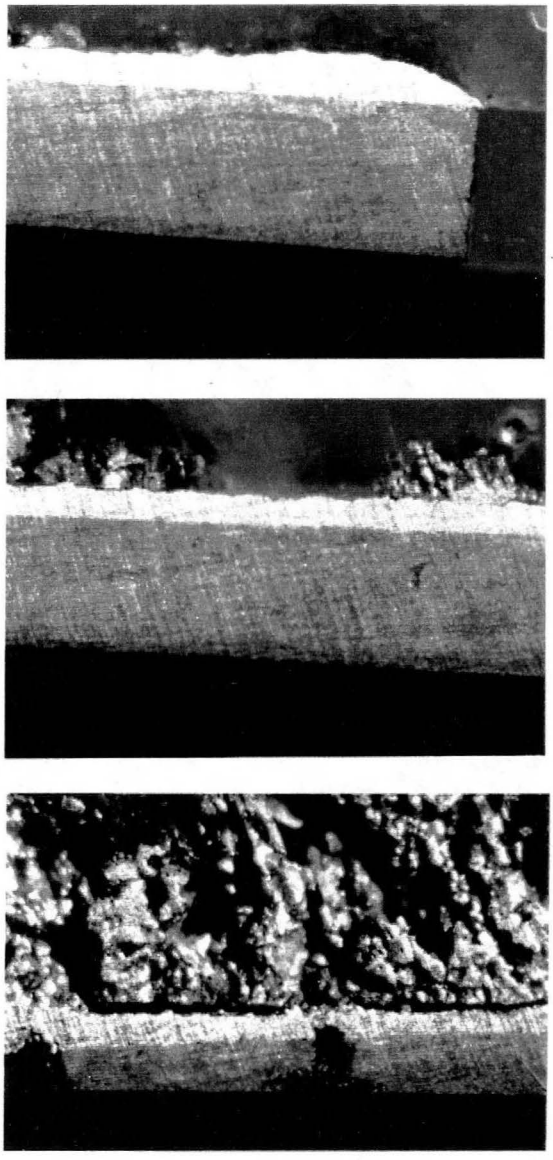

leading edge

trailing edge

copper substrate, 49 g/l zinc oxide + 6M KOH, 30 mA/cm**2,

3 hours, 45 minutes, Re=4000

BBC 860-8334

Figure 5.5

STRUCTURE OF MOSS AT HIGH MAGNIFICATION

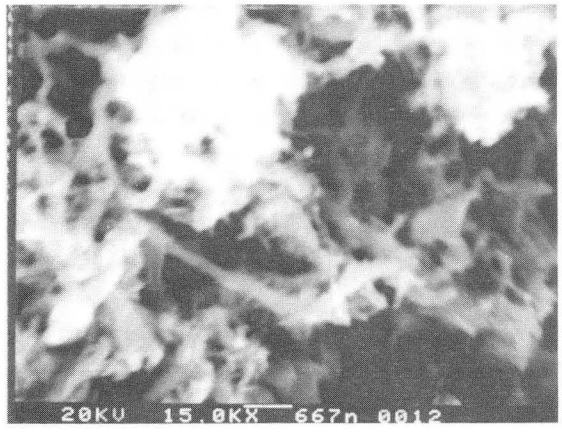

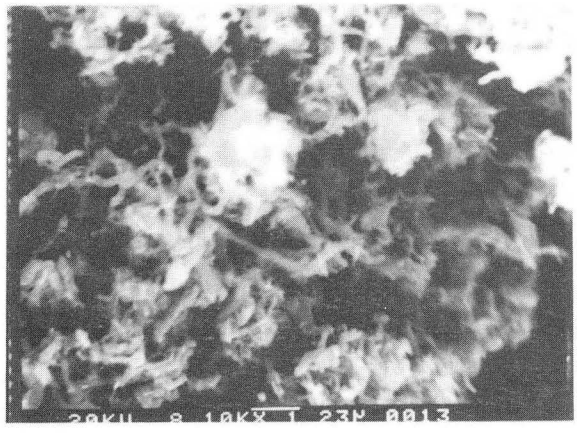

0.5 M ZnO, 6 M KOH, 20 mA/cm^2, 500 rpm, 27% i_l,
Re= 550, Ta= 1.6 X 10^6

XBB 901-383

Figure 5.6

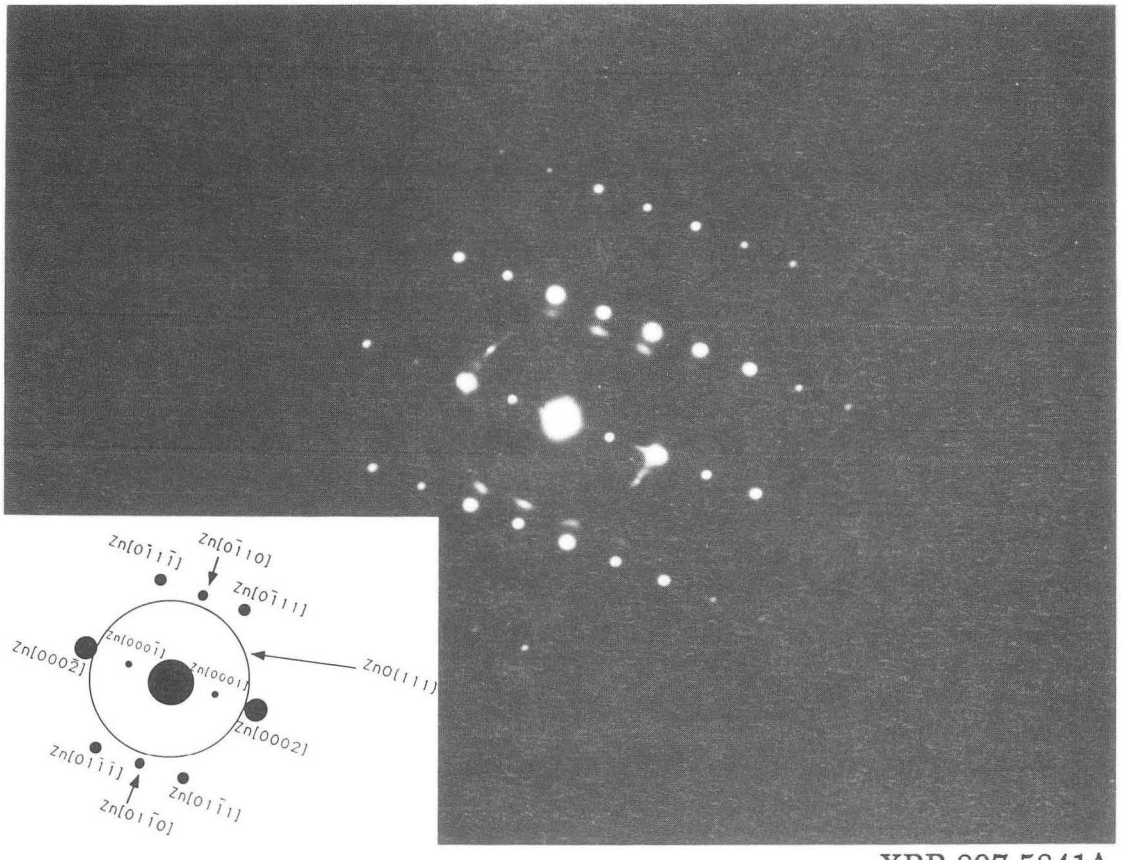

XBB 897-5841A

Figure 5.7

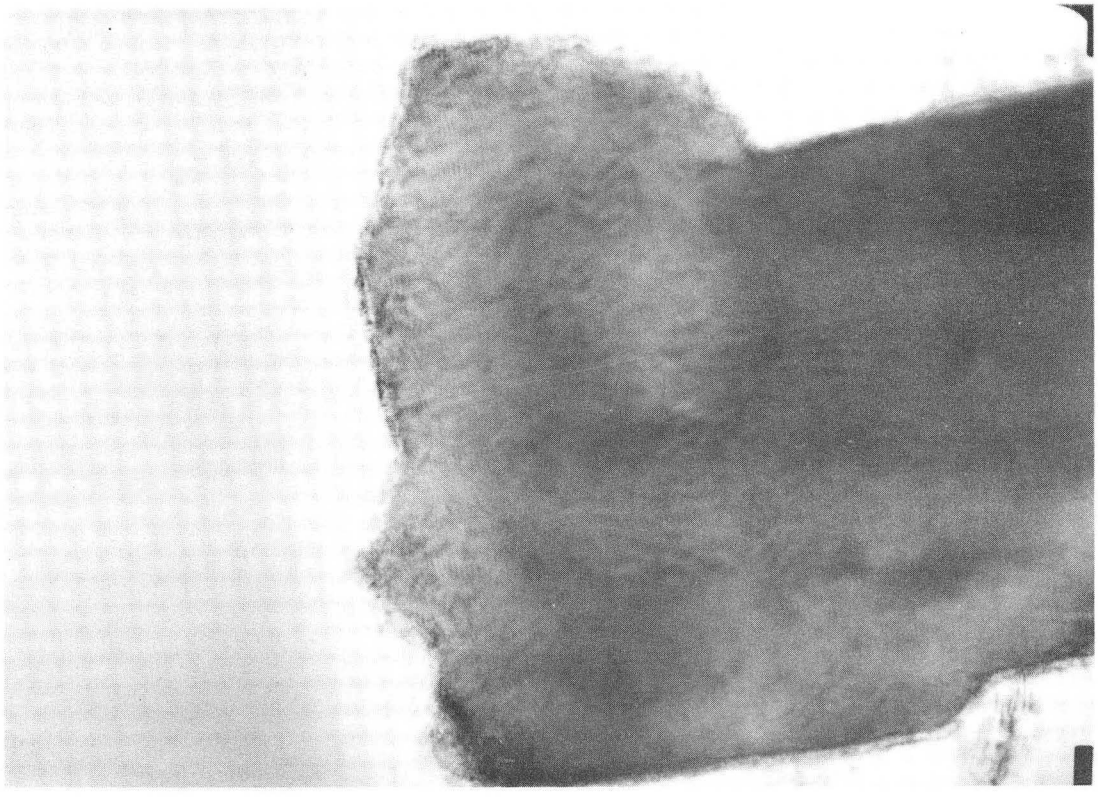

XBB 896-4722

Figure 5.8

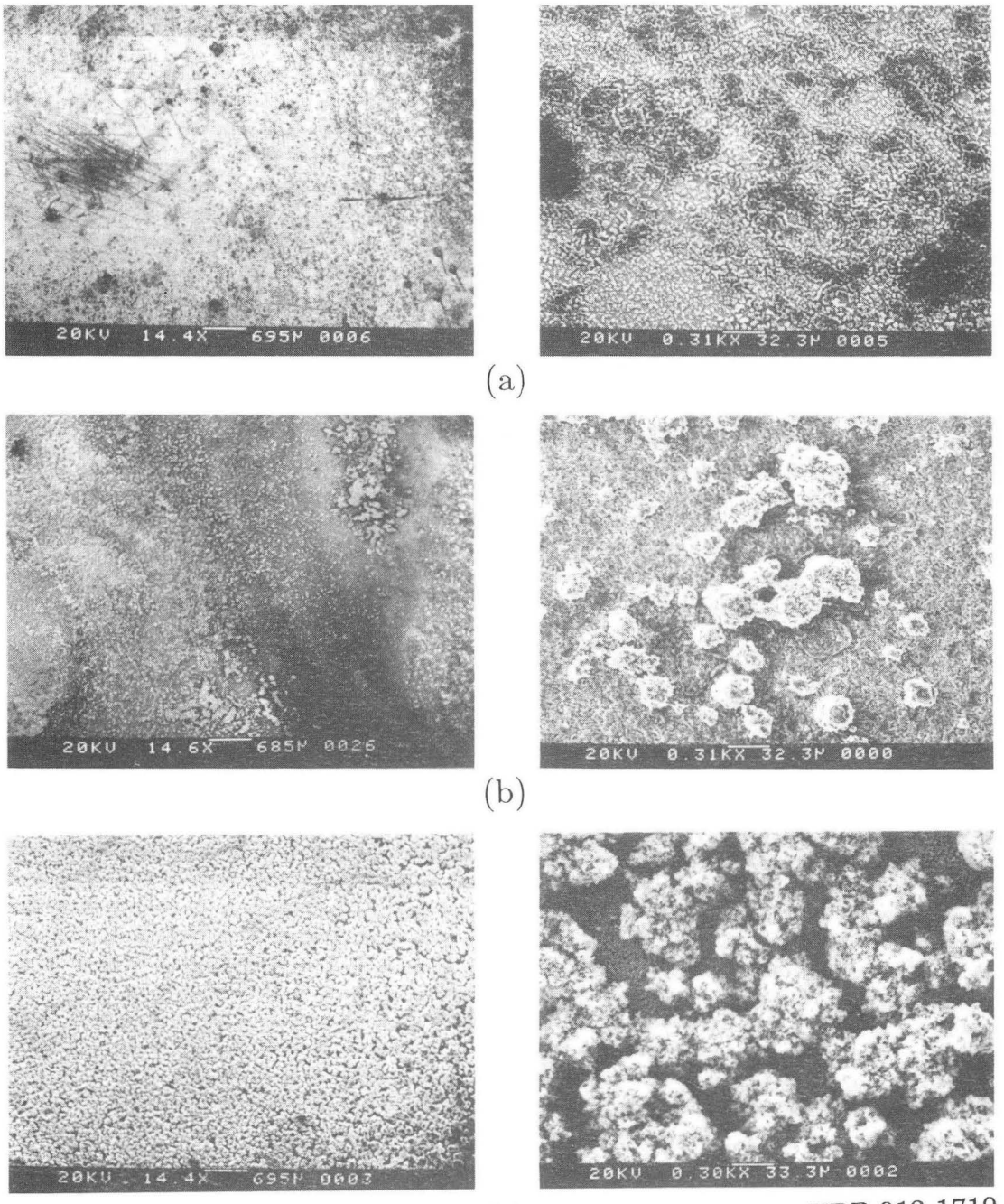
20KV 14.4X 695µ 0006
20KV 0.31KX 32.3µ 0005
(a)
20KV 14.6X 685µ 0026
20KV 0.31KX 32.3µ 0000
(b)
20KV 14.4X 695µ 0003
20KV 0.30KX 33.3µ 0002
(c)
XBB 913-1719

Figure 5.9

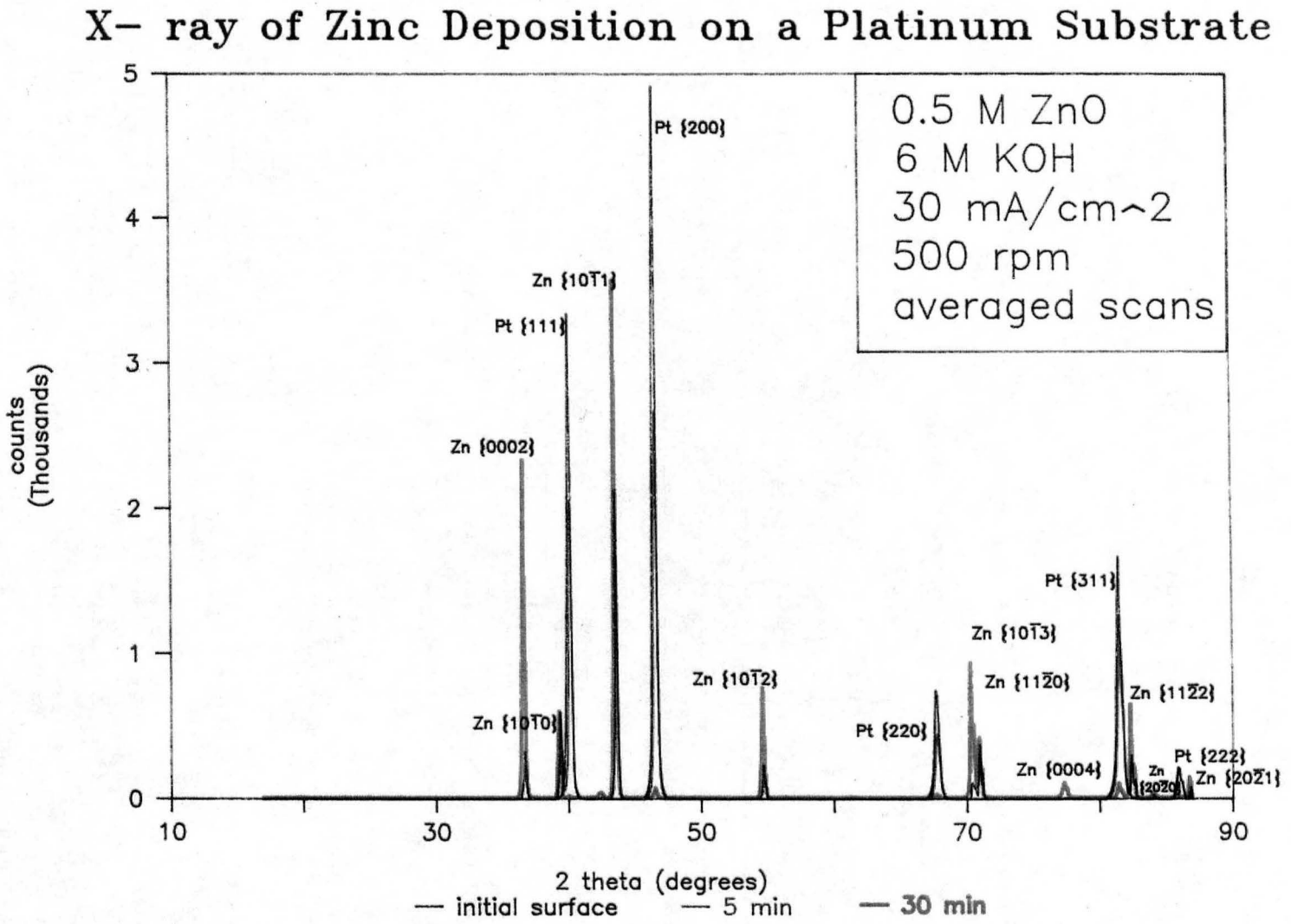

BBC 916-4588

Figure 5.10

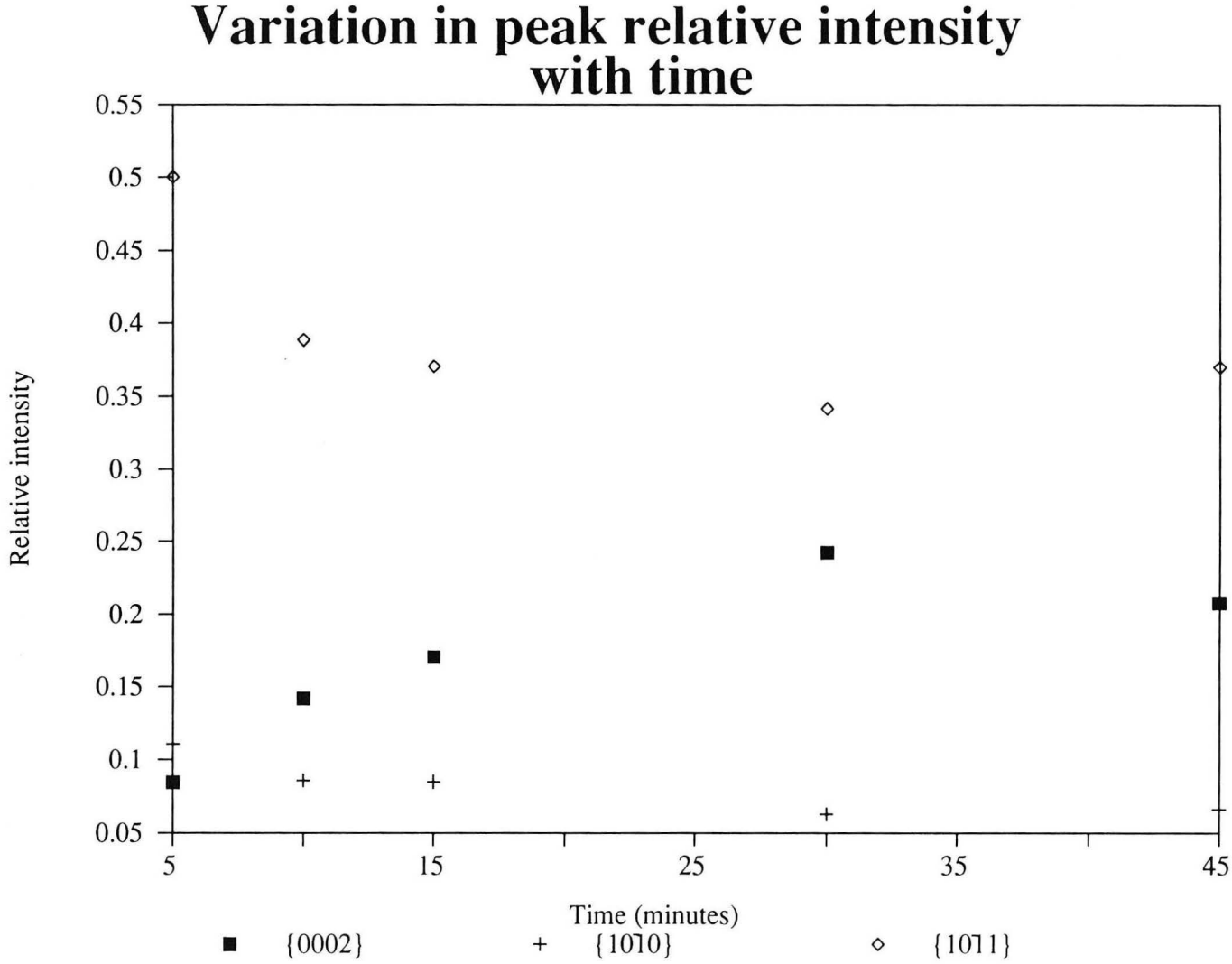

XBL 916-1266

Figure 5.11

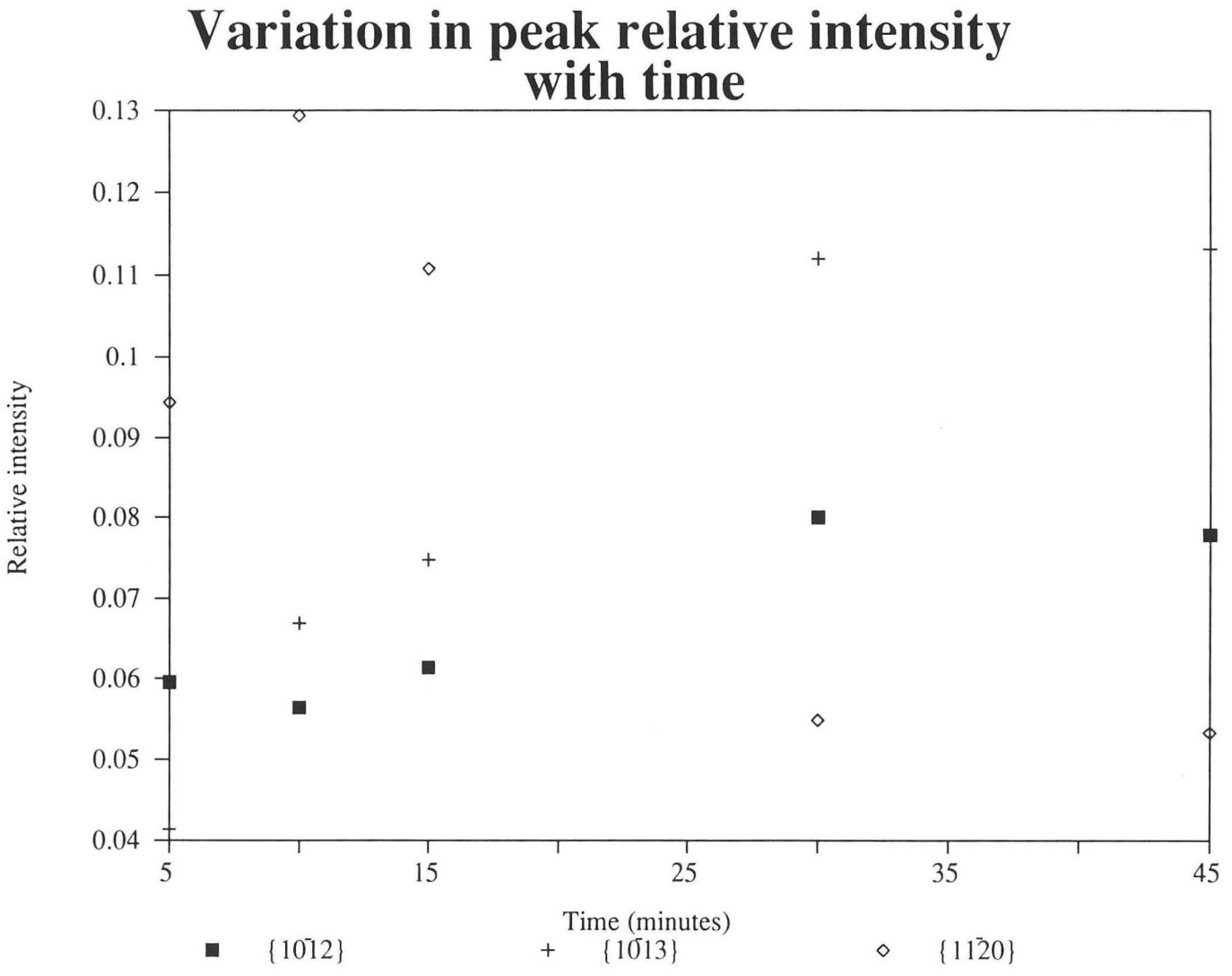

Figure 5.12

XBL 916-1265

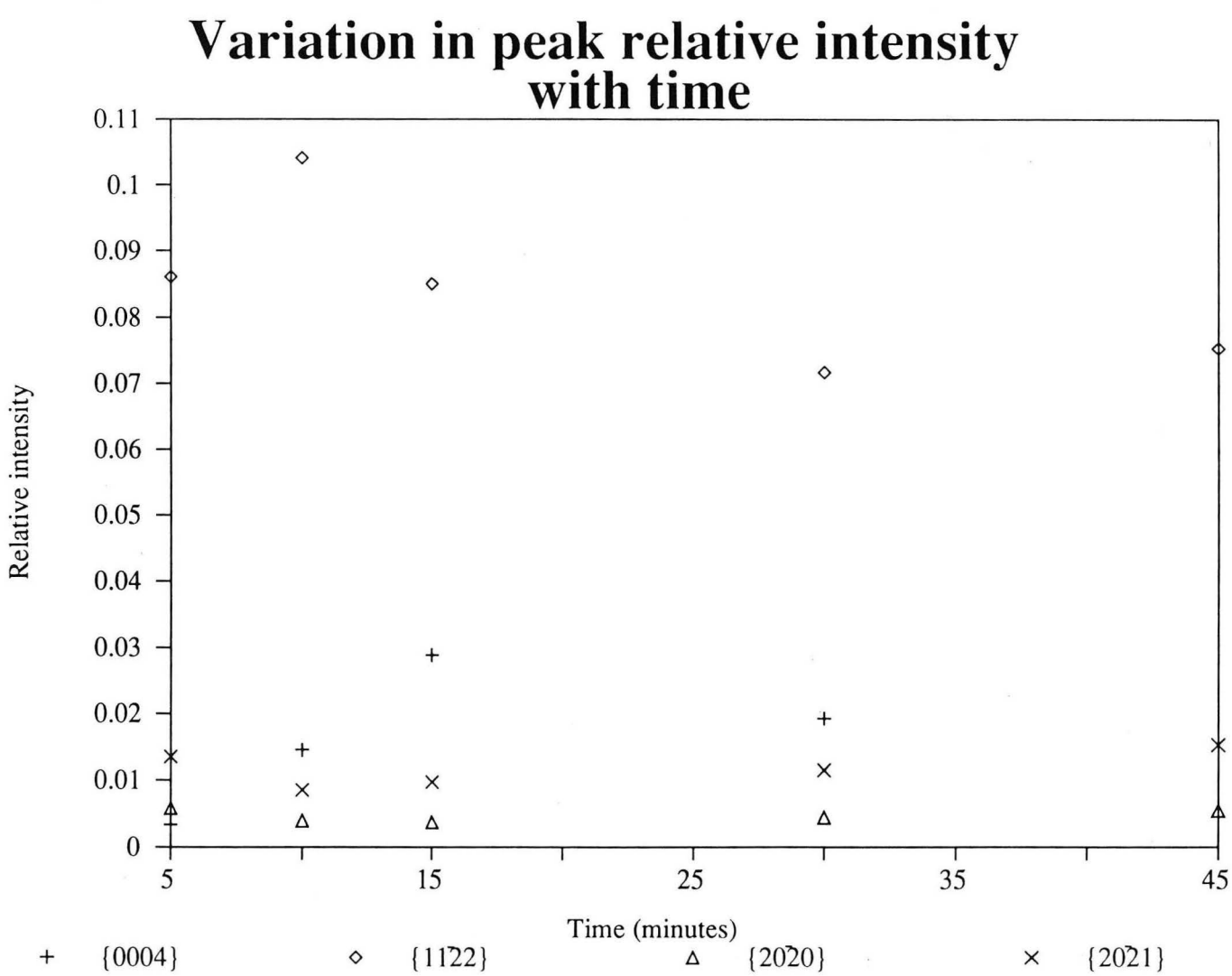

Figure 5.13

XBL 916-1264

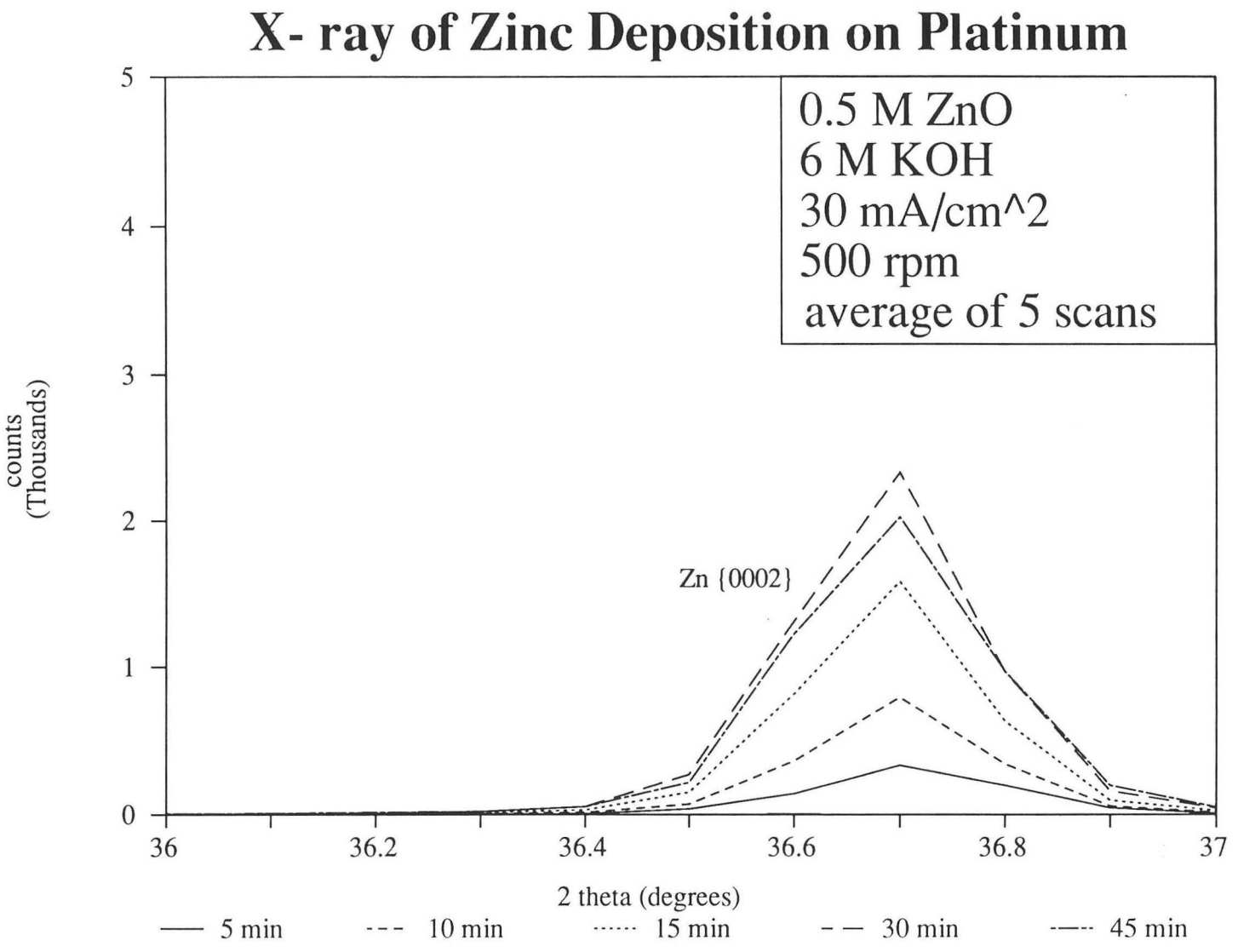

Figure 5.14

XBL 916-1267

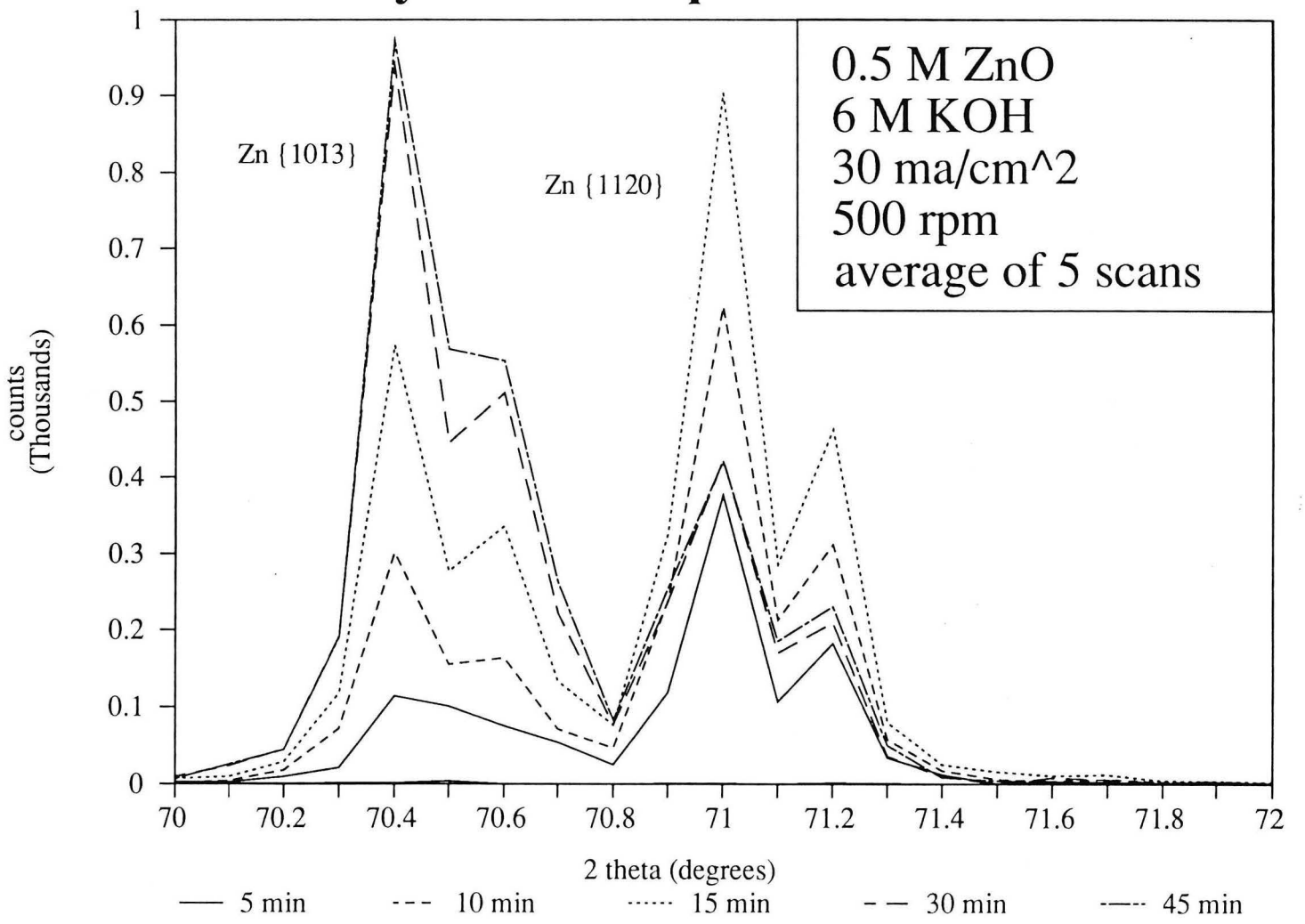

Figure 5.15

XBL 916-1268

INITIATION OF A MOSSY ZINC NODULE FROM BETWEEN TWO PROTRUSIONS

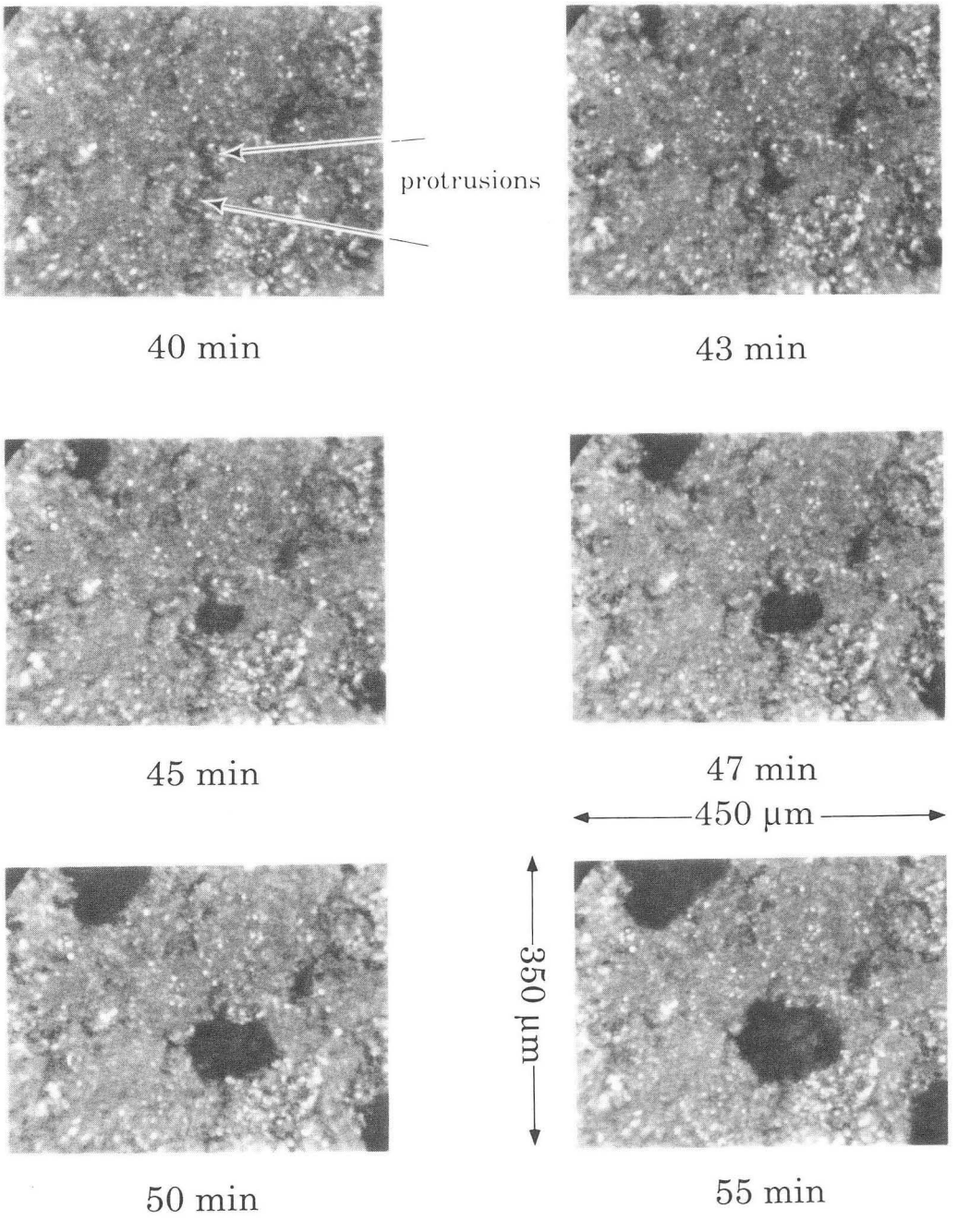

0.5 M ZnO, 12 M KOH, 10 mA/cm^2, Re= 250, V= 12 cm/s

XBB 914-3302A

Figure 5.16

INITIATION OF MOSS

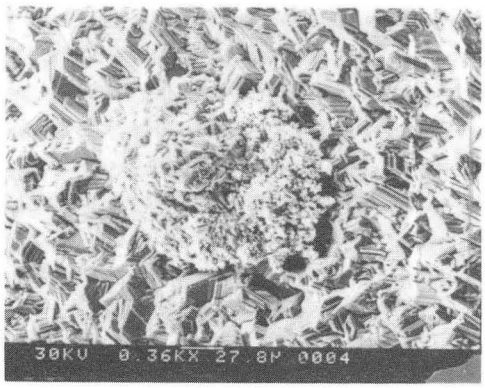

(a)

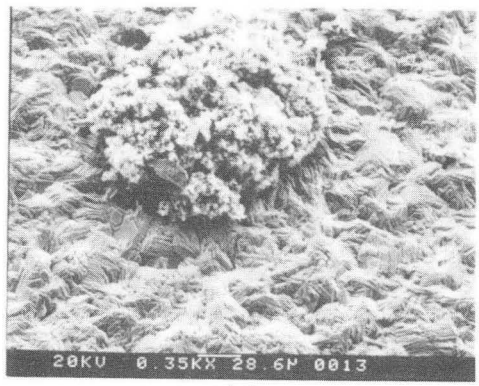

(a)

(b)

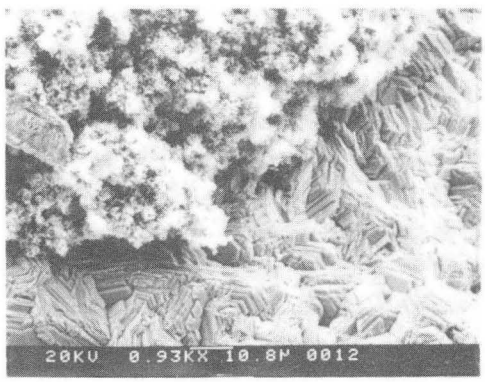

(b)

(c)
20 micron deposit

(c)
40 micron deposit

0.5 M ZnO, 6 M KOH, 1000 rpm, 50 mA/cm**2,
rotating cylinder electrode

XBB 880-10867

Figure 5.17

GROWTH OF MOSSY ZINC NODULES

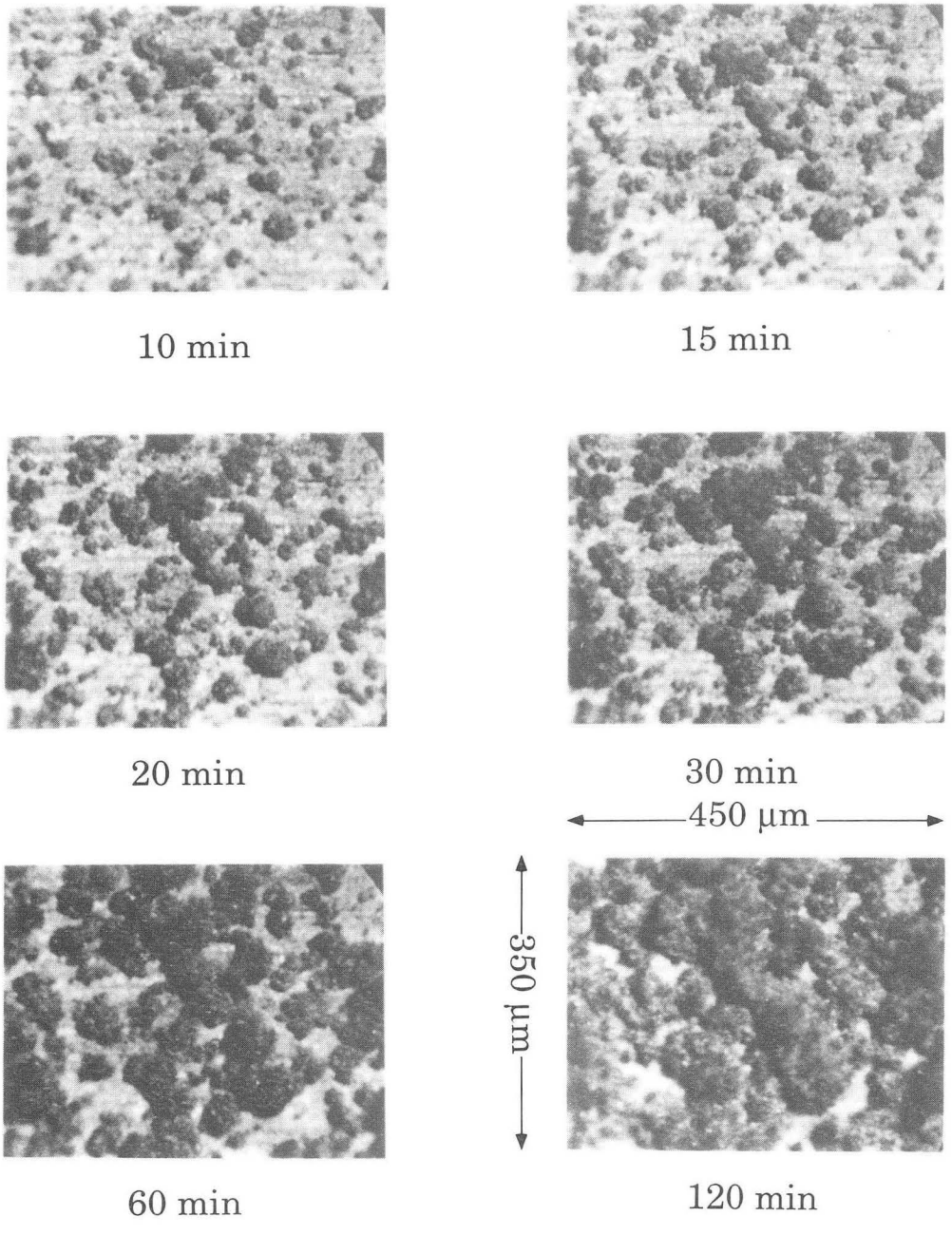

0.5 M ZnO, 6 M KOH, 2 mA/cm^2, Re= 500, V= 24 cm/s

XBB 914-3287A

Figure 5.18

GROWTH OF MOSSY ZINC NODULES

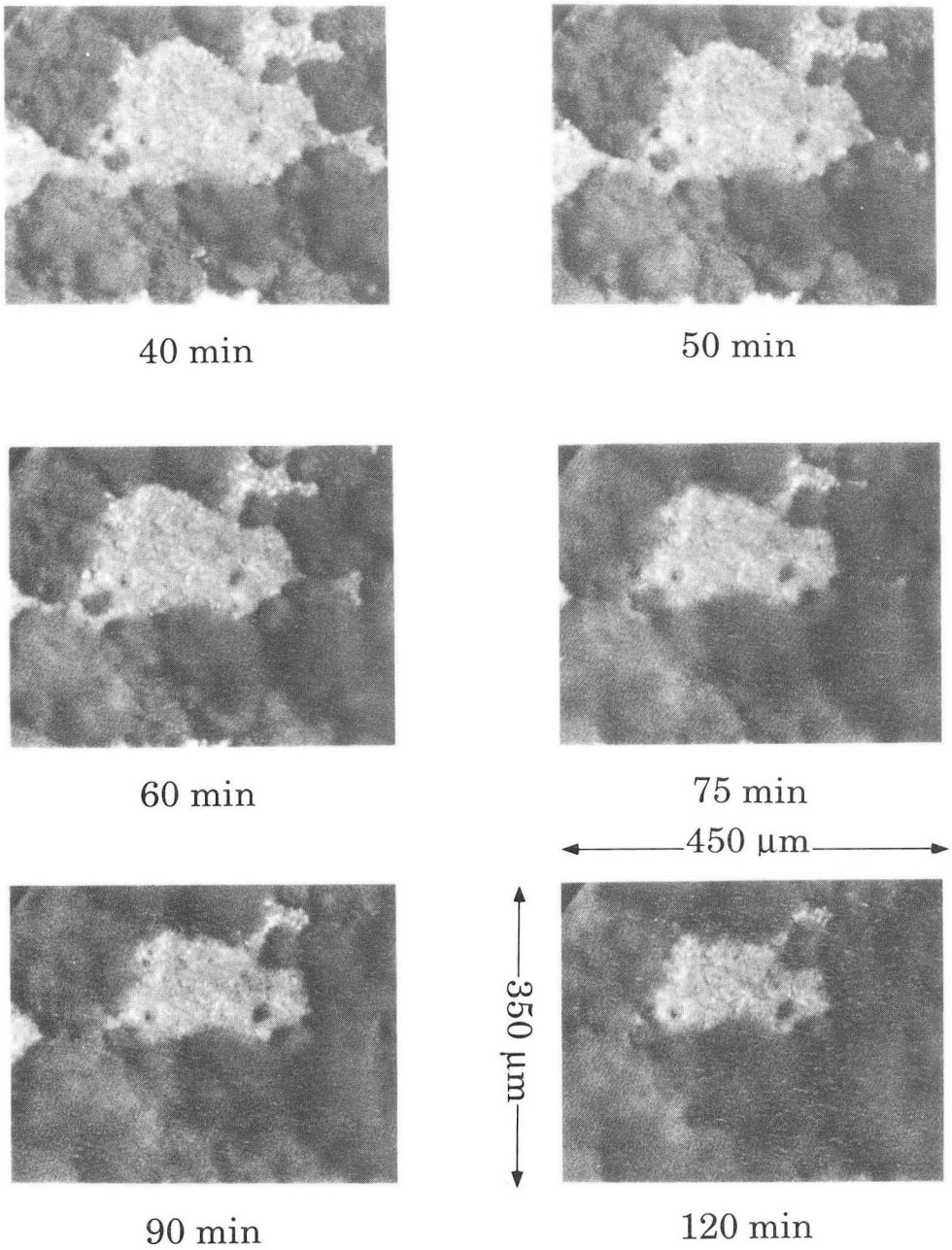

0.5 M ZnO, 12 M KOH, 10 mA/cm^2, Re= 250, V= 12 cm/s

XBB 914-3316A

Figure 5.19

PROGRESSION OF MOSS WITH INCREASING TIME

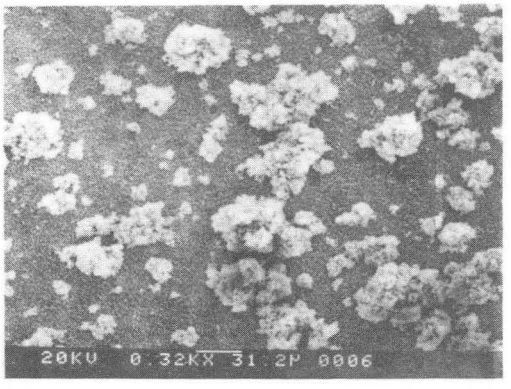

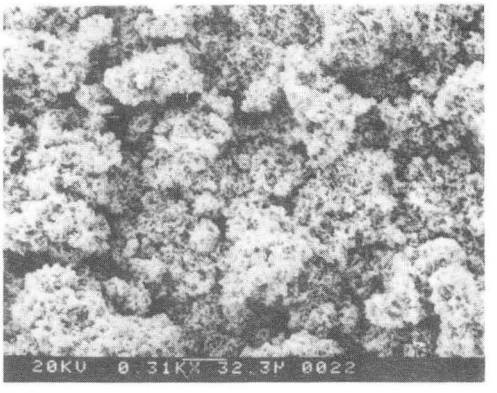

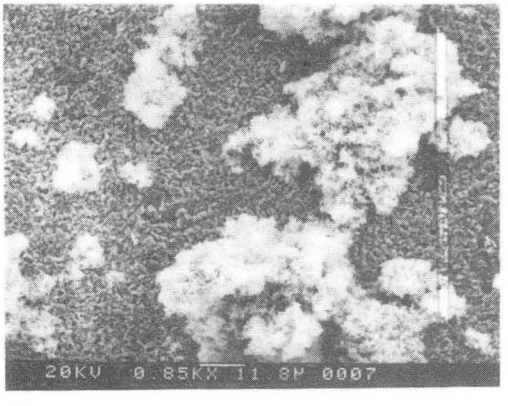

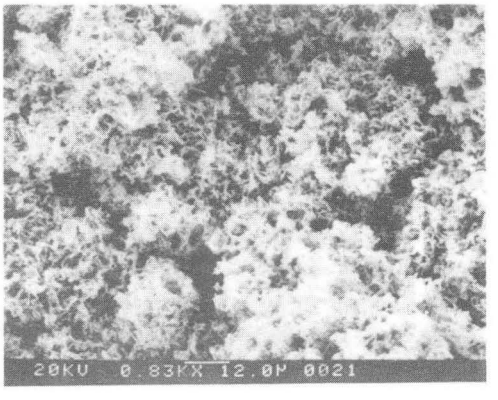

600 s

8000 s

0.25 M ZnO, 6M KOH, 15 mA/cm**2

XBB 880-10869

Figure 5.20

MOSS AT LOW CURRENT DENSITY

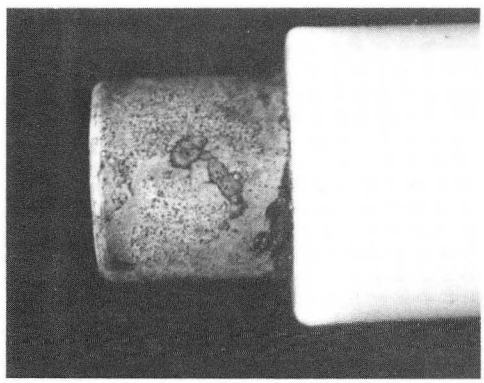

1 μm deposit thickness

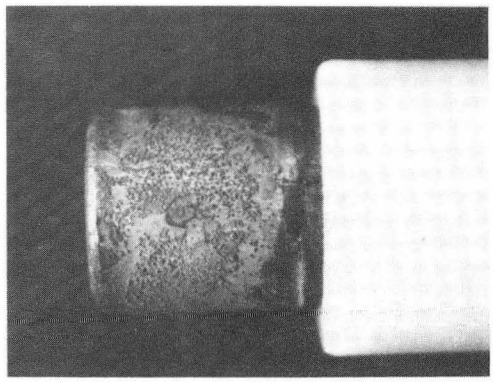

2 μm deposit thickness

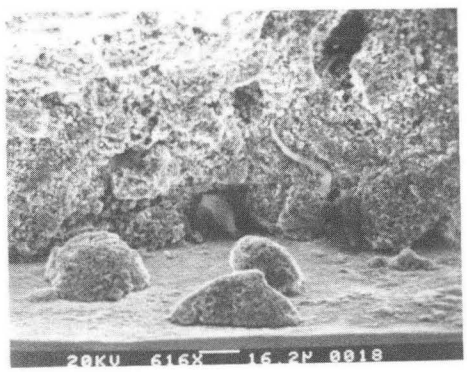

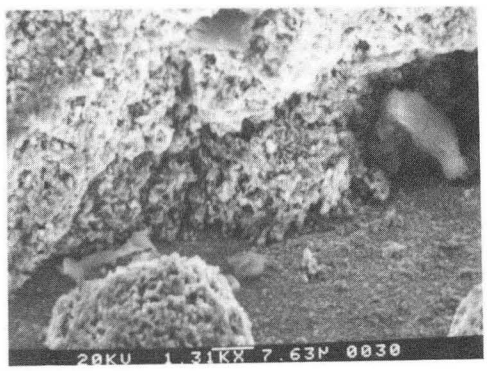

0.5 M ZnO, 6 M KOH, 2.3 mA/cm^2, 250 rpm, 5% i_l

Figure 5.21

XBB 901-380

PROGRESSION OF ROUGHNESS WITH INCREASING DEPOSIT THICKNESS

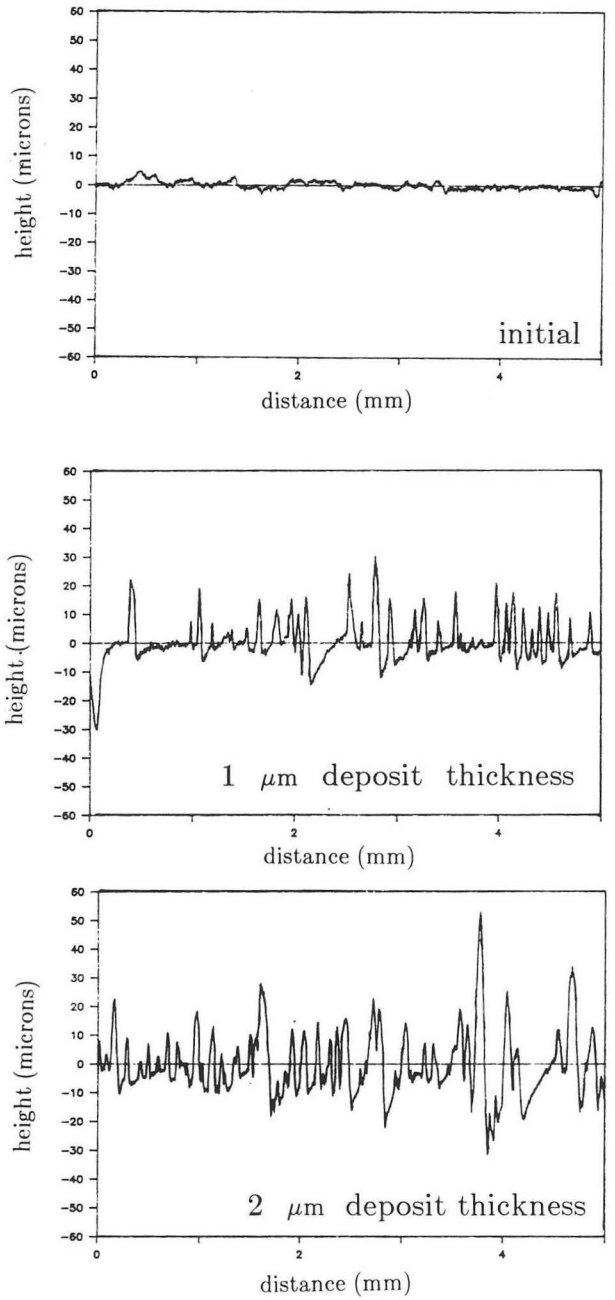

0.5 M ZnO, 6 M KOH, 2.3 mA/cm^2, 250 rpm, 5% i_l,
Re= 275, Ta= 4 X 10^5

XBL 901-181

Figure 5.22

CHANGE IN MORPHOLOGY
WITH INCREASING DEPOSIT THICKNESS

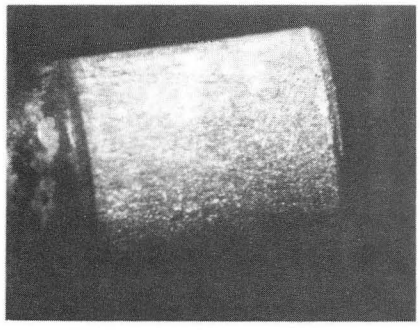

10 μm

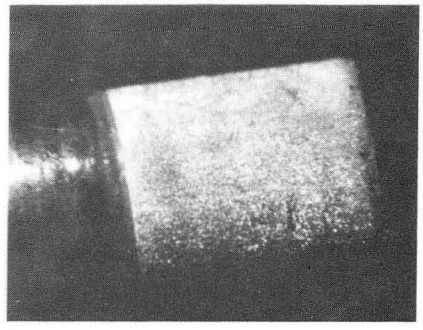

20 μm

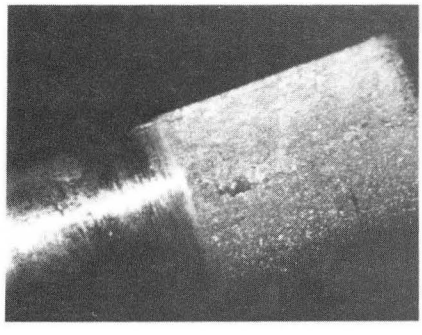

30 μm

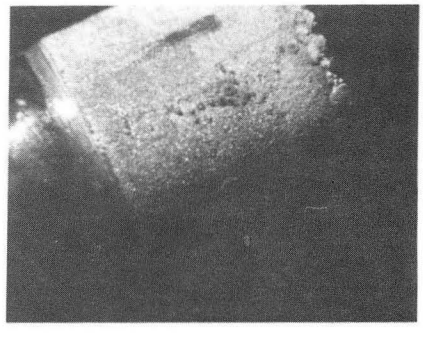

40 μm

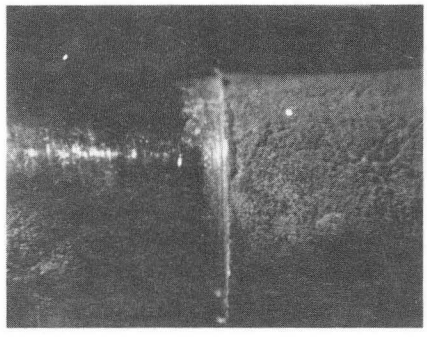

60 μm

0.5 M ZnO, 6 M KOH, 50 mA/cm^2, 500 rpm, 68% i_l

XBB 901-374

Figure 5.23

CHANGE IN PROFILE WITH INCREASING DEPOSIT THICKNESS

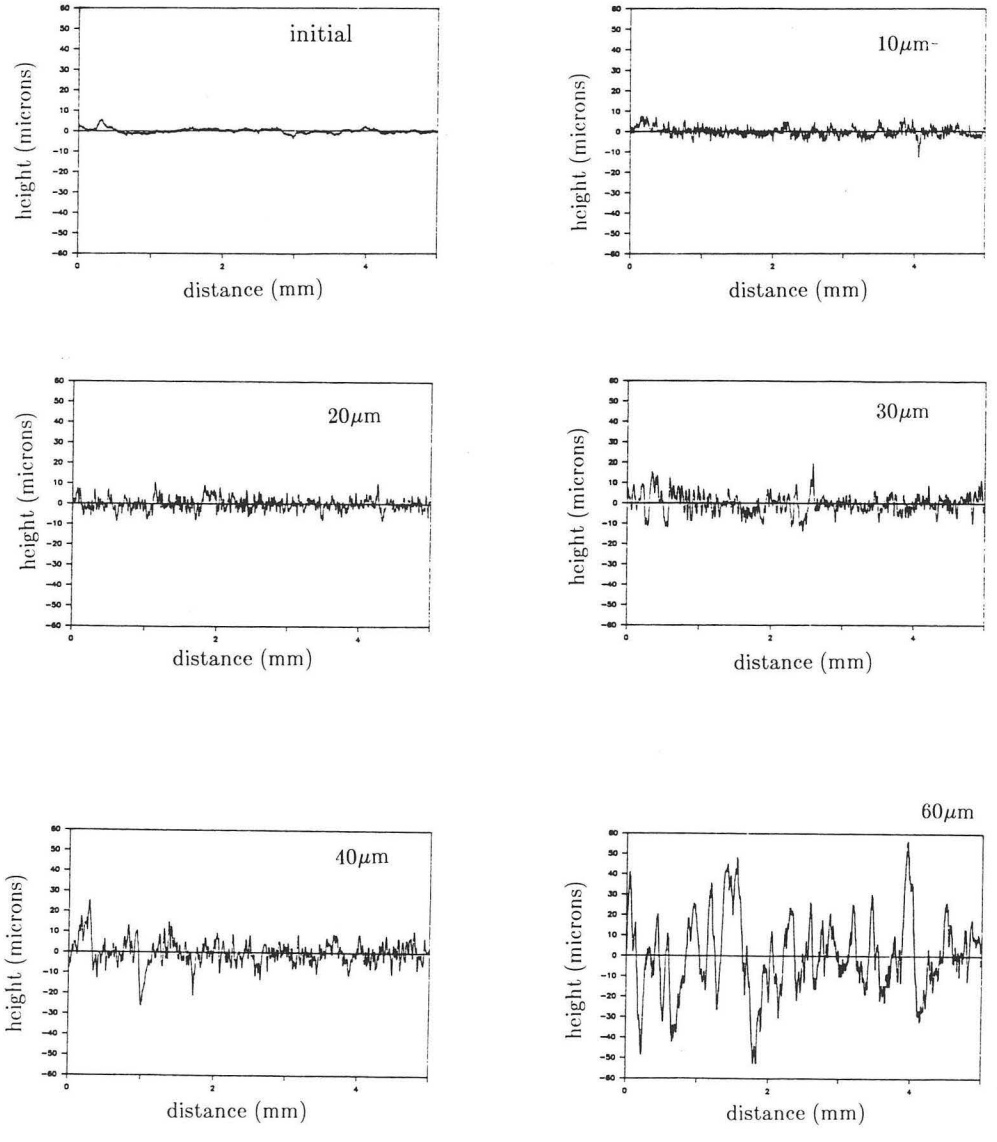

0.5 M ZnO, 6 M KOH, 500 rpm,
50 mA/cm^2, rotating cylinder electrode

XBL 901-180

Figure 5.24

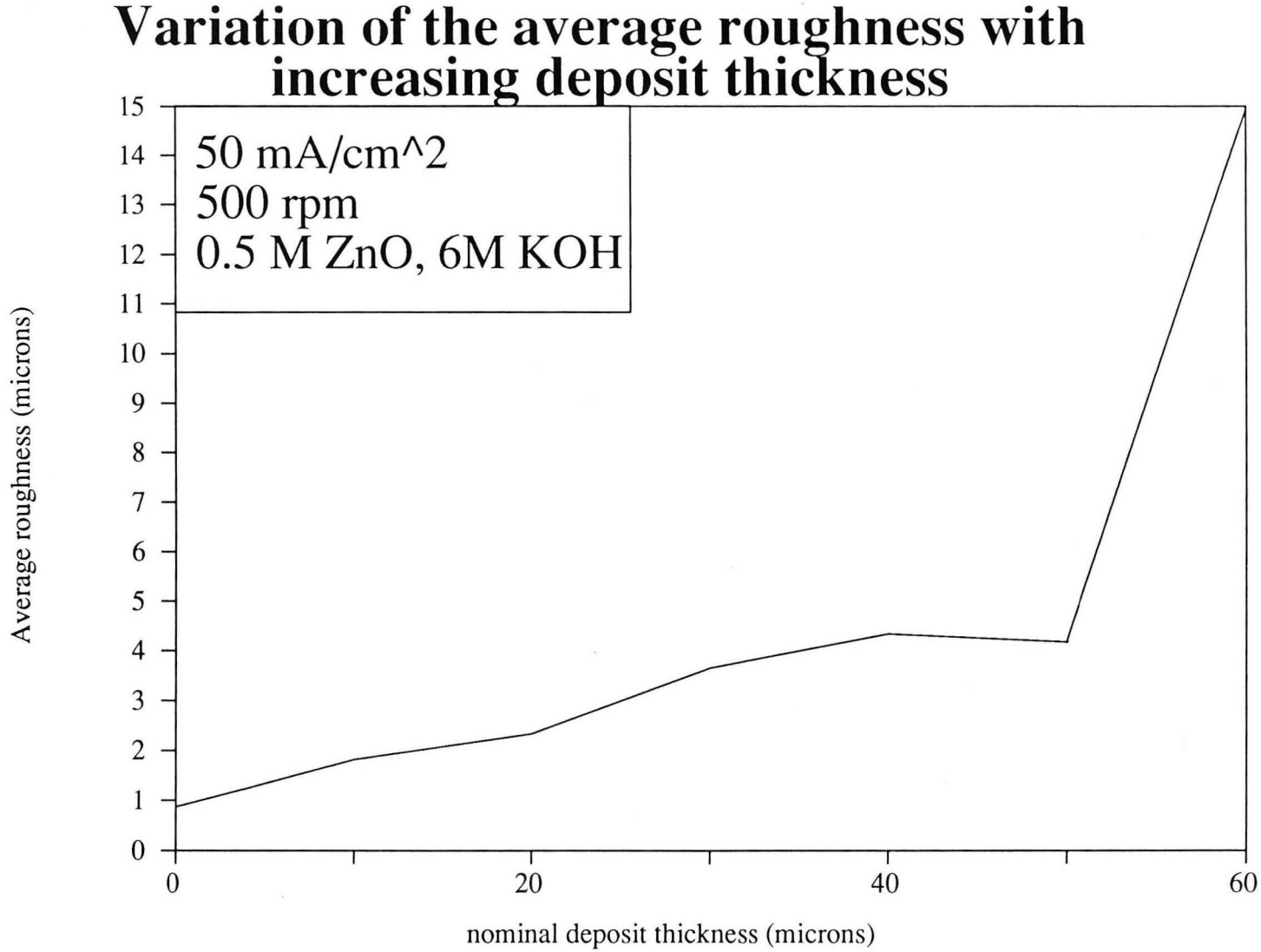

Figure 5.25

XBL 916 1249

CHANGE IN THE AUTOCORRELATION FUNCTION WITH INCREASING DEPOSIT THICKNESS

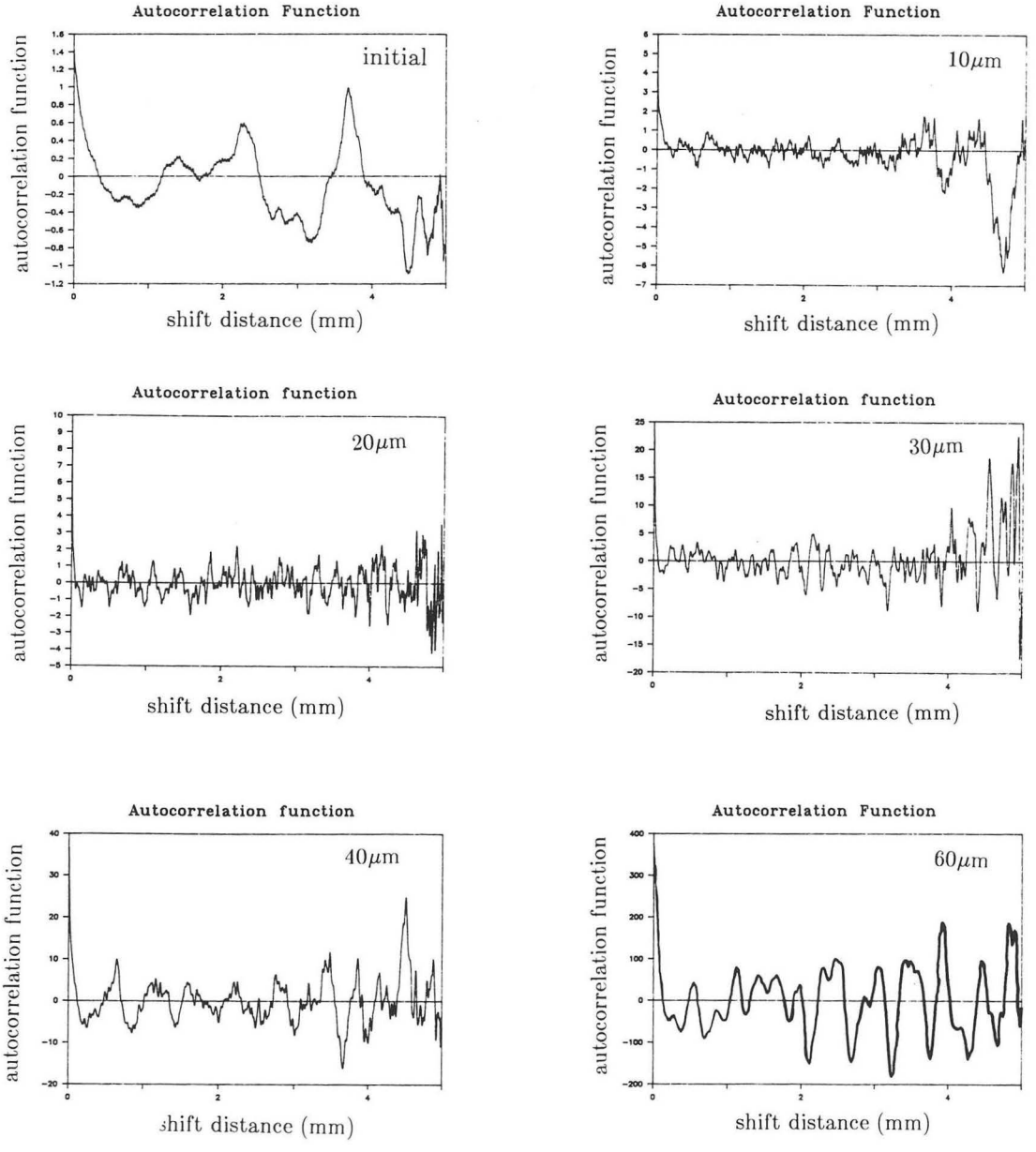

0.5 M ZnO, 6 M KOH, 500 rpm,
50 mA/cm^2, rotating cylinder electrode

XBL 901-182

Figure 5.26

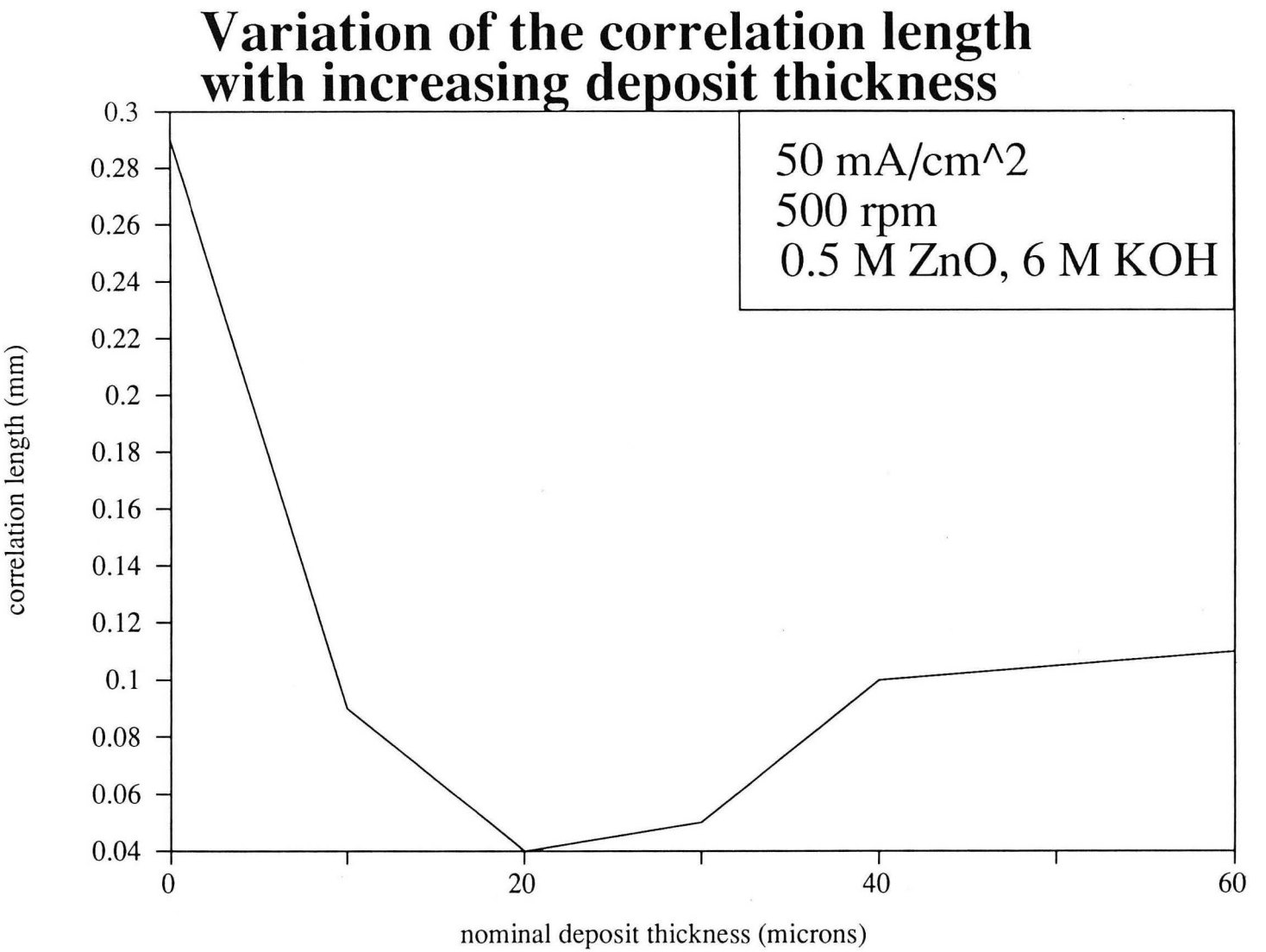

Figure 5.27

XBL 916 1250

CHANGE IN AMPLITUDE DENSITY FUNCTION WITH INCREASING DEPOSIT THICKNESS

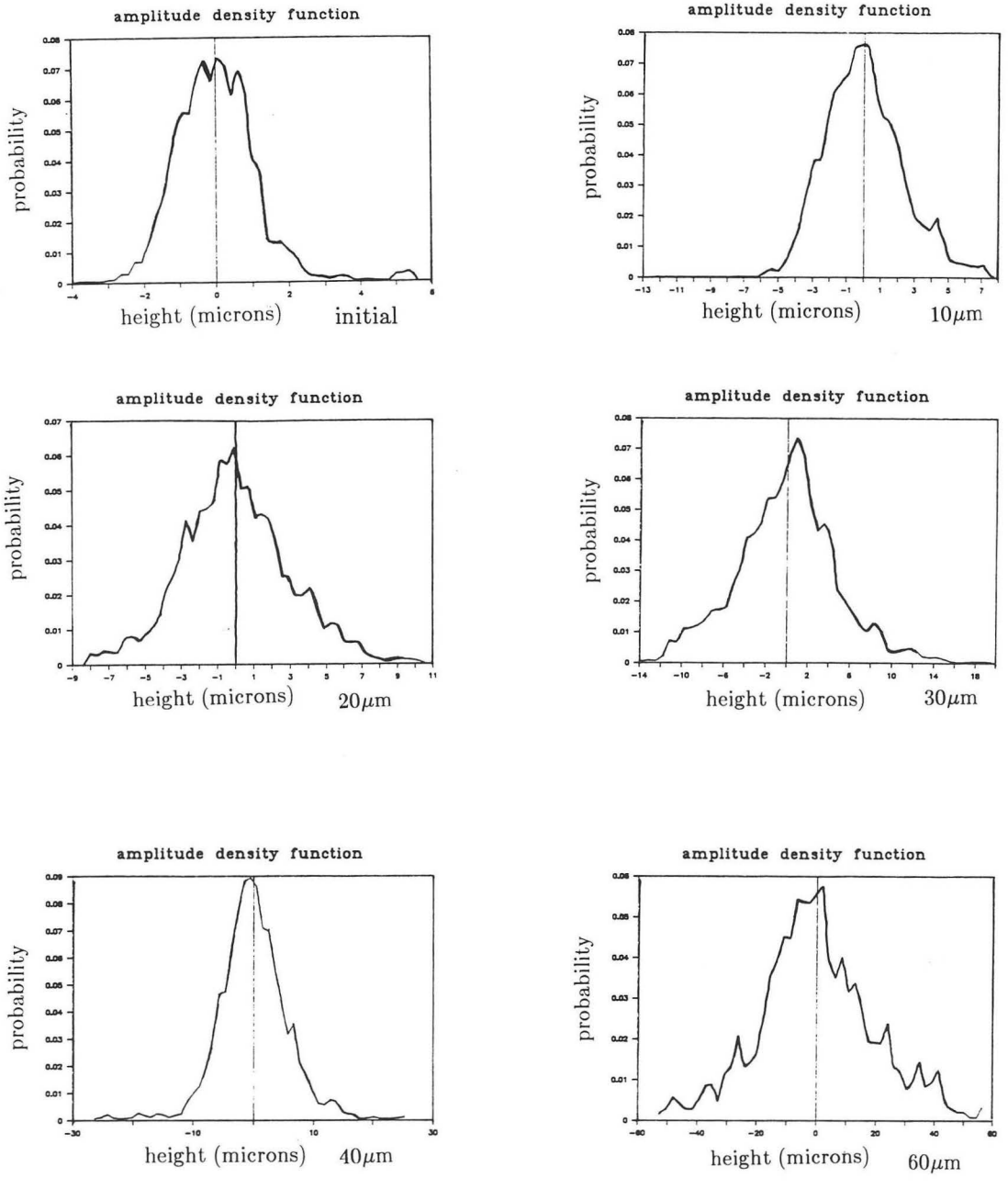

0.5 M ZnO, 6 M KOH, 500 rpm,
50 mA/cm^2, rotating cylinder electrode

XBL 901-179

Figure 5.28

COMPARISON OF THE STRUCTURE OF MOSS IN FLOWING AND NON-FLOWING MEDIA

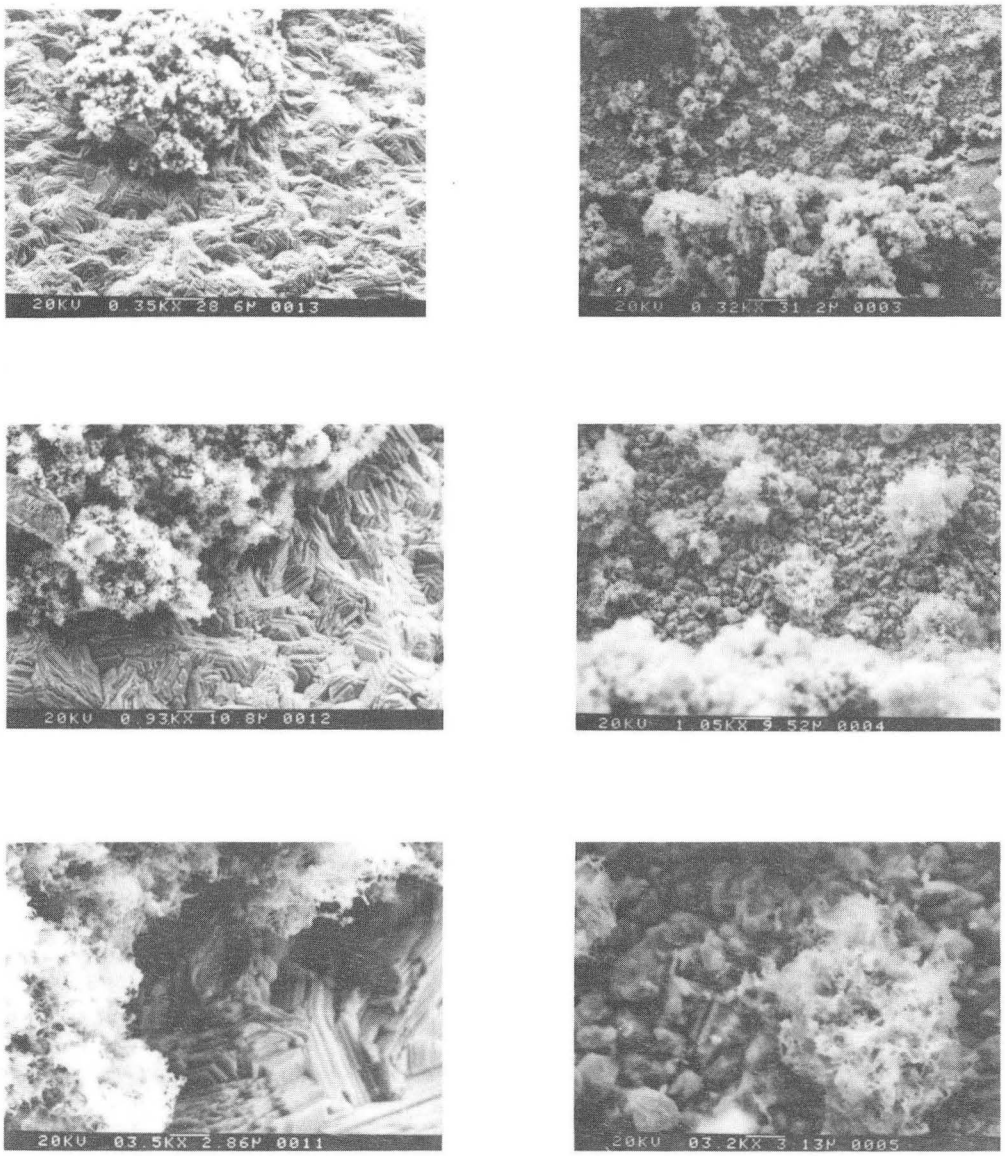

50 mA/cm^2, 40 μm deposited, 1000 rpm, Re= 1100, Ta= 6.2 X 10^6

4 mA/cm^2, 10 μm deposited, no flow

0.5 M ZnO, 6 M KOH

XBB 901-387

Figure 5.29

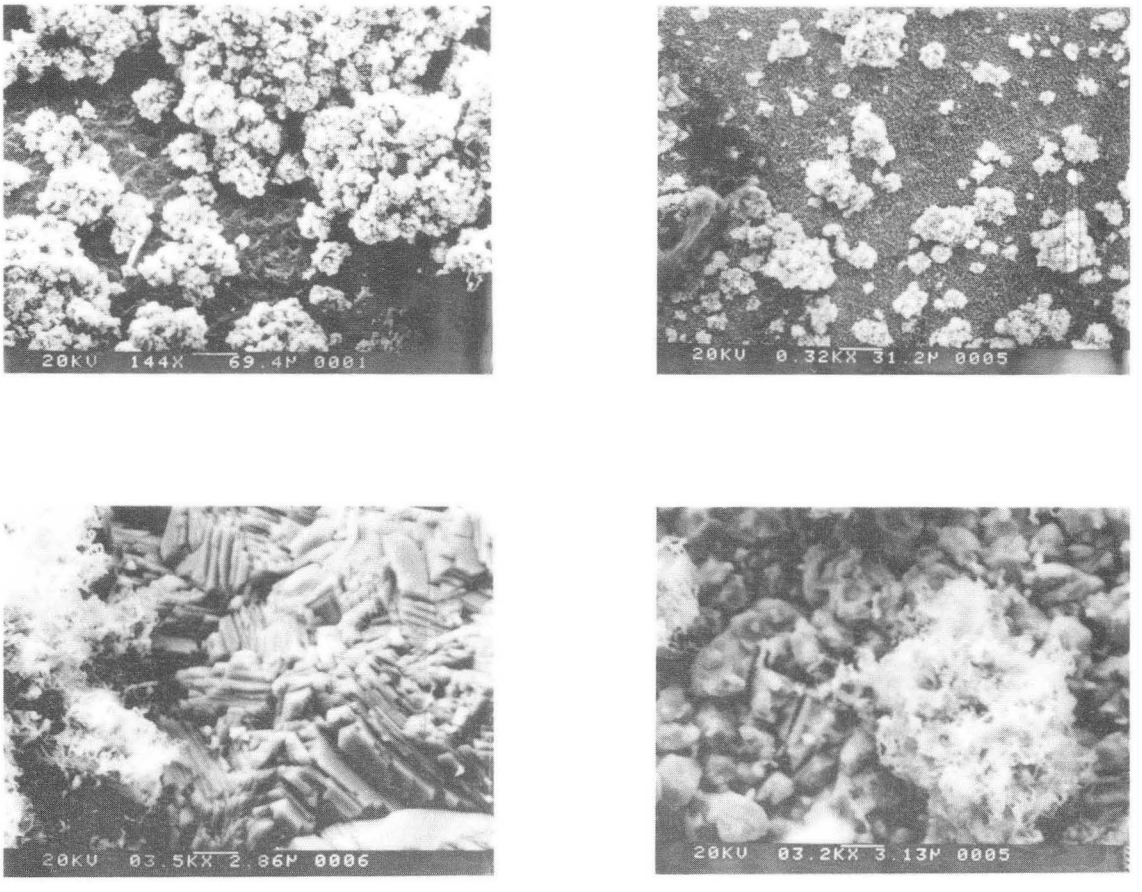

0.5 M ZnO, 6M KOH

0.25 M ZnO, 6M KOH

XBB 880-10870

Figure 5.30

COMPARISON OF THE COMPACT LAYER THICKNESSES

WHEN USING DIFFERENT SUBSTRATES

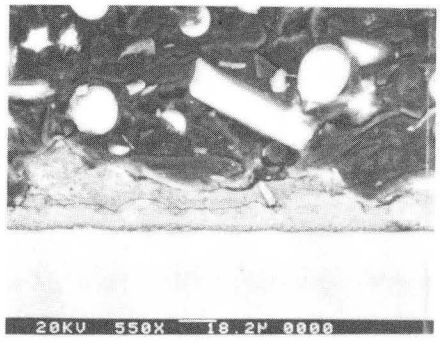

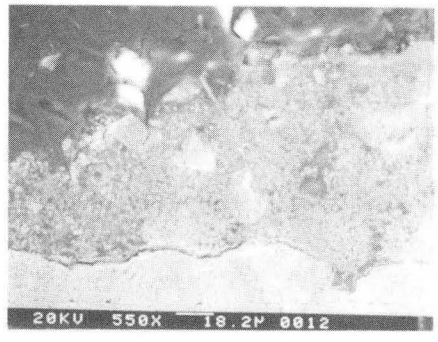

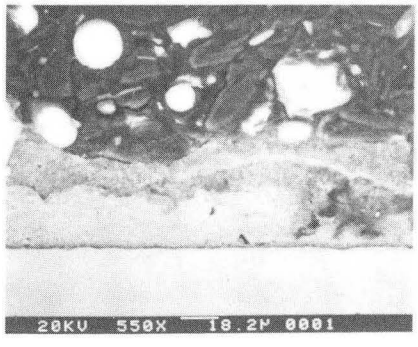

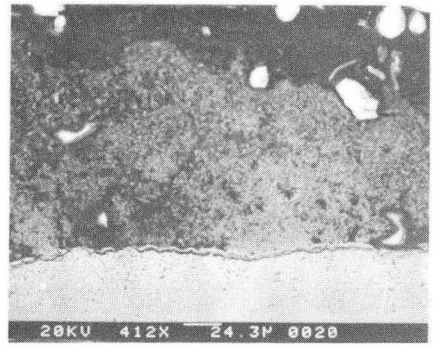

Cu, 17 μm compact layer thickness

Zn, 19 μm compact layer thickness

0.5 M ZnO, 6 M KOH, 30 mA/cm^2, 500 rpm, 41% i_l,
Re= 550, Ta= 1.6 X 10^6

XBB 901-388

Figure 5.31

COMPARISON OF THE STRUCTURE OF MOSS AT DIFFERENT

SUPPORTING ELECTROLYTE CONCENTRATIONS

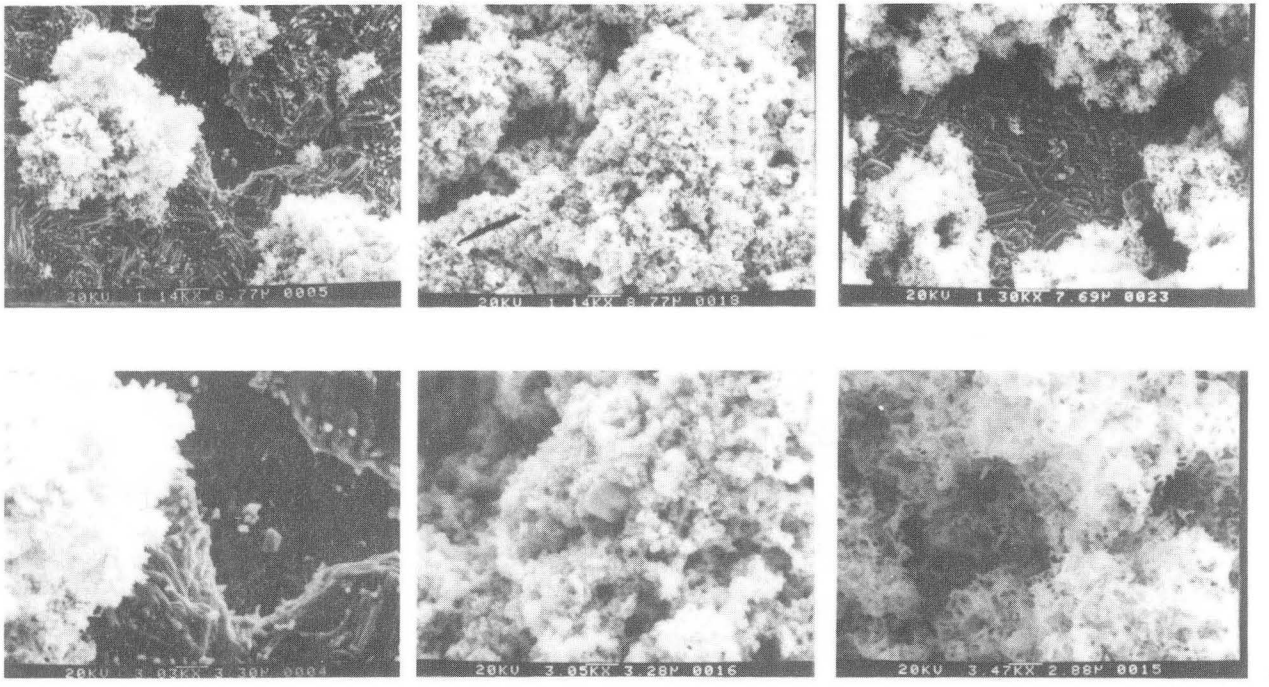

3 M 6 M 12 M

0.25 M ZnO, 15 mA/cm^2, 500 rpm, 41% i_l,
Re= 600, Ta= 1.5 X 10^6

Figure 5.32 XBB 901-381

COMPARISON OF THE COMPACT LAYER THICKNESS AT DIFFERENT SUPPORTING ELECTROLYTE CONCENTRATIONS

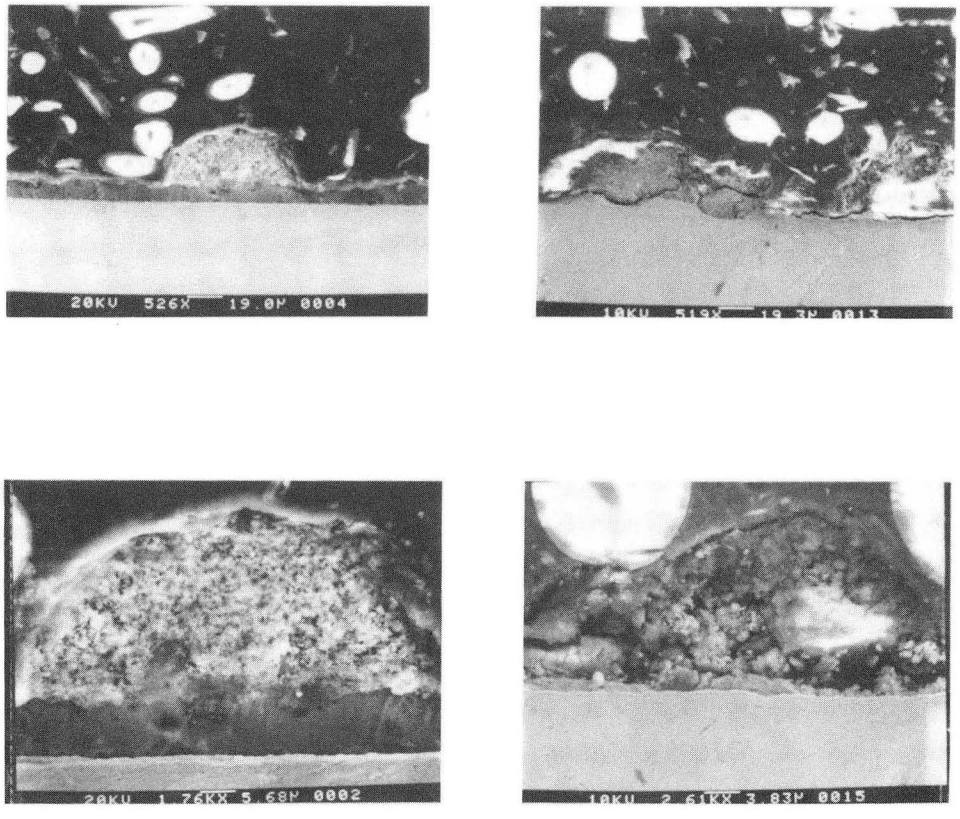

3 M KOH,
compact layer thickness= 9.95 μm

12 M KOH,
compact layer thickness= 2 μm

0.25 M ZnO, 15 mA/cm^2, 500 rpm, 41% i_l,
Re= 600, Ta= 1.5 X 10^6

XBB 901-378

Figure 5.33

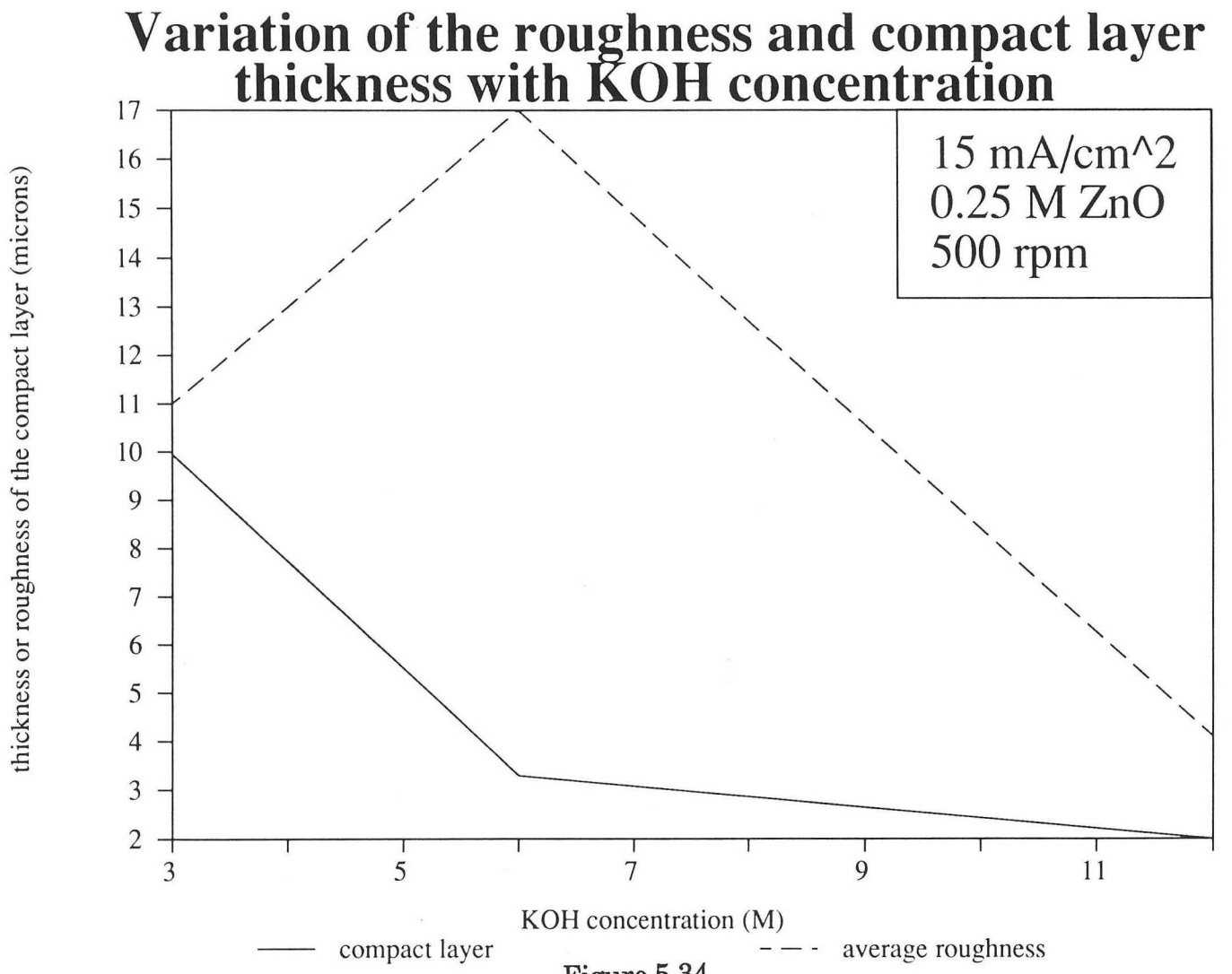

Figure 5.34

XBL 916 1251

COMPARISON OF THE COMPACT LAYER THICKNESS AT DIFFERENT FRACTIONS OF THE LIMITING CURRENT

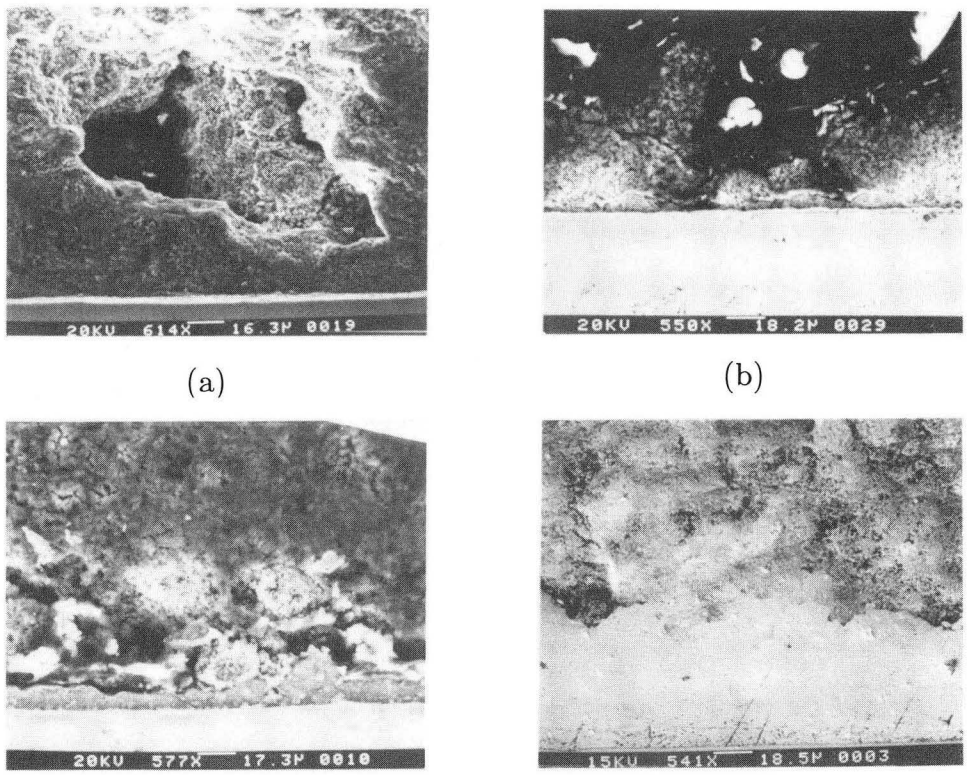

(a) (b)

(c) (d)

(a) 5 % i_l, 2.3 mA/cm^2, compact layer thickness= 1 μm

(b) 44 % i_l, 20 mA/cm^2, compact layer thickness= 4 μm

(c) 66 % i_l, 30 mA/cm^2, compact layer thickness= 15 μm

(d) 110 % i_l, 50 mA/cm^2, compact layer thickness= 77 μm

0.5 M ZnO, 6 M KOH, 250 rpm, Re= 275, Ta= 4 X 10^5

XBB 901-379

Figure 5.35

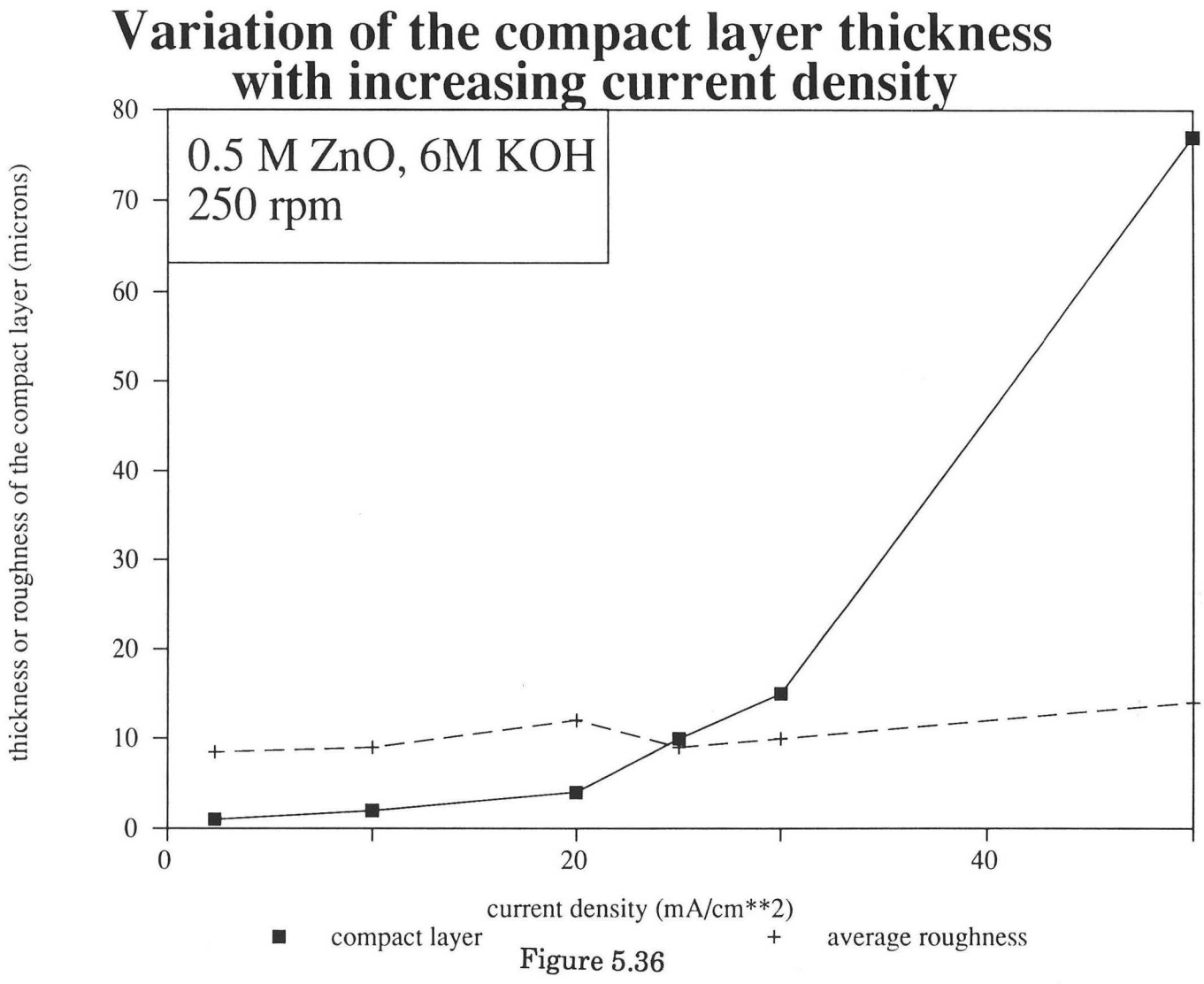

Figure 5.36

XBL 916-1252

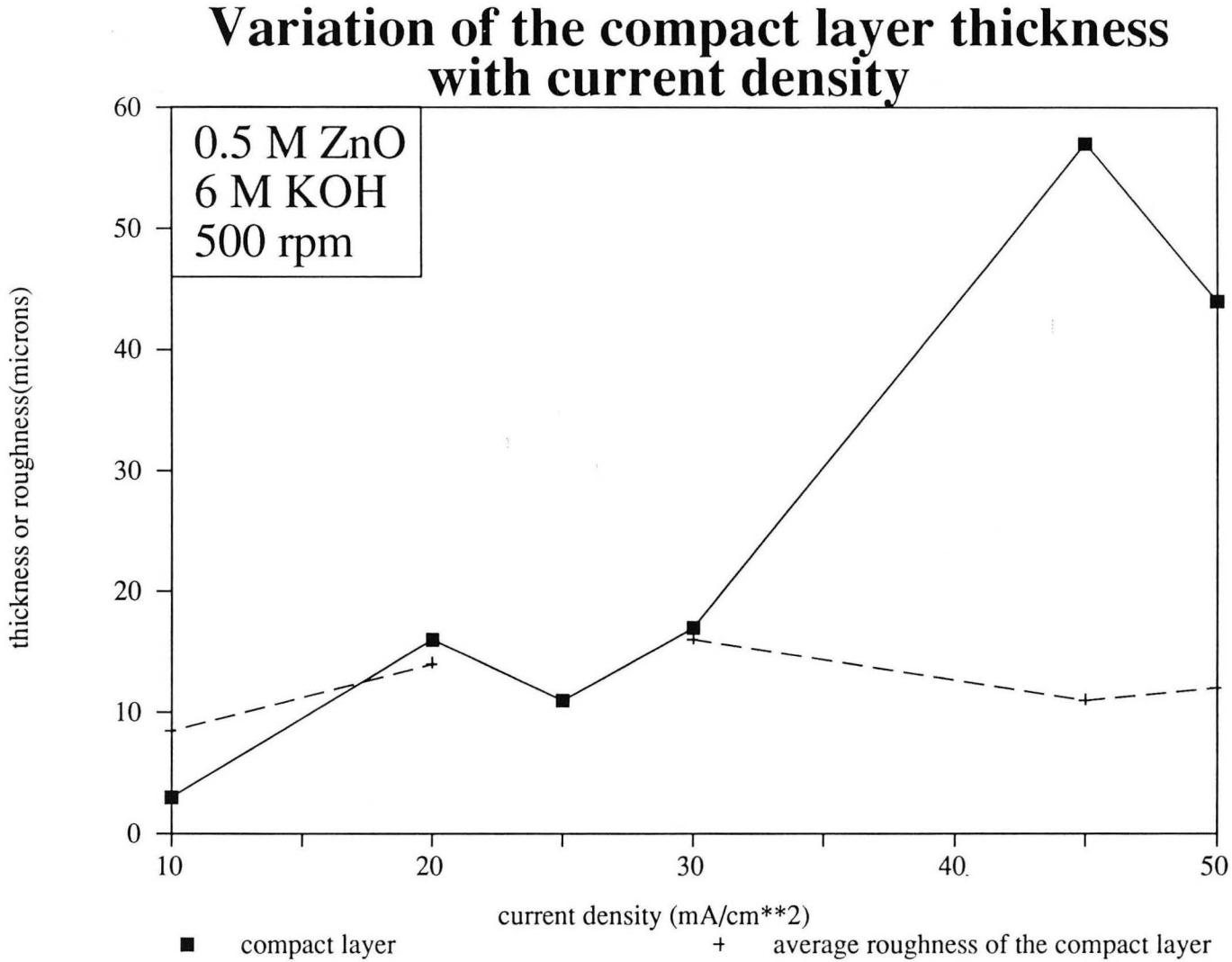

Figure 5.37

XBL 916-1253

COMPARISION OF THE COMPACT LAYER THICKNESSES WITH CHANGING CURRENT DENSITY

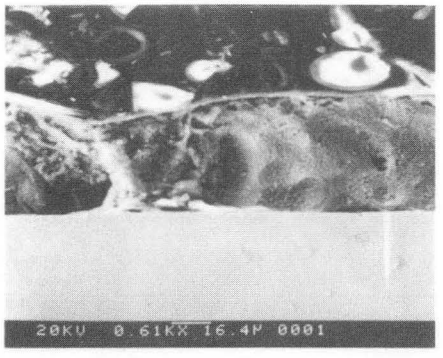

50 mA/cm^2

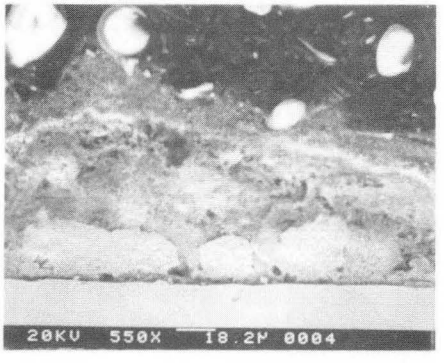

30 mA/cm^2

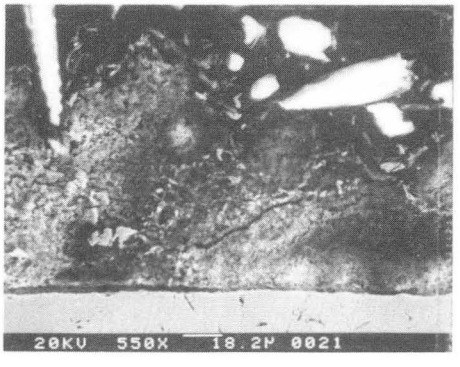

20 mA/cm^2

0.5 M ZnO, 6 M KOH, 41% i_l

XBB 901-384

Figure 5.38

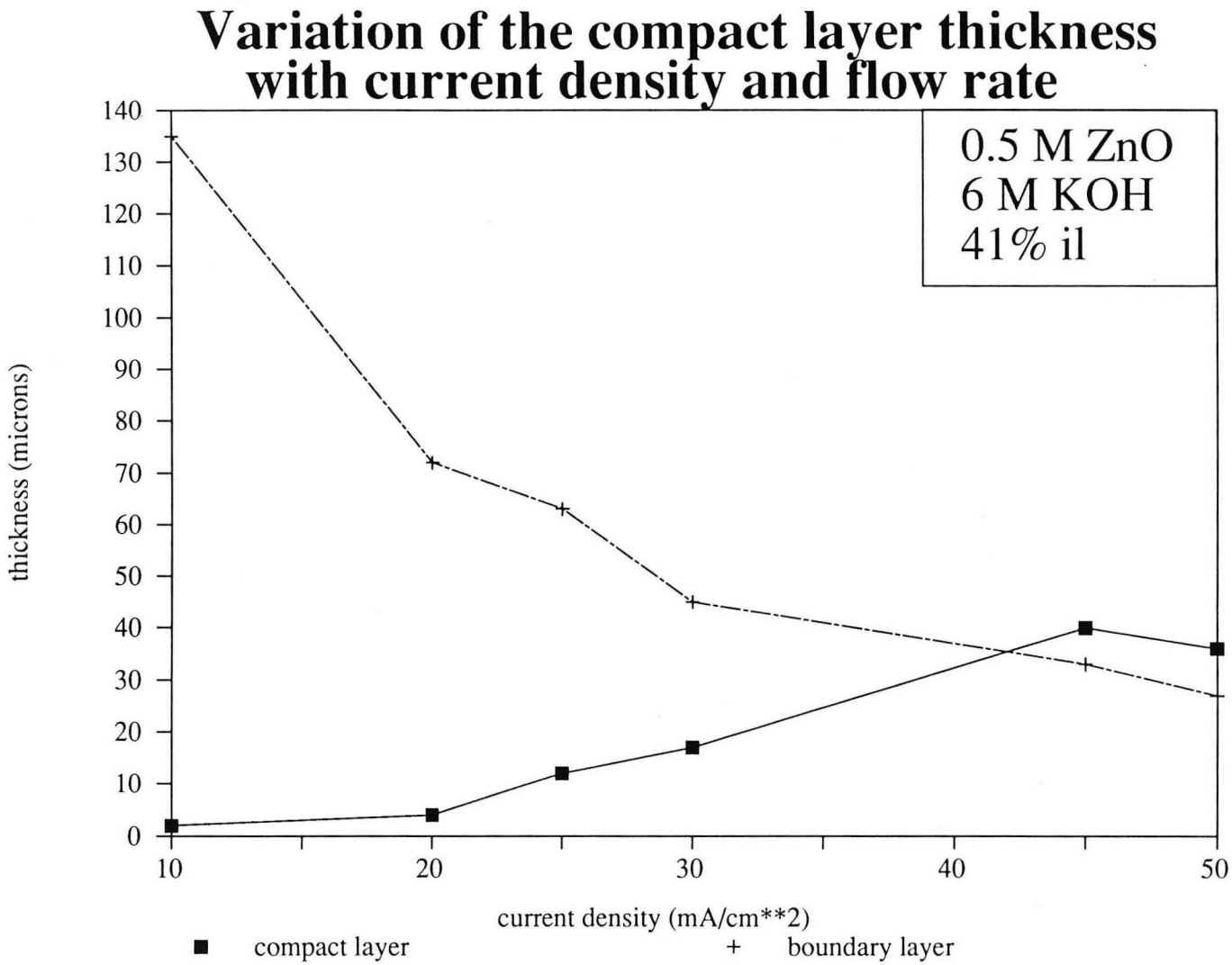

Figure 5.39

XBL 916-1254

COMPARISION OF THE COMPACT LAYER THICKNESSES WITH CHANGING CURRENT DENSITY

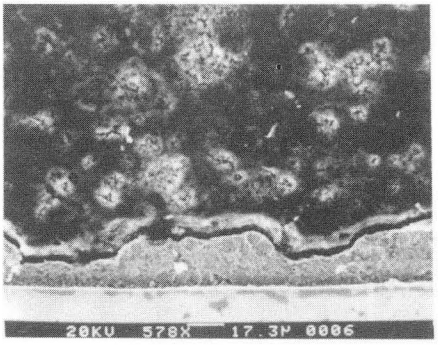

30 mA/cm^2, 250 rpm,
Re= 275, Ta= 4 X 10^5

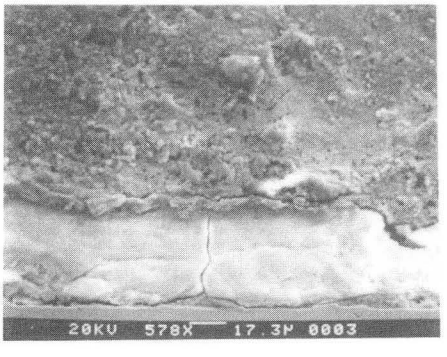

50 mA/cm^2, 500 rpm,
Re= 550, Ta= 1.6 X 10^6

0.5 M ZnO, 6 M KOH, 66% i_l

XBB 901-386

Figure 5.40

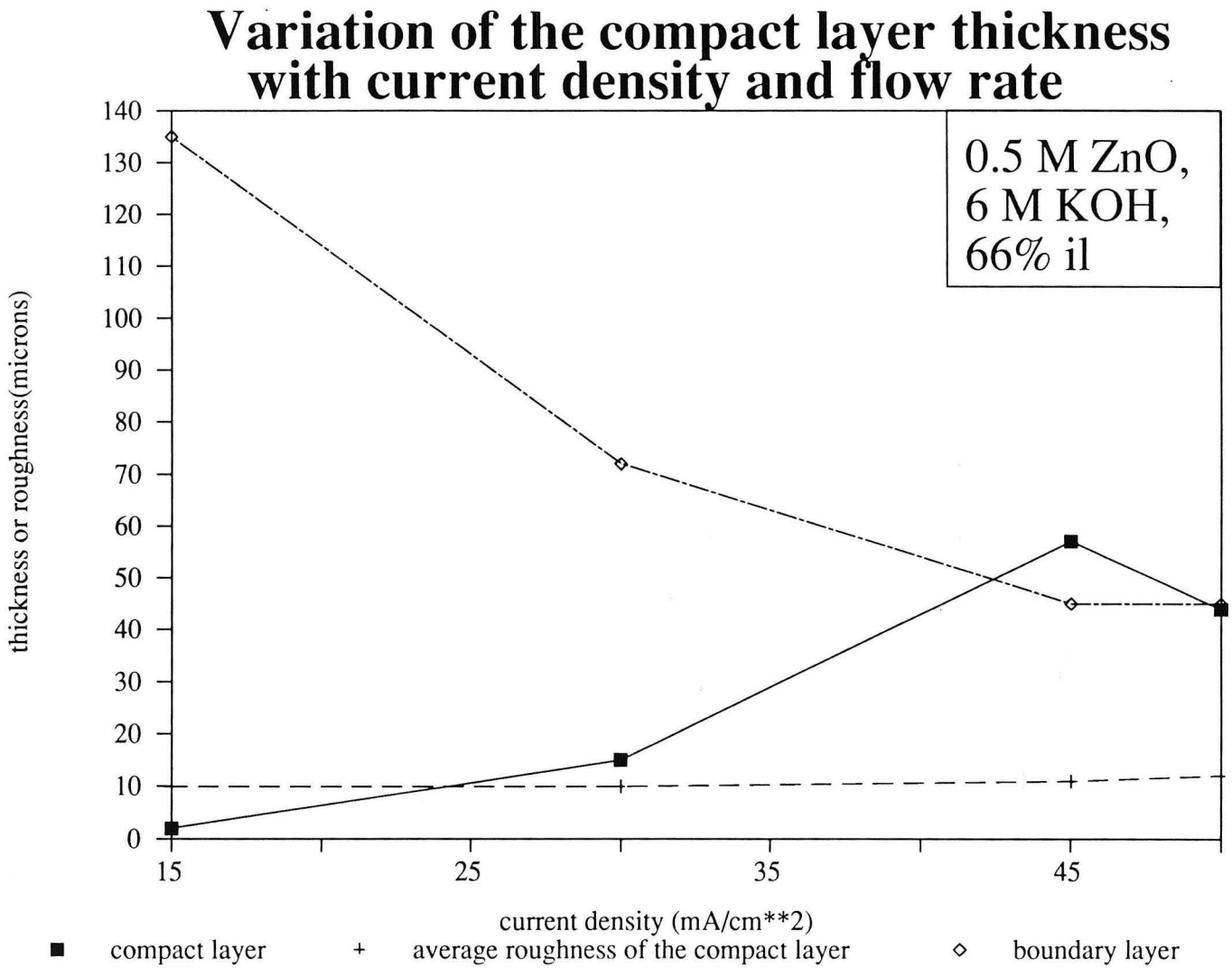

Figure 5.41

XBL 916-1255

COMPARISON OF THE COMPACT LAYER THICKNESSES AT DIFFERENT FRACTIONS OF THE LIMITING CURRENT

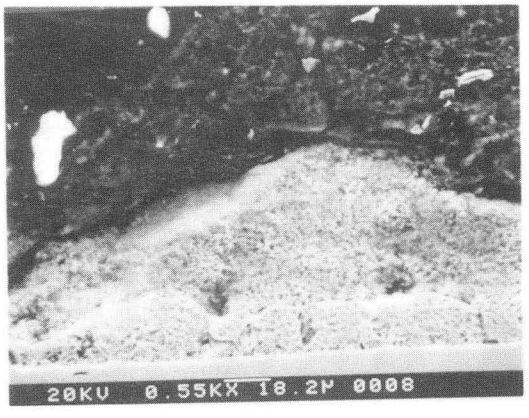

27 % i_l, compact layer thickness= 16 μm

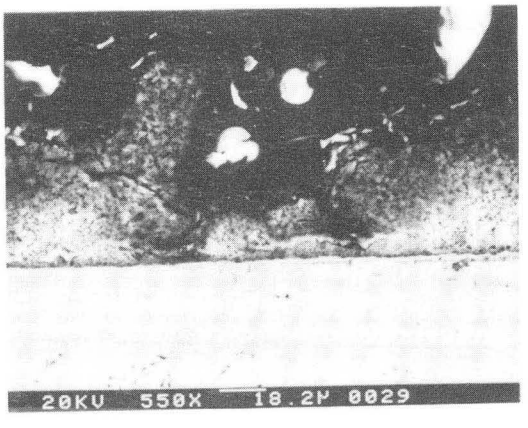

44 % i_l, compact layer thickness= 4 μm

0.5 M ZnO, 6 M KOH, 20 mA/cm^2

XBB 902-1025

Figure 5.42

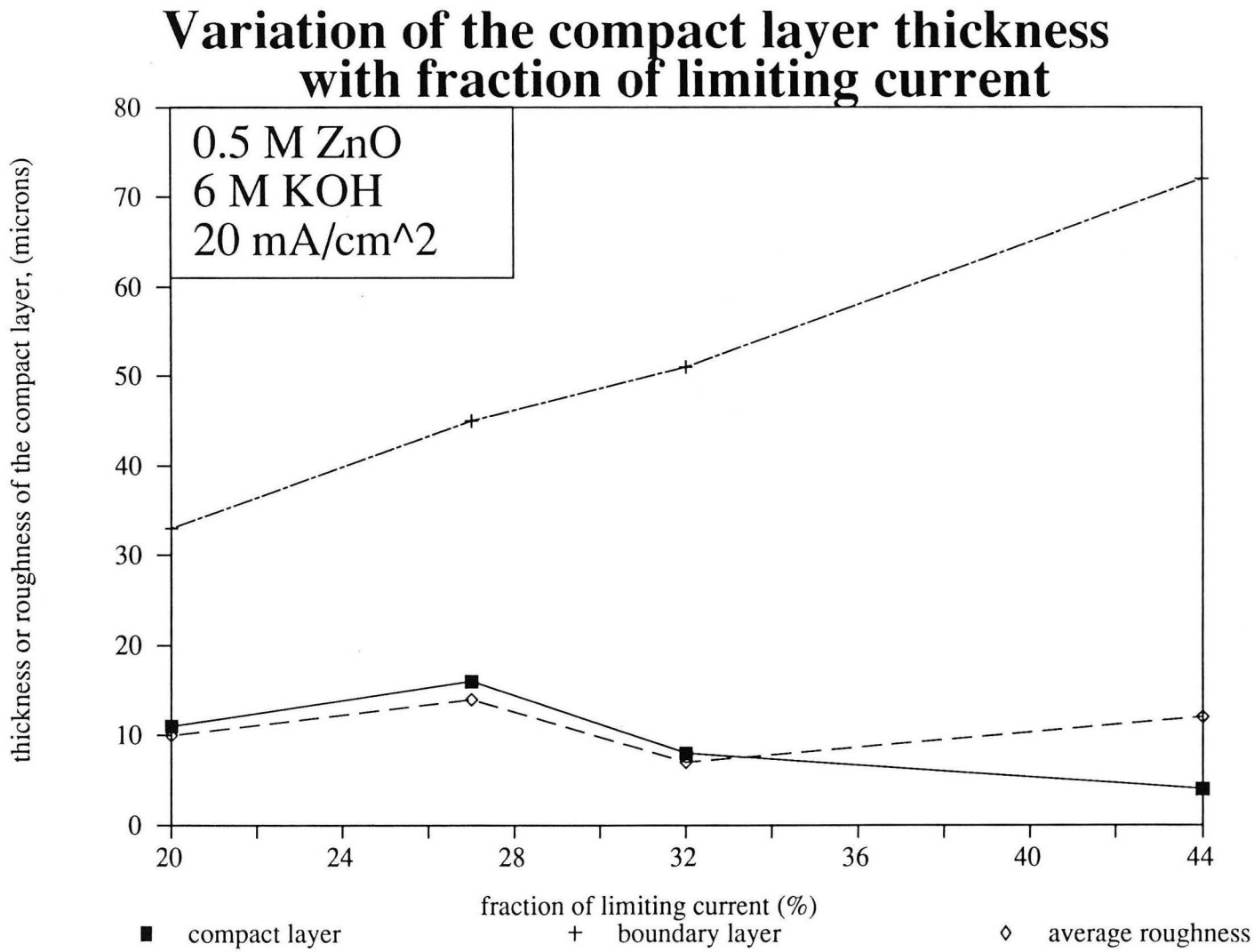

Figure 5.43

XBL 916-1256

COMPARISON OF THE COMPACT LAYER THICKNESSES

AT DIFFERENT FRACTIONS OF THE LIMITING CURRENT

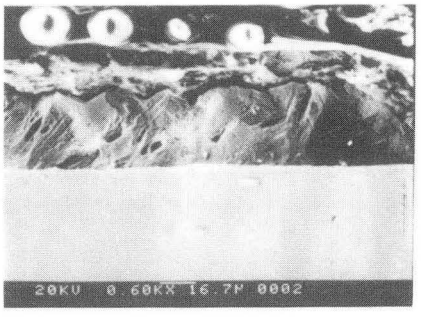

42 % i_l, compact layer thickness= 36 μm

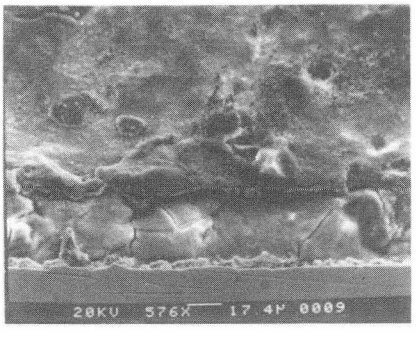

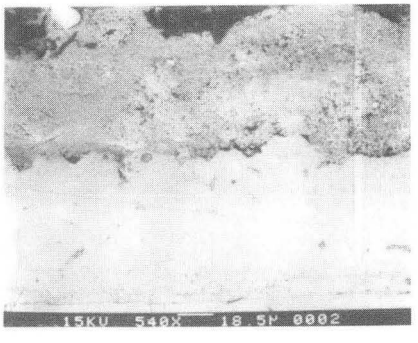

68 % i_l, compact layer thickness= 44 μm 110 % i_l, compact layer thickness= 77 μm

0.5 M ZnO, 6 M KOH, 50 mA/cm^2

XBB 901-375

Figure 5.44

Difference in the compact layer thickness with %il

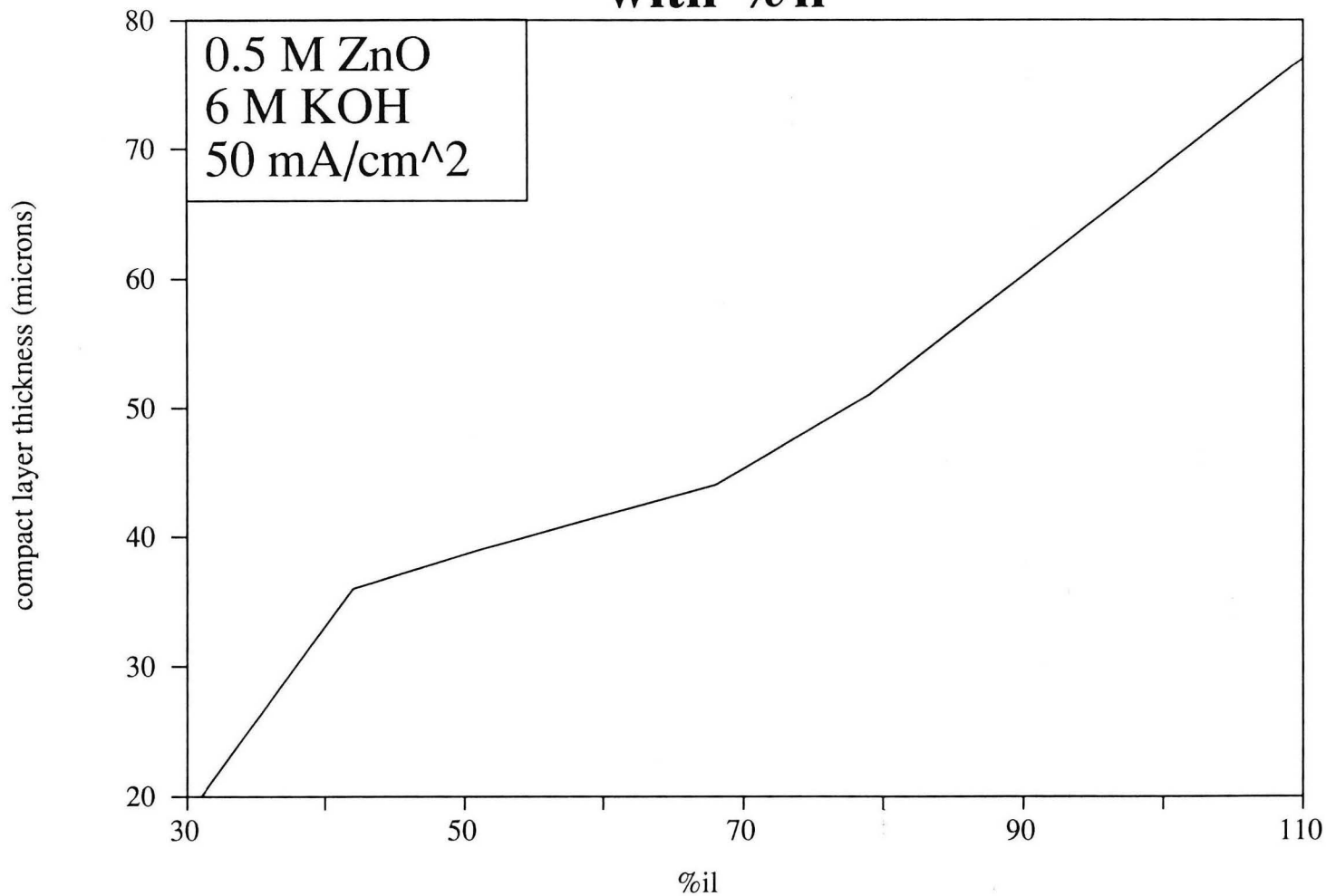

Figure 5.45

XBL 916-1257

COMPARISION OF THE COMPACT LAYER THICKNESSES WITH VARYING CURRENT DENSITY

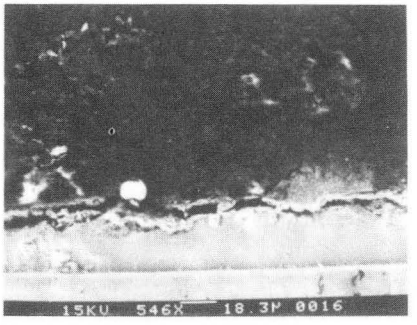

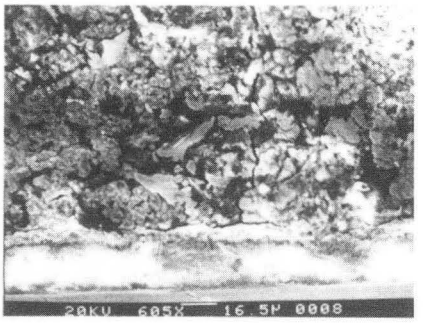

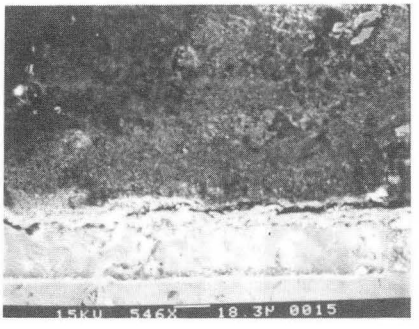

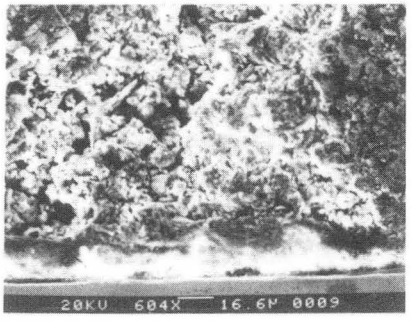

50 mA/cm^2, 10 μm deposited, 30 mA/cm^2, 69 μm deposited

compact layer thickness = 27 μm

30 mA/cm^2, 10 μm deposited, 50 mA/cm^2, 69 μm deposited

compact layer thickness = 19 μm

0.5 M ZnO, 6 M KOH, 250 rpm,
Re= 275, Ta= 4 X 10^5

XBB 901-382

Figure 5.46

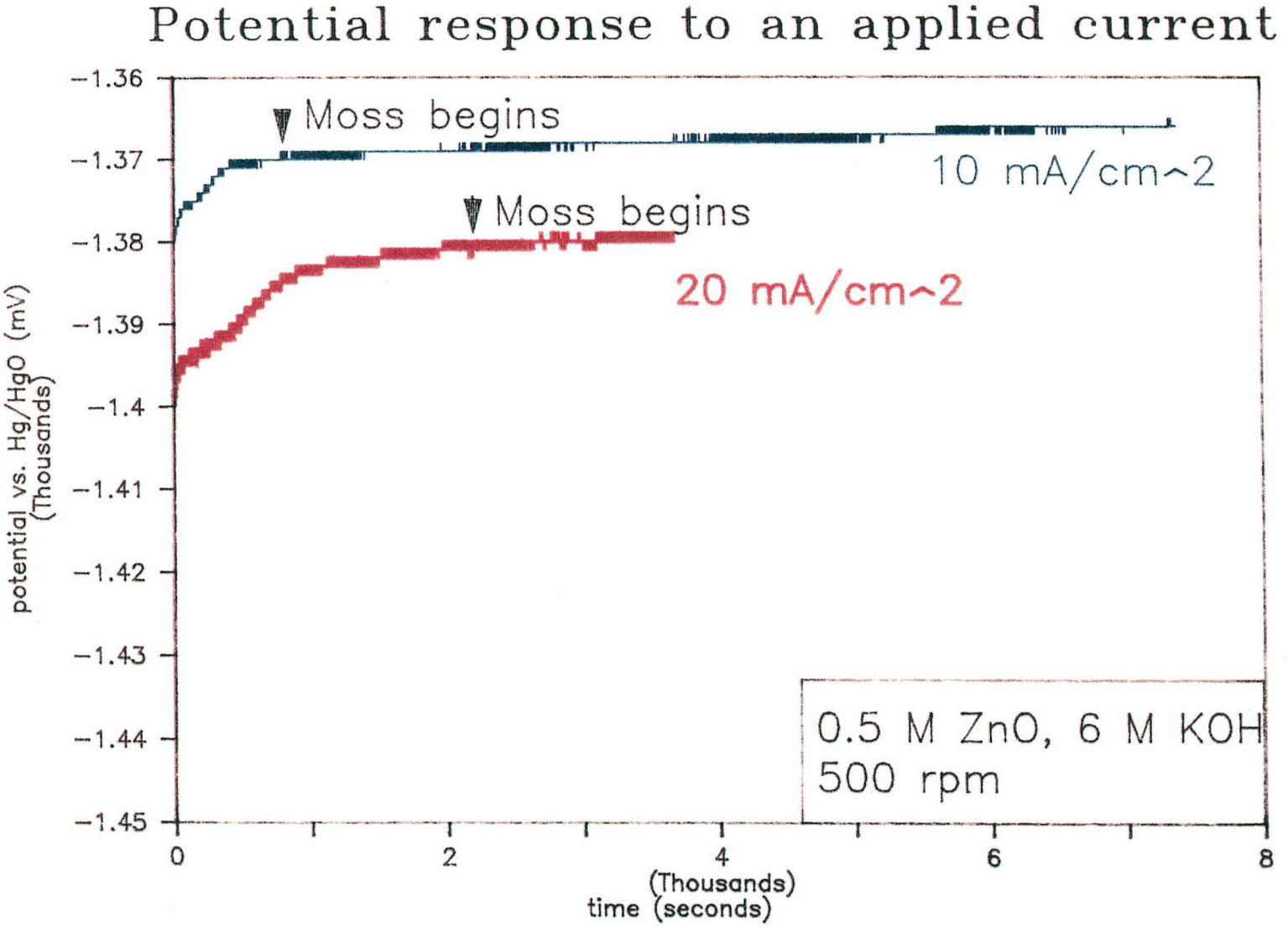

Figure 5.47

BBC 916-4586

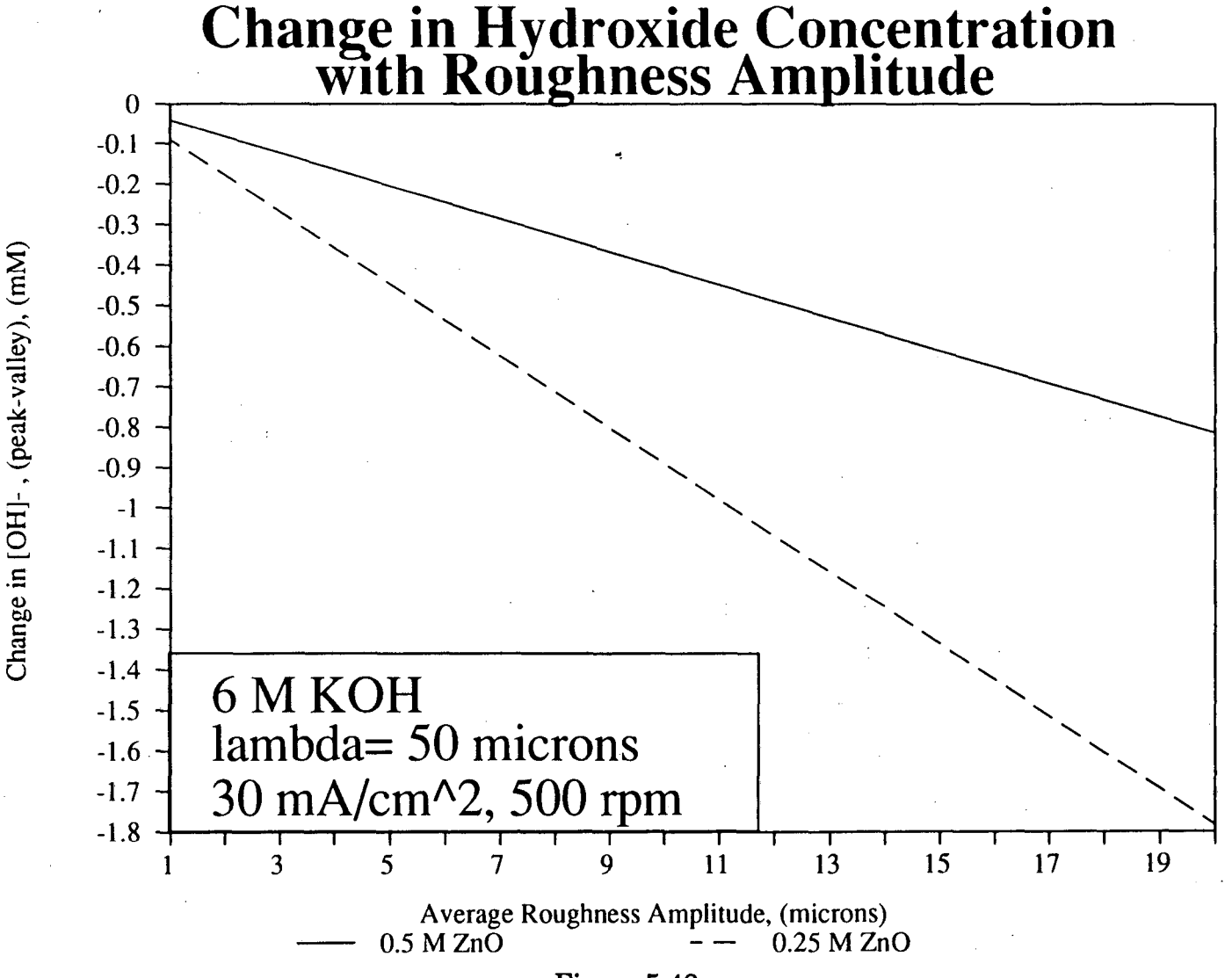

Figure 5.48

XBL 916-1258

Dependence of the Change in Hydroxide Concentration on [KOH]

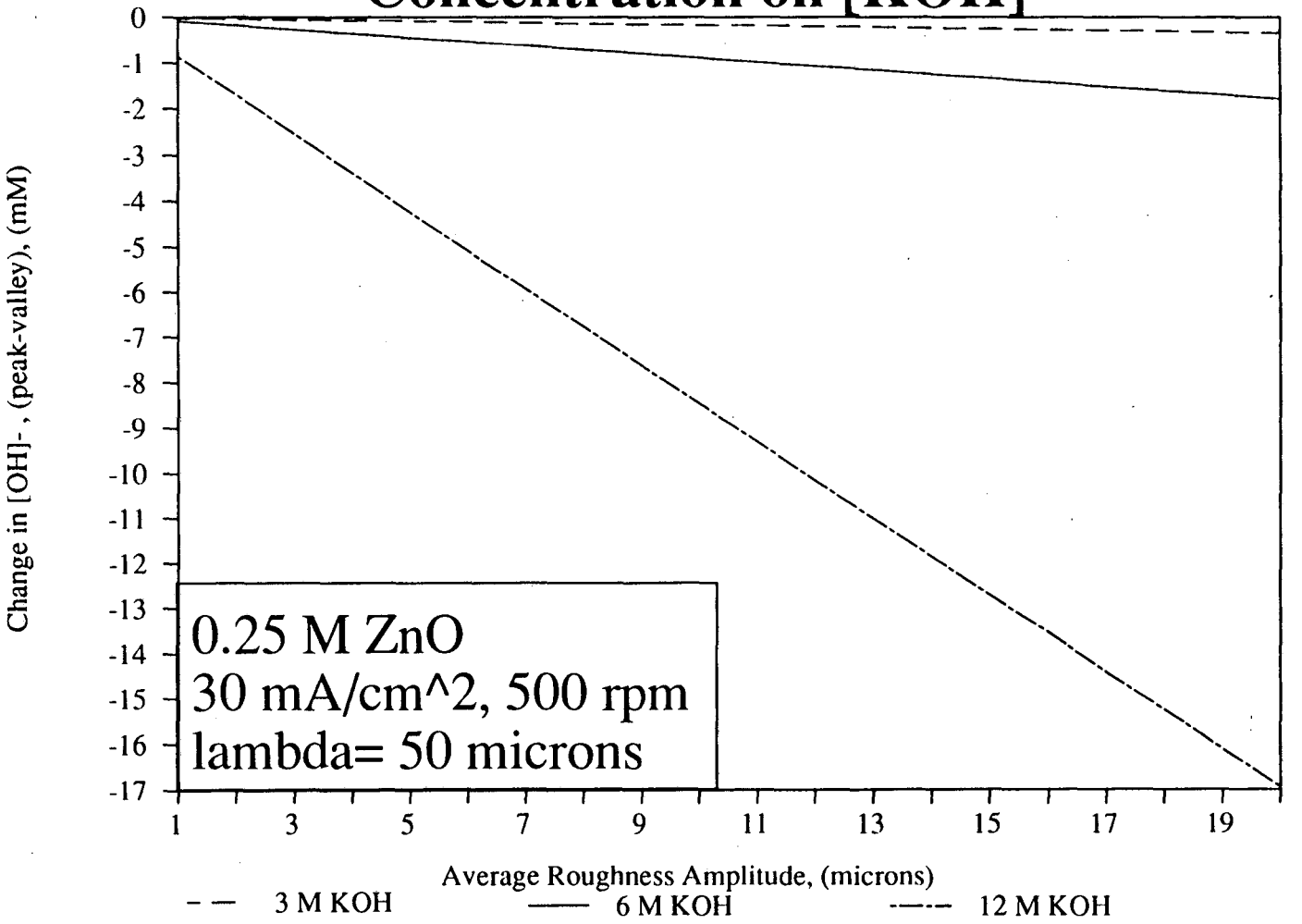

Figure 5.49

XBL 916-1259

Dependence of the Change in Hydroxide Concentration on Current Density

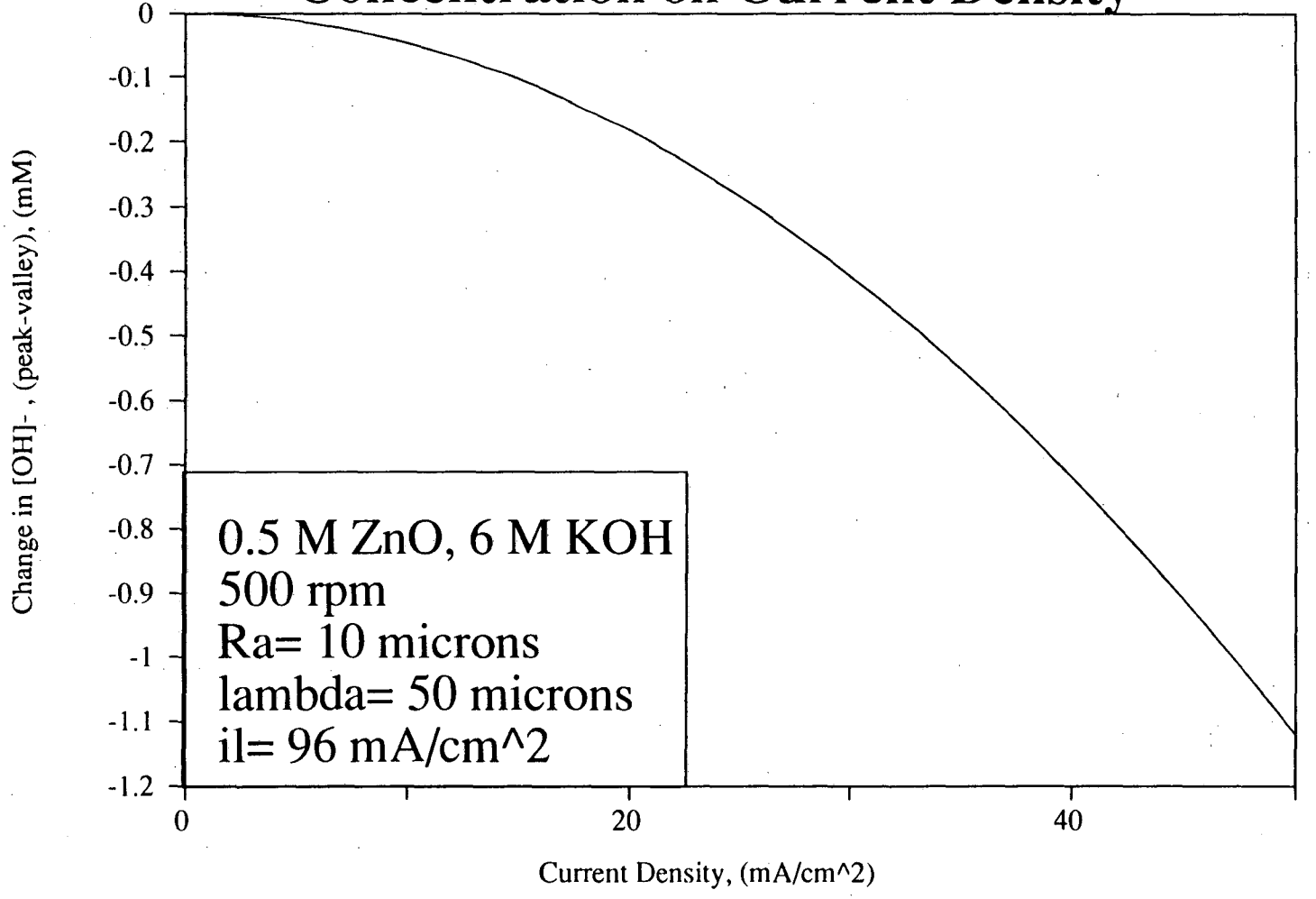

Figure 5.50

XBL 916-1260

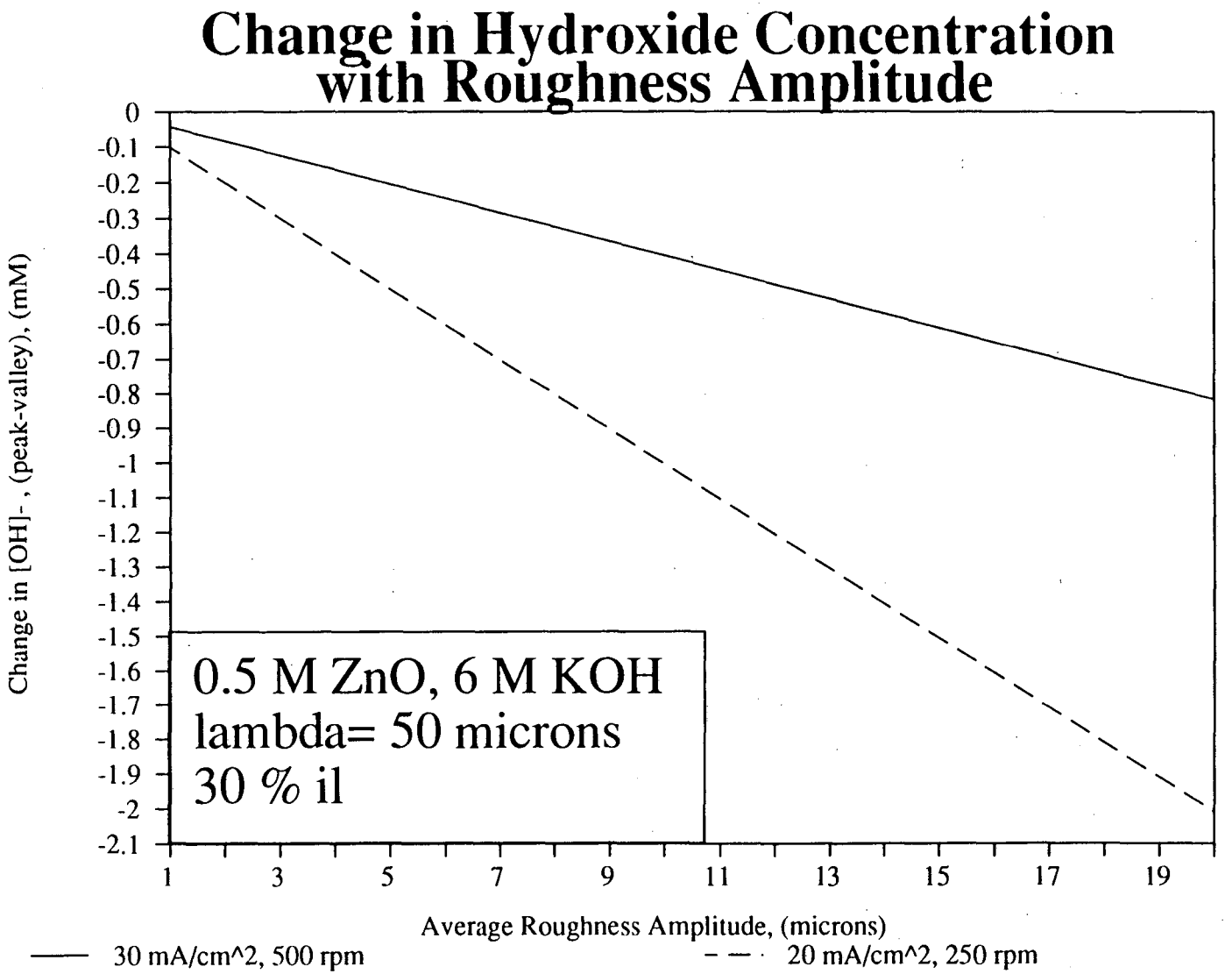

Figure 5.51

XBL 916-1261

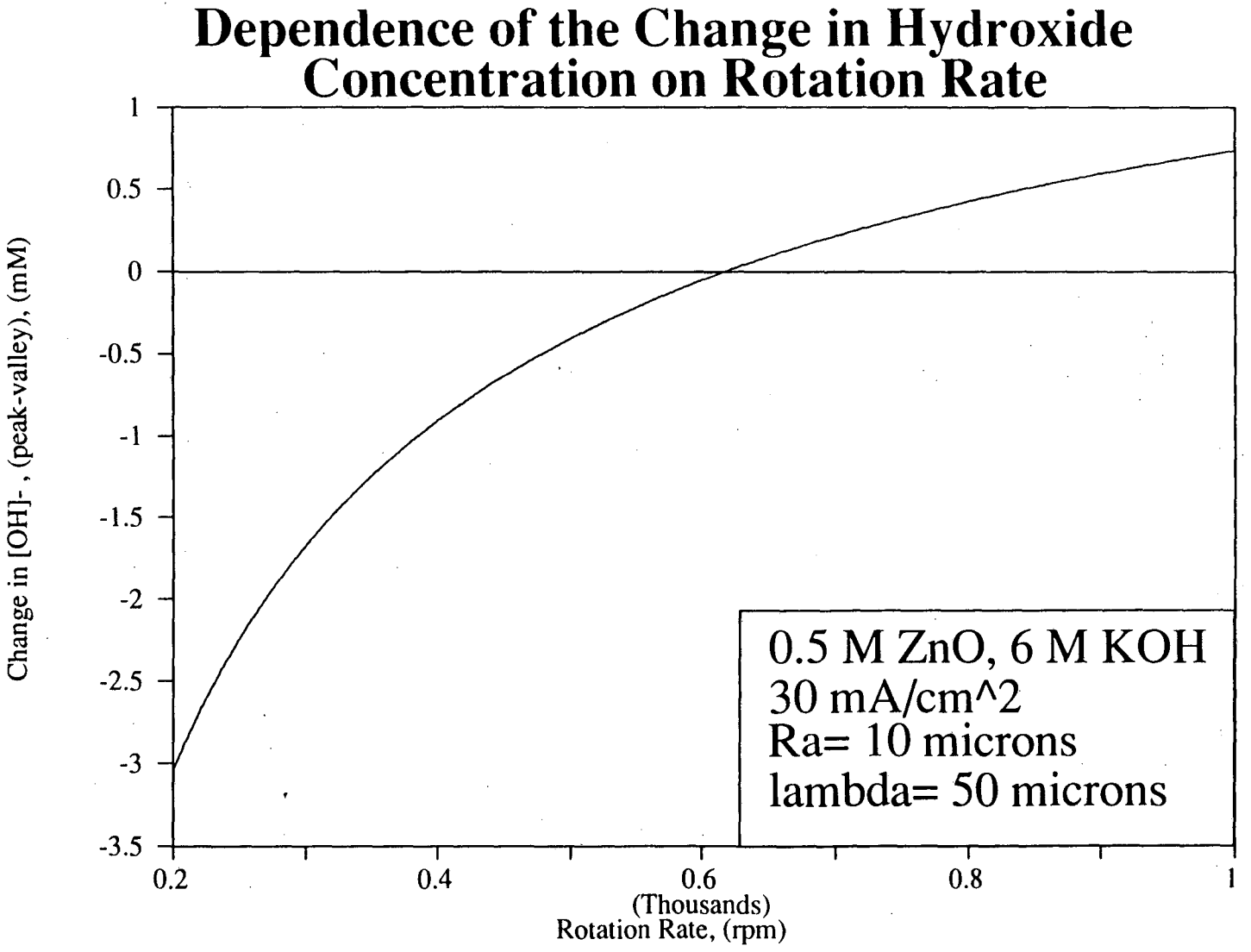

Figure 5.52

XBL 916-1262

Change in ip-iv with Roughness Amplitude

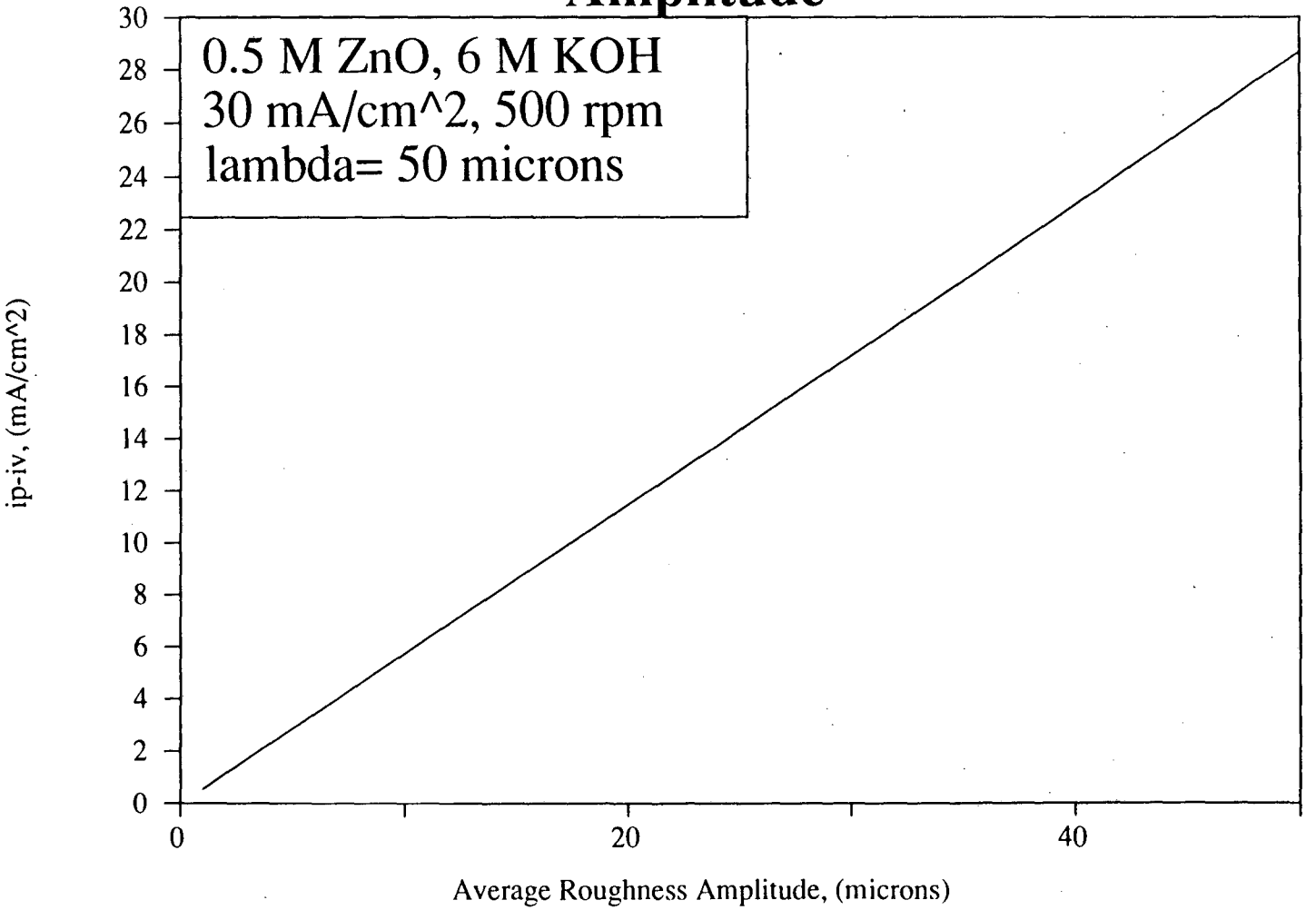

Figure 5.53

XBL 916-1263

SUMMARY AND CONCLUSIONS

Mossy zinc readily forms at low fractions of the limiting current density, regardless of the substrate or the cell geometry. It is characterized by a highly porous zinc structure composed of zinc filaments and adheres to the substrate poorly. Under the conditions studied, there is only one type of mossy zinc structure. In the current density range of interest in battery operation, moss appears only after the deposition of a substantially thick and rough compact layer. Moss initially forms on the areas of the electrode that have the worst mass transport or the lowest current density. Scanning electron microscopy has shown that the mossy structure is initiated both around large protrusions and in the crevices between growing crystal grains. Videomicroscopy has revealed that the emergence period is short, after which mossy zinc grows at a very fast rate compared to the compact layer. At first, the compact layer continues to grow; however, this growth stops once the moss nodules become dominant, because these surface features act as sinks for current.

Two sets of conditions always exist when moss is initiated: (1) relatively poor mass transport, and (2) the surface topography is dominated by large protrusions (this is the case at low current densities). The change in morphology is irreversible; however, the amount of charge passed before moss is initiated is determined by the deposition conditions. The following changes in the deposition conditions **promote** the growth of moss:

(1) Increasing the KOH concentration

(2) Decreasing the charging current density

(3) Lowering the flow rate

(4) Reducing the zinc oxide concentration

The most important factors influencing the compact layer thickness are the current density and the free hydroxide concentration (KOH). Increasing the supporting electrolyte concentration decreases both the compact layer thickness and the roughness required to initiate moss drastically. When the current density is low, the surface topography is dominated by a few protrusions. At low flow rates, these large nuclei have several effects: (1) they are sinks for current and (2) the valleys between protrusions are areas of decreased mass transport. As the magnitude of the current density is raised, the compact layer becomes thicker even if the fraction of the limiting current is kept constant. These two sets of results indicate that the roughness amplitude is a factor in the growth of moss. At a constant current density, but varying the fraction of the limiting current density, conflicting results were found. At a low current density, the compact layer thickness declined with increasing fraction of the limiting current. The opposite was true when a high current density is used. However, at high current densities, the roughness amplitude rises at a slower rate than it would if the applied current density was lower. It can be concluded that, at high current densities, the roughness elements have a greater tendency to merge, resulting in an increased roughness wavelength, a decreased roughness amplitude, and less moss.

When zinc is deposited from alkaline electrolytes, hydroxide ions are liberated. These ions diffuse and migrate away from the surface; however, in the valleys, the transport resistance dominates when the deposition conditions favor mossy zinc formation. As a result, the hydroxide concentration in the less accessible parts of the electrode is greater than it is elsewhere. A local buildup of this ion has several effects: (1) it enhances the rate of zinc deposition; (2) it blocks the sites for the zinc reaction, causing a change in crystal orientation; and (3) it shifts the equilibrium of the zincate complexes toward the more highly complexed species, resulting in a lowering of the local zinc concentration; (4) the potential is shifted in the cathodic direction. To confirm (4), the potential transient was measured and was found to gradually become level with time, after which moss was initiated, suggesting that the potential shift caused by the hydroxide buildup compensates for the potential decrease caused by

the increase in roughness. This combination of events results in a local change in the predominant crystal habit to crystal faces that are most favored for growth. These crystals grow laterally and outward, seeking zincate rich regions. The largest moss nodules become sinks for current, halting the growth of the compact layer and any small nodules of moss in their vicinity. They grow at a greatly enhanced rate without regard for the flow field.

The buildup of hydroxide ions is a function of the the deposition conditions. As the roughness or the KOH concentration becomes larger, the difference in the hydroxide concentration between the peaks and the valleys of a profile is worsened, so moss initiates more readily. As the current density (at the same fraction of the limiting current), flow rate, zinc concentration or wavelength increase, the change in the hydroxide concentration is predicted to be less; therefore, mossy zinc formation is inhibited. The model predicts that, for a given average roughness amplitude, a rise in the applied current density should produce a greater change in the hydroxide concentration from the peaks to the valleys. However, as the current density increases, merging of roughness elements becomes more likely, so there is a decrease in the roughness amplitude for the same charge passed, resulting in a smaller hydroxide ion buildup and less moss. These trends in the buildup of the hydroxide ions are in agreement with the observed trends in compact layer thickness; therefore, it can be concluded that hydroxide ions play a role in mossy zinc initiation.

FUTURE DIRECTIONS

While this work has looked into many questions arising in the formation of mossy zinc, there are directions which should be looked into on a deeper level. In this section, some future projects will be suggested.

1. In situ measurement of surface roughness during zinc deposition

In my project, the heights of roughness elements were measured ex-situ. In this continuation, the profiles would be measured in-situ and correlated with the initiation of mossy zinc. This could be accomplished using either STM or by an optical microscopic technique. Interference or phase contrast microscopy might be useful in this study.

2. Numerical analysis of the concentration and potential gradients during zinc deposition

This research would use the previously developed models of John Dukovic (66) and Ken Jordan (62) to examine theoretically the changes in the profiles and in the concentration fields as deposition proceeds. It would look at the effects of a change in deposition conditions and connect the appearance of moss with the perturbations in the deposition parameters.

3. TEM analysis of the strata of zinc

Cross- sectional transmission electron microscopy will be used to examine the crystal structure of the compact layer, the mossy layer, and the associated interface. The types of defects would be characterized and compared.

4. Adsorption and desorption of OH^- *on zinc surfaces*

The surface coverage of OH^- would be examined as a function of potential and flux of the hydroxide ion. RAMAN spectroscopy might be useful in this study.

APPENDIX 1- ALKALINE ZINC BATTERY SYSTEMS

Zinc is the most common negative electrode in primary batteries and has been used since the advent of the earliest galvanic cells in the early 1800's. Presently, alkaline zinc/manganese dioxide primary cells, marketed under such well known names as *Eveready* and *Duracell,* have the greatest worldwide sales. Within the last 30 years, alkaline zinc secondary batteries have also been of technical interest, and some batteries have become commercially viable. These secondary cells offer the advantages of low cost, low equivalent weight, ambient temperature operation, and moderately high battery voltage(1). The specific energy and power of these rechargeable batteries is high; therefore, potential applications are likely to include space vehicles, electric cars, and military communications (1, 67).

A-1.1 The Zinc/Air Battery

The zinc/air cell is unique in that one reacting species, oxygen, is not provided by a liquid electrolyte; thus, the battery weight is reduced and the energy density is increased(68). When an alkaline KOH electrolyte is used, the cell has both a high theoretical specific energy density, 1.33 kW hr/ kg, and a high cell voltage, 1.6 V.

Several half reactions have been proposed, but most researchers agree that the air electrode reaction is:

$$\frac{1}{2}O_2 + H_2O + 2e^- \rightleftarrows 2(OH)^- \qquad \text{(A-1-1)}$$

When using mechanically recharged electrodes, another possible charging reaction, that would be performed at the recharge station, was suggested by Foller(69):

$$2(OH)^- + H_2 \rightleftarrows H_2O + 2e^- \qquad \text{(A-1-2)}$$

The zinc electrode can react in several ways. At low zincate concentrations, the half cell reaction is:

$$Zn + 4(OH)^- \rightleftharpoons Zn(OH)_4^{-2} + 2e^- \qquad \text{(A-1-3)}$$

As the zincate concentration approaches the solubility limit on discharge, oxide formation becomes more important:

$$Zn(OH)_4^{-2} \rightleftharpoons ZnO + H_2O + 2(OH)^- \qquad \text{(A-1-4)}$$

Oxide formation both reduces the zincate concentration in the electrolyte, and causes passivation of the zinc electrode (70). The latter is a problem in both flowing and non-flowing media; however, in flowing media, substantial loadings can be achieved before the zinc electrode passivates (67).

Foller(69) discusses two other important reactions in the zinc/air battery. These are the self discharge reaction,

$$Zn + 2H_2O + 2OH^- \rightleftharpoons Zn(OH)_4^{-2} + H_2 \qquad \text{(A-1-5)}$$

and the parasitic reaction:

$$2H_2O + 2e^- \rightleftharpoons H_2 + 2OH^- \qquad \text{(A-1-6)}$$

The parasitic reaction occurs on charging the zinc cathode, where hydrogen evolution is thermodynamically favored but is kinetically limited.

Many different zinc/air cell designs have been proposed, some employing slurry electrodes and mechanical recharge, others having planar electrodes and electrical recharge. Both flowing and non-flowing battery configurations have been evaluated. Typical schematic designs for one of these cells are shown in Figure A-1.1 The forced convection system offers

the additional advantage of increased efficiency and reduced size, both crucial in electric cars (71). A basic cell usually consists of an air electrode, a porous spacer , a separator, an electrolyte compartment and a zinc electrode. Generally, the electrolyte is potassium hydroxide saturated with zinc oxide.

The porous air electrode is fabricated from a mixture of nickel, catalyst, and teflon; the latter is added to render the air electrode is hydrophobic and easily accessible to gas. Several catalysts, including platinum, silver, nickel oxide, and cobalt oxide, have been investigated. Corrosion resistant carbons with transition metal oxides as catalysts have also been evaluated as substrates for oxygen evolution; these electrodes showed promising cycle life characteristics (68).

For current collection, copper, magnesium, silver, nickel, and stainless steel substrates for zinc electrodes have been considered. In slurry electrodes, a fine copper expanded metal screen is used, because copper has good resistance to corrosion and alloys with the discharging zinc slurry. Porous copper electrodes were evaluated by Ross (68) in his zinc/air cell performance studies and it was found that these substrates were excellent for zinc deposition. On magnesium electrodes, zinc exhibits poor adherence; however, this substrate is useful in zinc slurry cells, where the deposition of a fine powder is desirable. Magnesium would not be considered a suitable planar electrode for zinc deposition. Silver and nickel offer good resistance to chemical attack under highly alkaline conditions, and a high cycle life has been demonstrated when either of these metals is used as a substrate for the zinc electrode (72). However, the cost of these metals renders the zinc/air cell uneconomical. Stainless steel current collectors were used in the CGE design zinc/air cell that had an announced energy density of 110 W- hr/kg and a specific power of 80 W/kg with 40% overall efficiency (73). However, ferric and ferrous ions are well known dendrite promoters, so it appears unlikely that a stainless steel based zinc electrode is appropriate for the zinc/air cell.

The zinc/ air battery still has several technical problems involving both air and zinc electrodes. Carbon dioxide removal from the electrolyte and electrode stability are major problems with the air electrode(67). To circumvent these difficulties, an acid zinc/air cell was proposed (74), however, oxygen absorption and zinc self discharge are problems when acidic media are used(75).

High cathodic overpotentials, caused by the sluggish kinetics of oxygen reduction, is another major factor contributing to the low overall efficiency of the zinc/air cell (69). External, mechanical recharge involving an alternate reaction, the combination of hydrogen gas with hydroxide ions (cf. equation A-1-2), was evaluated by Foller (69), who found that this method circumvented the oxygen electrode's slow kinetics and resulted in improved overall efficiency. Air electrodes consisting of transition metal oxide catalysts in a carbon matrix have been proposed by several researchers (68, 76); these electrodes lowered the cost of the battery, while also being stable in the harshly alkaline conditions of the zinc/air cell. Graphite based electrodes with transition metal catalysts have also been reported to enhance the cycle life of the zinc/air cell (68).

At the zinc electrode, shape change and dendrite growth remain problems. Both phenomena have been extensively studied, and although our understanding has greatly increased, solutions to these technical difficulties are still being sought.

Slurry electrodes and mechanical recharge alleviate the problems of shape change and dendritic growth, although other problems arise. In batteries with slurry electrodes, shunt currents occur because zinc particles agglomerate in the direction of the potential gradient. According to Katan and co-workers (77), zinc particles move in the direction of the potential gradient by a mechanism involving zinc deposition on one side of the particle and dissolution on the other. Zinc particles can settle, causing short circuits, and battery failure. When using zinc slurry electrodes, the current collector, 90% of the total cell weight, must be optimally designed to maximize the system power density (69).

A-1.2 The Zinc/Ferricyanide Battery

The zinc/ferricyanide cell concept was advanced in about 1978; thus, it is still in the early stages of development(78). Potential applications for this battery include energy storage for solar cells and load leveling at electric power plants. As shown in Figure A-1.2, the zinc/redox cell uses forced convection and is similar in design to the zinc/bromine cell. This cell has a high cell voltage, 1.63V, and operates at ambient temperature, since both the zinc and redox reactions have fast kinetics. The major advantage of this battery over the zinc/air cell is that the air electrode is replaced by a highly reversible ferricyanide/ ferrocyanide electrode, thus circumventing the numerous cell problems caused by the air electrode.

The half reactions in this cell are:

$$Fe(CN)_6^{-3} + e^- \rightleftarrows Fe(CN)_6^{-4} \qquad \text{(A-1-7)}$$

$$Zn + 4(OH)^- \rightleftarrows Zn(OH)_4^{-2} + 2e^- \qquad \text{(A-1-8)}$$

On discharge, the active materials precipitate out of solution and are stored in the external reservoirs, a process that reduces the bulk of the zinc/ferricyanide battery(79). When the cell is charged, the discharge products redissolve providing a saturated sodium ferrocyanide or sodium zincate cell electrolyte (78).

The zinc/ferricyanide cell uses a dense carbon felt as the ferricyanide electrode, and a cadmium plated iron substrate as the zinc electrode. Since the ferricyanide and ferrocyanide ions migrate toward the anode on discharge, a cation conducting separator is necessary to prevent electrolyte mixing. Because sodium ferrocyanide has a large heat of crystallization, heat exchangers are also needed (79).

Several problems with the zinc electrode remain. Like all zinc batteries, there are problems when zinc is deposited and ways to consistently control the zinc morphology have not

been found. Shape change, mossy zinc formation and dendrite growth are all morphological problems that need better understanding. Currently, the cycle life of this battery is only about 100 cycles with an overall efficiency of 62%; achievement of improved cycle life and efficiency requires further research efforts.

The knowledge of the ferricyanide/ferrocyanide couple in strongly alkaline media, 5M NaOH in the zinc/ferricyanide battery, is sorely lacking. Mc Breen (79) suggested that ferricyanide complexes decompose through the stepwise substitution of cyanide ions by hydroxyl ions, although this problem is greatly mitigated by the removal of heavy metal ions from the electrolyte. Ferricyanide and ferrocyanide ions can form cationic complexes with sodium ions in the supporting electrolyte (79).

Other cell engineering problems remain as well. Handling of zinc oxide, sodium ferrocyanide and sodium ferricyanide, still cause difficulties, although work on solids handling done in connection with the development of the zinc/chlorine cell may be applicable to the zinc/ferricyanide cell. Separator material selection and engineering of multicell stacks also remain technical problems in the development of a viable zinc/ferricyanide cell; however, these problems are not insurmountable.

A-1.3 The Zinc/Nickel Oxide Battery

Currently one of the most reliable secondary zinc cells, the zinc/ nickel oxide battery is a prime candidate for electric vehicle power in the near term (79). It offers excellent low temperature performance, and recent developments have led to great improvements in cycle life. Over 300 cycles at an overall efficiency of 85% have been achieved in test cells, and like other zinc cells, the zinc/nickel oxide battery offers a moderately high cell voltage, 1.74 V. However, the theoretical energy density, 373 W-hr/kg, is significantly lower than that of other zinc secondary batteries.

The half reactions in this battery are:

$$Zn + 2H_2O \rightleftharpoons Zn(OH)_2 + 2H^+ + 2e^- \qquad \text{(A-1-9)}$$

$$2NiOOH + 2H_2O + 2e^- \rightleftharpoons 2Ni(OH)_2 + 2OH^- \qquad \text{(A-1-10)}$$

When the cell is discharged, the zinc electrode is oxidized to $Zn(OH)_2$ which complexes in solution forming ions of the type $Zn(OH)_n^{-(n-2)}$. Zinc oxide may also be precipitated onto the zinc electrode, causing passivation.

The cell consists of a porous nickel electrode, a separator, an electrolyte compartment, and a zinc electrode. Unlike the zinc/air and zinc/ferricyanide cells, the zinc/nickel oxide battery does not employ forced convection, although the use of flow has been evaluated (71).

The nickel electrode is either a sintered, porous nickel sponge or a nickel powder bonded to a current collector using a polymeric binder (1). The zinc electrode is prepared by bonding zinc powder to a current collector. A variety of bonding processes and current collector substrates have been evaluated (1).

Many of the technological problems of the zinc/nickel oxide battery have been solved, making this cell a viable candidate for electric vehicle propulsion in the near term (79). Using careful engineering, great improvements in cycle life have been achieved, and currently zinc/nickel oxide cells can attain over 300 cycles with an excellent overall efficiency of 85% (79). By using improved separators and modified charging methods, the dendrite problem has been greatly mitigated, although densification and shape change of the zinc electrode are still open problems. Efforts are being made to produce low cost nickel electrodes, because the cost of the zinc/nickel oxide cell is high, roughly 100 dollars/kWhr.

A-1.4 The Zinc/Silver Oxide Battery

For applications requiring high specific power and where cost is irrelevant, the zinc/silver oxide cell is of interest. This secondary cell has a cell voltage of 1.86 V and can deliver a specific energy of 200 W hr/kg (1). The design of this cell is very similar to the zinc/nickel oxide cell; it uses porous silver and zinc electrodes in a non flowing configuration. Like the zinc/nickel oxide cell, the remaining technical problems include shape change, densification of the zinc electrode, cycle life cost, and prevention of zinc self-discharge.

Figure Captions

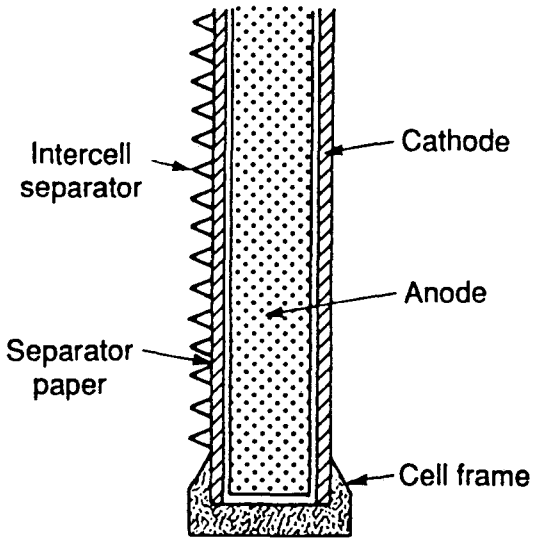
Intercell
separator
Cathode
Anode
Separator
paper
Cell frame

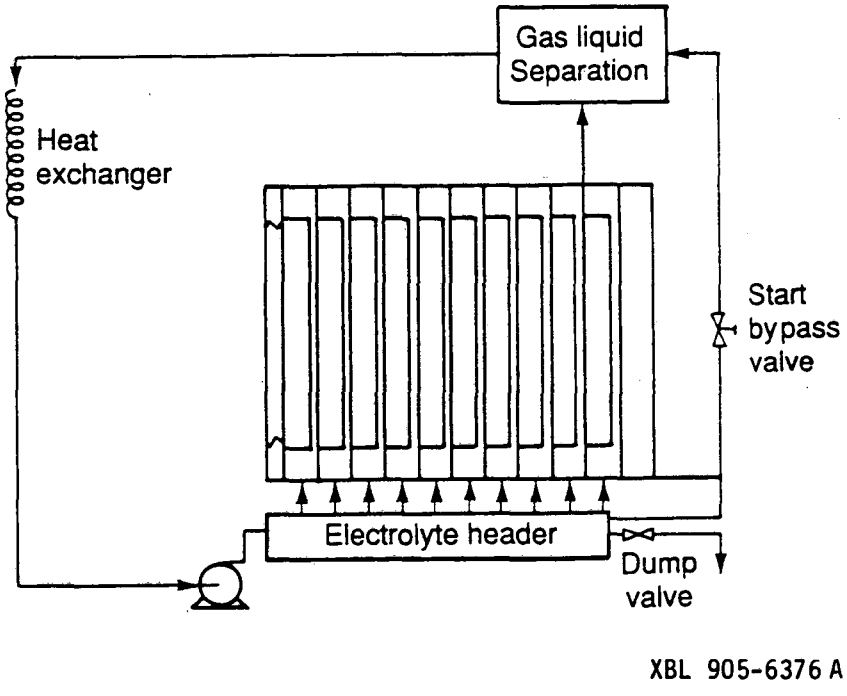
Gas liquid
Separation
Heat
exchanger
Start
bypass
valve
Electrolyte header
Dump
valve
XBL 905-6376 A

Figure A-1.1

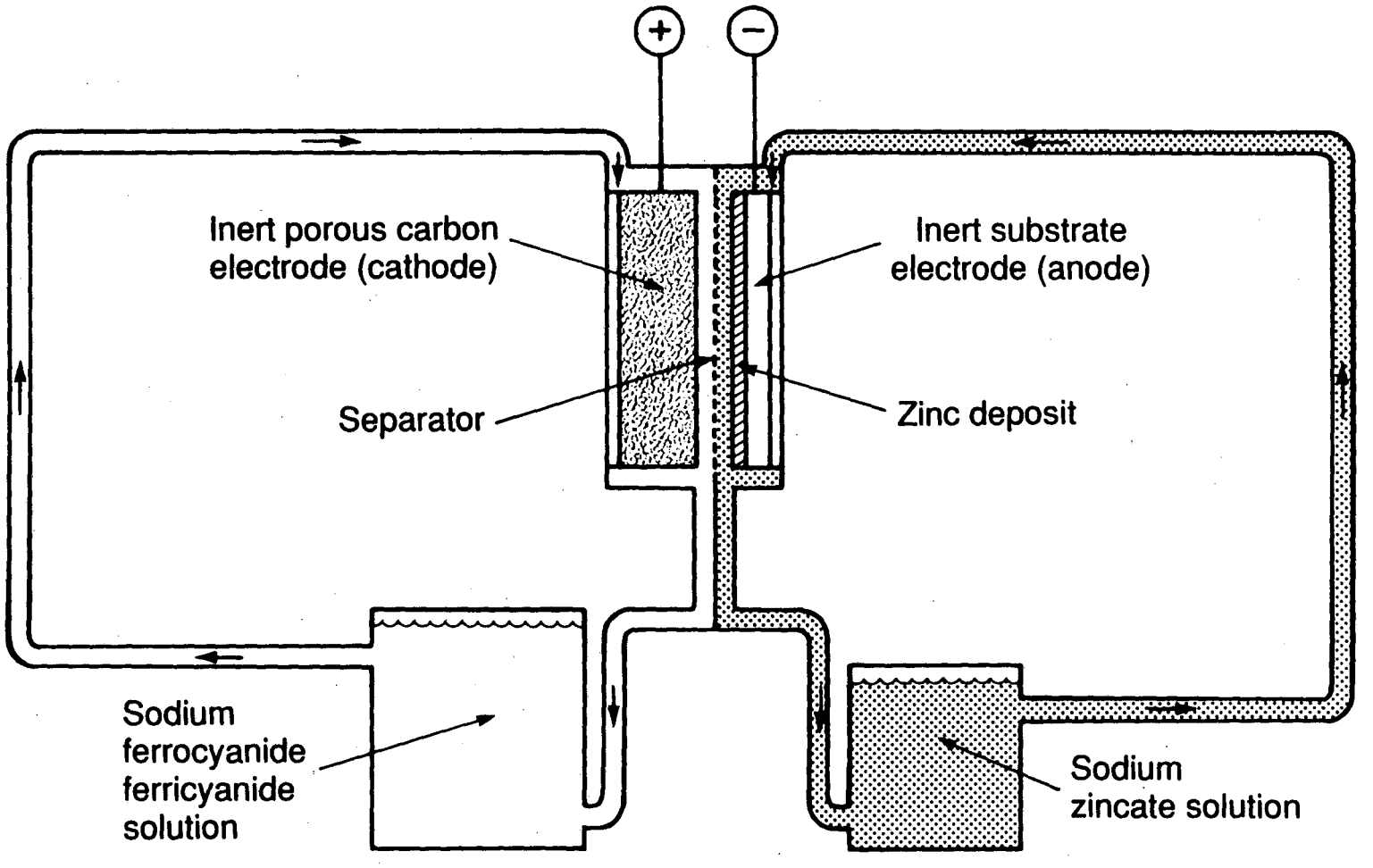

Figure A-1.2

XBL 905-6383

APPENDIX 2- EFFECT OF DEFECTS ON THE ELECTROCRYSTALLIZATION PROCESS

A-2.1 Origins of Defects

Defects can affect the metal deposition process, because they are favored locations for the charging reaction. Although there are many sources of defects in electrodeposited metals, the substrate is probably the most important source of dislocations in thin electrodeposits. When metal is first deposited, a thin alloy layer is usually formed with the substrate, after which three dimensional, epitaxial crystallites are nucleated. Metal deposits preferentially where the nucleation overpotential is lowest, at surface imperfections; thus, surface defects are propagated into the bulk electrodeposit(80). Subsequent deposition occurs preferentially on existing crystals, so the imperfections of the basis metal can extend far into the electrodeposit and possibly affect the morphology. Typically, substrate effects disappear at an electrodeposit thickness of about 1000 Å.

Since stresses caused by misfit between the surface and the electrodeposit can result in defect generation, there should be an influence of the basis metal on electrodeposition which would be manifested in the surface overpotential. Here, generation of defects is a result of the difference in the lattice parameter, a, between the substrate and the electrodeposit; this is illustrated in Figure A-2.1(a). The phenomena of substrate effects in the electrodeposition process was observed first by Pangaroff(53) and later by Mc Breen and co-workers(81). Both Pangaroff and Mc Breen observed differences in orientation depending on the basis metal, and Pangaroff reported that these differences became less as the thickness of the deposit increased. Weil(80) reported that electrodeposits typically contained more dislocations than metals prepared by conventional means, and that these defects originated because of stresses generated during deposition. The dislocations were generated by the addition of extra lattice planes, and the dislocation lines were curved relative to the applied stress of misfit.

Because of slight misfits in orientation, dislocations are formed when three dimensional nuclei interact; this is shown in Figure A-2.1(b). As the applied overpotential is raised, the density of nuclei increases exponentially; thus, more dislocations are produced. Lamb and co-workers(82) undertook an extensive study of copper deposition, covering a range of current densities and additive concentrations. Their results unequivocally show a dramatic increase in hardness with current density, indicating that the dislocation density is influenced by interactions of three dimensional nuclei.

Impurities play an important and complex role in the electrodeposition process, especially when less noble metals are deposited. When co-deposited with a metal such as zinc, metallic impurities lower the overvoltage for the evolution of hydrogen. Impurity atoms inevitably have a different atomic size than the bulk lattice; therefore, the misplacement can result in the generation of other crystal defects, as pictured in Figure A-2.1(c). Although stress related defects can be generated in the bulk electrodeposit, the major effect of impurity deposition is the nucleation of twins, a result of the impurity atom's slight misplacement in the crystal lattice(80).

While the effects of impurity and additive incorporation are similar, additives can have other dramatic effects on the electrodeposit. Typically, additives are large complexes which, unlike impurities, are intentionally added to the electrolyte to improve the electrodeposit. A successful additive will cause the grain size of the electrodeposit to decrease, resulting in a smoother and brighter deposit. Lamb(82) examined the role of incorporated additives on the deposit properties and found that gelatin additions increased the hardness, a direct result of the change in grain size. However, this additive also increased the deposit's internal stress, indicating that some of the additive was being incorporated into the crystal and was causing the generation of stress related defects.

A-2.2 Effect of Crystalline Imperfections

Early workers believed that crystallization occurred via the formation of two dimensional nuclei and the extension of existing crystal faces. A high overpotential is needed to form two dimensional nuclei, and if this energy is not continuously supplied to the surface, crystal growth stops after the completion of one monolayer (7). However, as long as an adequate supply of reactant is maintained, crystals continue to grow indefinitely.

As the nature of crystalline imperfections became known, their effect on the electrocrystallization process came to be an open scientific question. Franck and co-workers (83) showed that surface dislocations provided sites favorable for nucleation where, at low degrees of supersaturation, rapid crystal growth was possible, thereby explaining the observations that only a low degree of supersaturation is required for crystal growth. At a dislocation, the incomplete monolayer results in an atomic step upon which atoms can deposit without two dimensional nucleation. Therefore, crystal growth can continue indefinitely, even at low degrees of supersaturation. As shown in Figure A-2.2, an atom will first adsorb at a surface site, where deposition is less favorable, and then it diffuses to a site on the dislocation step. Finally, the adatom diffuses to a kink site. Because the atomic coordination and bonding forces are increased at the base of the atomic step, deposition is more energetically favorable at the kink. At this site, the atom is tightly bound, incorporated into the lattice and forms a new kink site.

In an electrocrystallization process, three dimensional nucleation is usually a continuous process. Deposition is favored at those sites having the lowest nucleation overpotential; that is, deposition at defects, especially grain boundaries, dislocations, and impurity clusters, is favored. The orientation is not necessarily the same as the previously grown crystal, and could have a faster growth rate than the bulk electrodeposit. This situation would result in the appearance of an instability, which will either propagate or disappear in accordance with

stability criteria(33). The nucleation of a new crystal phase on a surface defect could result in an instability causing some morphological phenomena.

While point defects and impurities may have detrimental effects on the morphology, they may also benefit crystal growth, as some impurities increase the binding energy of the host atom to the interface(84). The impurity stabilizes the thermodynamically unstable host nucleus and lowers the overpotential for metal deposition(85, 86). However, most impurities lower the overpotential for detrimental side reactions, particularly hydrogen evolution. An enhanced rate of gas evolution results both in an increase in energy consumption and in blocking of the surface by gas bubbles.

Frank (83) showed that, in addition to providing sites for crystallite growth, dislocations affected the growing crystal's macromorphology. The morphology can be affected by an array of surface dislocations, which pin the crystal behind dislocation lines; this is shown in Figure A-2.3. When the crystal is pinned, the sites at the dislocation base are no longer favored for deposition, although some atoms will still deposit at these sites, enabling further coverage by the depositing metal. Monolayer bunching at a dislocation may lead to microscopic terracing of the deposit; the terrace sides are related to the dislocation's Burgers vector.

Microscopic terracing can also be caused by slight misorientations in the electrodeposit stacking. In a study by Bockris and co-workers(86), electrochemistry was performed on well characterized zinc surfaces which contained steps oriented along the {0001} and $\{\bar{1}100\}$ planes at varying angles to the perpendicular axis. It was postulated that if a high index plane could be formed from steps bounded by dislocations, then the widening of steps with time could be predicted. Although they expected that the width of layers would increase linearly with time, the rate of increase was dependent on the crystal's angle to the perpendicular axis. As a result, the conclusion was made that primary steps were formed by a mechanism involving the propagation of submicroscopic steps, caused by slight misorientations in the electrodeposit stacking.

Partial dislocations, imperfections in which the crystal lattice is not displaced by a full atomic position, have important effects on the deposit morphology. While the sites on the partial dislocation's terrace are favorable for crystal growth, the crystal nucleus has a twin relationship with the substrate. When a crystal nucleated at a perfect dislocation meets one grown from a partial dislocation, there are always defects generated.

Screw dislocations can have many important effects on the morphology. Since nucleation is unnecessary on these sites, they are an important source of boulder growths, which can grow into either dendrites or striations (if flow is present). The protrusions cover the surface and form terraced growth pyramids, which are epitaxially aligned with the substrate(87).

Under mass transport limited conditions, the rotation of a screw dislocation results in the formation of dendrites(87). The screw dislocation forms a protrusion, grows under mass transport control until it reaches a critical radius of curvature, and then shoots up quickly under activation control. Despic and co-workers(87) identified two critical parameters for dendrite growth: (1) the overpotential to change the radius of curvature under mass transport control, and (2) the overpotential to rotate a screw dislocation.

Wranglen(88) performed an in-situ study of the growth and branching habits of several types of dendrites, using a cell mounted on a microscope. Using x-ray diffraction, he measured the crystallographic orientation of the electrodeposited dendrite and its branches and found that the branching of dendrites is directly related to the crystallography of the lattice defects. In tin dendrites, a twin relationship between the dendrite and its branches was found, indicating that branching occurred because of partial dislocations upon which metal deposited. The growth of branched dendrites in other metals showed other definite orientation relationships, showing that stacking considerations are a factor in dendrite branching.

In a heavily dislocated electrodeposit, interactions between growing defects can result in changes in the morphology, which are dependent on the dislocation type and the sign of the Burgers vector. Budevski(89) wrote that two interacting dislocations with the same Burgers

vector will form a single defect with a correspondingly increased Burgers vector. If the signs of the defects' Burgers vectors are reversed, a step bounded by the dislocations is formed. If this kink is small, it will be inactive for growth; however, nucleation will still be favored at that site. In large steps, dislocations can form loops, which are favored for both growth and nucleation. A dissociating defect can cause dramatic changes in the microstructure depending on the Burgers vectors and the angles of the resulting partials. All sites will be active for both growth and nucleation; twinning can also result.

Defects are clearly important in the metal deposition process, and any morphological study should include their effects. When performing electrolysis, defects are easily created, since most processes use both additives and foreign substrates. The rate of nucleation and growth at these sites is greatly enhanced, and once protrusions achieve a critical size, they can influence the hydrodynamic and concentration fields, causing morphological havoc. The instability of these surface perturbations can cause large scale morphological phenomena.

Figure captions

A-2.1(a) Interface between substrate and electrodeposit

A-2.1(b) Interface between two protrusions

A-2.1(c) Lattice distortions around an impurity atom

A-2.2 Differences between crystallization processes and electrocrystallization processes: (a) crystallization; (b) electrocrystallization, after (7)

A-2.3 Pinning of a crystal by a dislocation

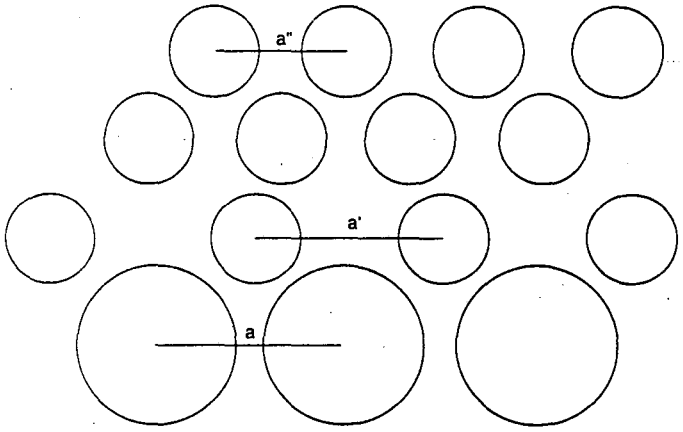

(a)

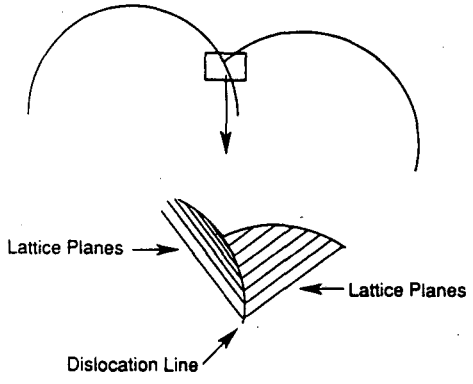

(b)

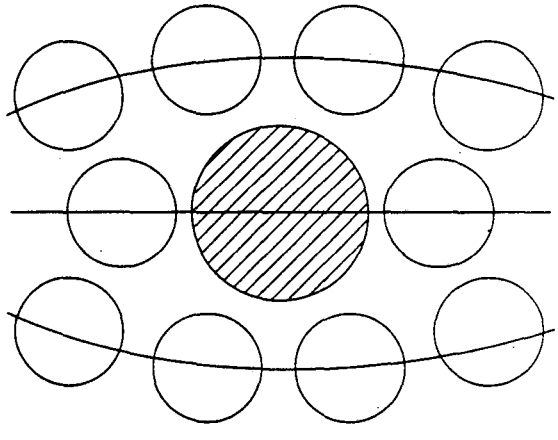

(c)

XBL 9012-4788 A

Figure A-2.1

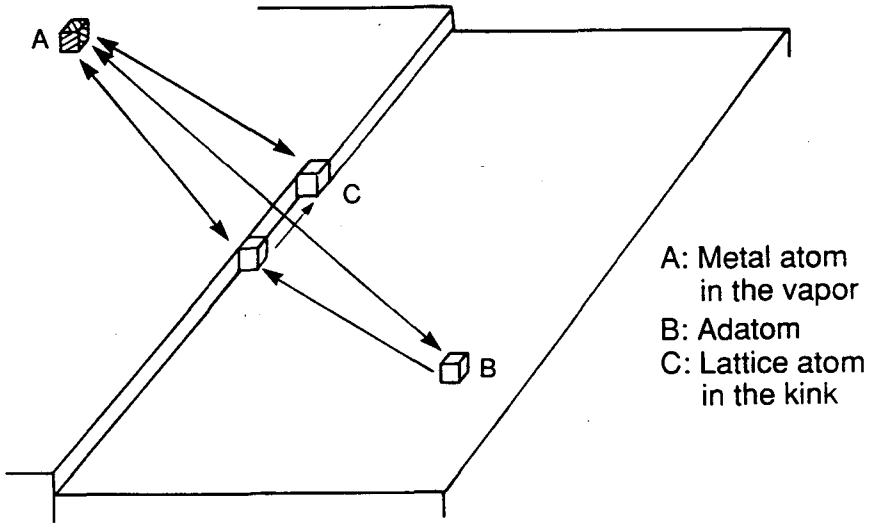

(a)

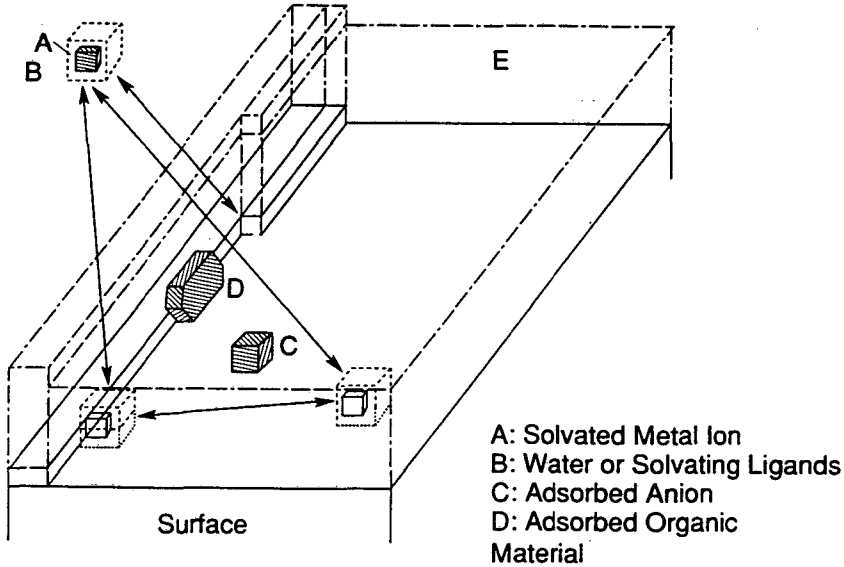

(b)

XBL 906-6421 A

Figure A-2.2

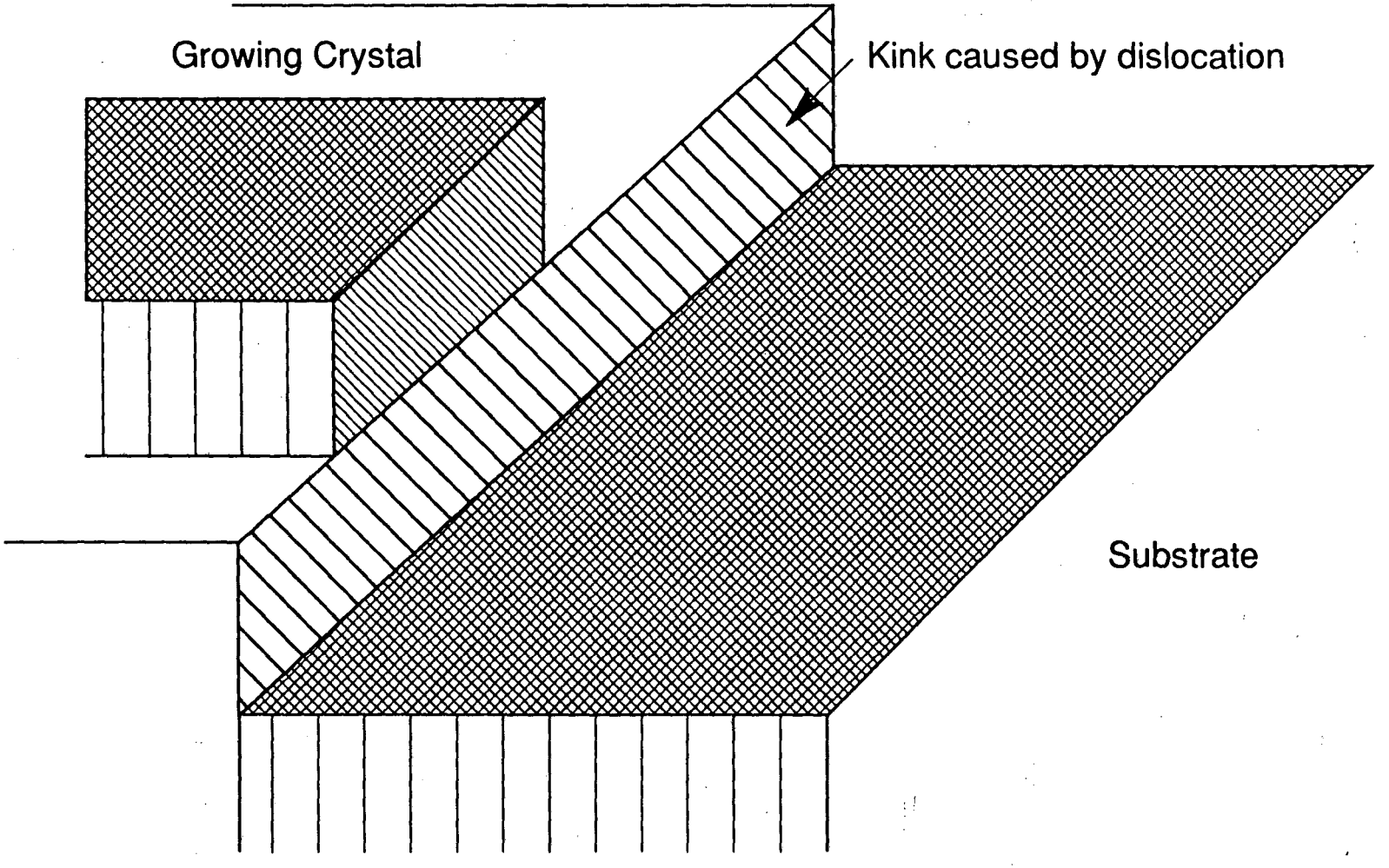

Figure A-2.3

XBL 9012-4791

APPENDIX 3- THE GENERATION OF CADMIUM SPONGE

Barnard, Edwards, Holloway and Tye(90) performed an extensive study of cadmium deposition on a nickel substrate using both acidic and alkaline electrolytes. For overpotentials above -250 mV, the deposit was initially smooth; however, sponge developed after a latent period of between 1 and 3 hours. The appearance of moss corresponded to a change in the slope of the current/time curve, and it was concluded that the mode of nucleation became progressive.

Barnard and co-workers (90) hypothesized that cadamate, $Cd(OH)_4^{-2}$, might be trapped in the crevices of the growing crystal, causing blocking of the electrode surface and subsequent moss formation. Even though a concurrent study (90) confirmed that small amounts of suspended cadamate greatly enhanced the growth rate of moss, the authors later concluded that the amount of dissolved cadamate was not sufficient to cause a change in morphology.

Using a stationary, cadmium sulfate electrolyte, Popov and co-workers (91) plated cadmium onto a copper wire substrate under potentiostatic conditions. They found that three morphological types were obtained depending on the magnitude of the overpotential. As the current density declined, the morphology progressed from dendritic, to spongy, to needlelike. No induction time was observed for the initiation of spongy electrodeposits; this type of morphology appeared before the copper surface was completely covered with cadmium. The authors concluded that mixed control is required for spongy deposits to form: at lower overpotentials, needlelike deposits were initiated, while when spherical diffusion conditions prevailed, dendrites were produced.

Henderson and Ladan(92) described a method by which cadmium sponge could be produced from chloride electrolytes. The deposit morphology was a function of current density, pH, plating bath composition, and temperature. X- ray diffraction indicated that the sponge was in the hcp orientation and had no oxide inclusions.

Wranglen(10) performed an extensive study of spongy and powdery deposition concentrating on metals that deposit with a low overvoltage: silver, lead , zinc, and cadmium. Under free convection, cadmium deposited in the mossy form when low current densities, high temperatures and neutral electrolytes were used. When spongy cadmium was produced, the non-compact layer initially covered the upper part of the cathode, the area of lowest current density and then spread to higher current density areas. Increasing the temperature caused the mossy cadmium layer to appear sooner.

Although there is some controversy over the nature of cadmium sponge, certain facts are well established. Mossy cadmium forms at both high and low current densities, the former being the result of depletion of cadmium ions near the electrode. The nature of the anion is not a factor in determining whether sponge will form, although the level of alkalinity of the electrolyte is crucial. As indicated by the current transients, nucleation on the electroplated cadmium surface is progressive once moss is initiated. The moss is polycrystalline and shows no signs of oxide inclusions. Because zinc and cadmium are chemically very similar metals, both being of the hcp structure with an elongated c- axis and both having the same outer shell configuration, one would expect that the same facts would be true of zinc moss.

APPENDIX 4- CALCULATIONS OF TRANSPORT PROPERTIES

In the rotating cylinder system, the limiting current density was calculated using the equation of Eisenberg and Tobias (48):

$$i_l = 0.0791 \frac{nFD_{Zn(OH)_4^{-2}}C_b}{d_i} Re^{0.7} Sc^{0.356} \qquad \text{(A4-1)}$$

where :

$$Re = \Omega\frac{d_i^2}{2\nu}, \quad \text{and} \quad Sc = \frac{\nu}{D_{Zn(OH)_4^{-2}}} \qquad \text{(A4-2, A4-3)}$$

The Schmidt number in equation (A4-1) is calculated using values for the diffusion coefficient and the kinematic viscosity obtained from Mc Breen(1) and the Handbook of Chemistry and Physics (93). The approximate value of this dimensionless parameter is 6500.

To determine the type of flow in the rotating cylinder cell, two dimensionless numbers are necessary. The Taylor number, a modification of the Reynolds number, is given by:

$$Ta = Re^2\left(\frac{r_o - r_i}{r_i}\right) \qquad \text{(A4-4)}$$

The diffusion boundary layer thickness is given by the expression:

$$\delta = \frac{nFD_{Zn(OH)_4^{-2}}C_b}{i_l} \qquad \text{(A4-5)}$$

Table 1 shows the magnitudes of all of the transport properties for the range of flow rates used in this study.

In the channel flow cell, the limiting current was calculated using Landau's correlation (94) for laminar flow:

$$i_l = 1.85\frac{nFD_{Zn(OH)_4^{-2}}C_b}{d_h}(ReSc\frac{d_h}{l})^{0.333} \qquad \text{(A4-6)}$$

where:

$$Re = \frac{d_h \rho V}{\mu} \qquad \text{(A4-7)}$$

and d_h, the hydraulic diameter, is defined as

$$d_h = \frac{4S}{l_p} \qquad \text{(A4-8)}$$

where l_p is the perimeter of the cell, 2.6 cm. The value of the hydraulic diameter was 0.46 cm.

The fraction of charge carried by a particular species is given by the transference number shown in equation A4-9:

$$t = \frac{n_i c_i \lambda_i}{\Sigma n_i c_i \lambda_i} \qquad \text{(A4-9)}$$

For the range of experimental conditions investigated, the transference number of the zincate species was very close to zero, and most of the charge was transported by the hydroxide

species. There was minimal variation in the transference number with KOH concentration.

Table 1- Calculated Transport properties*

Rotation Rate	i_l, mA/cm^2	δ, μm	Re	Ta	Sc
100	24	135	120	62000	6570
250	45	72	275	390000	6570
400	63	51	482	987830	6570
500	72	45	548	1552887	6570
750	98	33	900	3500000	6570
1000	156	20	1646	14000000	6570

*0.5 M ZnO, 6 M KOH, rotating cylinder cell

APPENDIX 5- MODIFICATIONS TO THE VIDEOMICROSCOPY SYSTEM

The videomicroscopy system was modified after the completion of the work by Mc Vay et al.(50) to achieve a better current distribution and higher magnification. The microscopy system consisted of the flow cell, the flow cell cover, and a dual eyepiece microscope. Illumination was provided using a fiber optic lamp. Attached to one eyepiece was a videocamera that transmitted images to a videorecorder and a monitor that displayed the progress of deposition during the experiment.

When the flow cell was redesigned to achieve higher magnifications, the channel depth was narrowed from 0.6 to 0.3 cm. At that time, a cell cover that would accommodate a glass window was machined. The glass window was necessary because a total microscope to electrode distance of no more than 5.6 mm was required and better transmission of light was also desired. The higher resolution was achieved by using a 50x long working distance objective lens with a numerical aperture of 0.6 and a working distance of 5.6 mm. (Normal objective lenses of this magnification have working distances of 0.4 mm (51).) Using this lens, a maximum magnification of 250X was attained without loss of picture quality.

To take videotapes, the video camera was mounted at the eyepoint of the microscope; for more information on this theory see (50). The videotapes were recorded in real time and after the experiment were edited to show the salient features of the deposition process. Alternatively, two videorecorders were used to observe the experiment; one recording in real time and the other using the time lapse mode.

NOMENCLATURE

A	Profile Amplitude (cm)
C	concentration (M/cm^3)
D	diffusivity (cm^2/s)
d_h	hydraulic diameter (cm)
d_i	inside diameter (cm)
d_o	outside diameter (cm)
F	Faraday constant (96480 C/equivalent)
i	current density (A/cm^2)
i_a	average current density (A/cm^2)
i_l	limiting current density (A/cm^2)
i_o	exchange current density (A/cm^2)
J	Nucleation rate
l	characteristic length (cm)
l_p	wetted perimeter (cm)
n	charge per ion (equivalents/mole)
N	number of ordinates chosen in a profile length
N_{OH^-}	flux of hydroxide ion, $mole/cm^2$-sec
$N_{Zn(OH)_4^{-2}}$	flux of zincate ion, $mole/cm^2$-sec
R	Gas Constant (8.314 Joule/mole-K)
R_a	average roughness
R_q	root mean square roughness
Re	Reynolds number
Sc	Sherwood number

S	cross sectional area (cm)
Ta	Taylor number
t_i	induction time (s)
t	transference number
V	Velocity (cm/s)
V_m	molar volume (cm^3/g)
x, y	position coordinates parallel to average surface
z	position coordinate normal to average surface
z_s	value of z at surface

Greek Letters

α	charge transfer coefficient
δ	nernst diffusion layer thickness
η	overpotential
κ	solution conductivity
λ	spatial period
μ	viscosity (centipoise)
ν	kinematic viscosity (cm^2/s)
ϕ	potential (volts)
ω	spatial frequency
Ω	rotation rate (radians/s)

Subscripts

a	activation
b	bulk
c	concentration
i	interface
n	nucleation
r	ohmic
s	surface

Superscripts

o	flat surface
p	perturbation magnitude

REFERENCES

1. Mc Breen, J. and E. Cairns, *The Zinc Electrode,* in *Advances in Electrochemistry and Electrochemical Engineering,* H. Gerisher and C. W. Tobias, eds., Volume 11, John Wiley and Sons, New York, 1978, p. 273.

2. Oswin, H. G. and K. F. Blurton, *The morphology of zinc electrodeposited from alkaline electrolytes,* in *Zinc/ Silver Oxide Batteries,* A. Fletcher, ed. with John Lander, John Wiley and Sons, NY, 1971, p. 63.

3. Cotton, F. A. and G. Wilkinson, *Advanced Inorganic Chemistry,* 4th edition, Chapter 18, Wiley, New York, (1980).

4. Mathewson, C. H., *Zinc, the Science and Technology of the Metal, its Alloys and Compounds,* ACS monograph series no. 142, Reinhold Publishing Co., New York, 1959.

5. Bard, A. J. ed., *Encyclopedia of the Electrochemistry of the Elements,* Vol. 5, Marcel Dekker, NY, 1976

6. Achmetow, N. S. and G. S. Wosdwishenskij, *Zh. Priklad. Khim., 29(8),* 1196, (1956).

7. Fischer, H., *Angew. Chem. Int. Edit., 8(2),* 108, (1969).

8. Burgess, C. F. and C. Hambuechen, *Electrochemical Industry, 1(6),* 204, (1903).

9. Arouete, S., K. F. Blurton, and H. G. Oswin, *JES, 116(2),* 166, (1969).

10. Wranglen, G., *JES, 97(11),* 353, (1950).

11. Ibl, N., *Applications of mass transfer theory: The formation of powdered metal deposits,* in *Advances in Electrochemistry and Electrochemical Engineering,* C. W. Tobias, ed., John Wiley and Sons, NY, 1962, p. 49.

12. Naybour, R. D., *Electrochim. Acta., 13,* 763, (1968).

13. Naybour, R. D., *JES, 116(4),* 520, (1969).

14. Mc Breen, J., E. Gannon, D. T. Chin, and R. Sethi, *JES, 130(8),* 1641, (1983).

15. Kudryavtsev, N. T. and A. A. NIkiforova, *Zh. Prikl. Khim., 22(4),* 367, (1949).

16. Kudryavtsev, N. T., *Zh. Fiz. Khim., 26,* 270, 81, (1952).

17. Kudryavtsev, N. T., *Tr. Soveshchaniyapo Elektrokhim. Akad. Nauk SSSR, Otd. Khim. Nauk,* 258, (1953).

18. Kudryavtsev, N. T., R. Yu. Bek, and I. F. Kushevich, *Tr. Noskov. Khim. Tekhnol. Inst. D. I. Mendeleeva, 22,* 137, (1956).

19. Kudryavtsev, N. T., R. Yu. Bek, and I. F. Kushevich, *Zh. Prikl. Khim., 30,* 1093, (1957).

20. Epelboin, I., M. Kasouri, and R. Wiart, *J. Electroanal. Chem., 58,* 488, (1975).

21. Epelboin, I., M. Kasouri, and R. Wiart, *J. Electroanal. Chem., 65,* 373, (1975).

22. Tsuda, T. and C. W. Tobias, *The Influence of Lead Ions on the Macromorphology of Electrodeposited Zinc,* M. S. Thesis, University of California, Berkeley, September, 1981, LBL report no. 21497.

23. Popov, K. I., D. N. Keca, and M. D. Andjelic, *J. Appl. Electrochem., 9,* 19, (1978).

24. Popov, K. I. and N. V. Krstajic, *J. Appl. Electrochem., 13,* 775, (1983).

25. Popov, K. I., N. V. Krstajic, S. R. Popov, and M. I. Cekerevac, *J. Appl. Electrochem., 16,* 771, (1986).

26. Cachet, C., U. Stroder, and R. Wiart, *E. Acta., 27(7),* 903, (1982).

27. Cachet, C., Z. Chami, and R. Wiart, *E. Acta., 32(3),* 465, (1987).

28. Cachet, C., B. Saidani, and R. Wiart, *E. Acta., 33(3),* 405, (1988).

29. Hugot- Le Goff, A., S. Joiret, B. Saidani, and R. Wiart, *J. Electroanal. Chem., 263,* 127, (1989).

30. Cachet, C., B. Saidani, and R. Wiart, *JES, 138(3),* 678, (1991).

31. Vorkapic, L. Z., D. M. Drazic, and A. R. Despic, *JES, 121,* 1385, (1974).

32. Hamnet, A. and R. J. Mortimer, *J. Electroanal. Chem., 234,* 185, (1987).

33. Mullins, W. W. and R. F. Sekerka, *J. Appl. Physics, 35,* 444, (1964).

34. Sekerka, R. F., *J. Appl. Physics, 36,* 264, (1965).

35. Mullins, W. W. and R. F. Sekerka, *J. Appl. Physics, 34,* 323, (1963).

36. *Roughness Evolution and Dendritic Growth in Zinc Electrodeposition from Halide Electrolytes.* EPRI report EM-2937, March, 1983.

37. Aogaki, R., K. Kitazawa, Y. Kose, and K. Fueki, *Electrochim. Acta, 25,* 965, (1980).

38. Aogaki, R. and T. Makino, *Electrochim. Acta, 26,* 1509, (1981).

39. Barkey, D. and C. W. Tobias, *Studies on High Speed Electroforming,* PhD Thesis, University of California, Berkeley, LBL report no. 23880, August, 1987.

40. Barkey, D. and C. W. Tobias, *JES, 136(8),* 2199, (1989).

41. Barkey, D. and C. W. Tobias, *JES, 136(8),* 2207, (1989).

42. Farr, J. P. G. and N. A. Hampson, *J. Electroanal. Chem. and Interfacial Chem., 181,* 433, (1967).

43. Farr, J. P. G. and N. A. Hampson, *J. Electroanal. Chem. and Interfacial Chem., 181,* 407, (1968).

44. Bockris, J. O'M., Z. Nagy, and A. Damjanovic, *JES, 119(8),* 285, (1972).

45. Dirkse, T. P., *JES, 120(9),* 1456, (1979).

46. Isaacson, M., F. R. Mc Larnon, and E. J. Cairns, *JES, 137(7),* 2014, (1990).

47. Isaacson, M., F. R. Mc Larnon, and E. J. Cairns, *JES, 137(8),* 2361, (1990).

48. Newman, J.. *Electrochemical Systems.* Prentice Hall, NJ, 1973.

49. Faltemeier, J. and C. W. Tobias, *The Effect of Hydrodynamic Flow on the Morphology of Electrodeposited Zinc,* PhD Thesis, University of California, Berkeley, LBL report no. 16485, August, 1983.

50. Mc Vay, L, R. H. Muller and C. W. Tobias, *Studies of Micromorphology and Current Efficiency of Zinc Electrodeposited from Flowing, Chloride Electrolytes,* M. S. Thesis, University of California, Berkeley, May, 1986, LBL report no. 21497.

51. Richardson, J. H.. *Optical Microscopy for the Material Sciences.* Marcel Dekker Inc., NY, 1971.

52. Justinijanovic, I. N. and A. R. Despic, *Electrochim. Acta., 18,* 709, (1973).

53. Pangaroff, N. A., *E. Acta., 9,* 721, (1964).

54. Mackinnon, D. J., R. M. Morrision, J. E. Maitland, and P. E. Warren, *J. Appl. Electrochem, 20,* 728, (1990).

55. Kindler, A. *The Morphology of Electrodeposited Copper,* PhD Thesis, University of California, Berkeley, LBL report no. 12838, November, 1981.

56. *Surface Texture (Surface Roughness, Waviness, and Lay)* ANSI/ASME Standard B46.1-1985, The American Society of Mechanical Engineers, NY, NY, 1985.

57. Cullity, B. D., *Elements of X-ray Diffraction,* Addison-Wesley publishing Corp. Reading, Mass., 1959.

58. Putt, Ron, in *Technology Base Research Project, Quarterly Report, 1 st. Quarter, FY, 1991.*

59. Mayer, S. T. and R. H. Muller, *An In Situ Study of the Anodic Film Formation of Cu, Ag, and Zn in Alkaline Media,* PhD Thesis, University of California, Berkeley, LBL report no. 28085, December, 1989.

60. Fischer, H., *The nucleation dependent growth layer: A structure element in electrocrystallization,* presented to the 56 th annual convention of the American Electroplaters Society, Detroit, Michigan, June 16, 1969.

61. Grahame, D. C., *Chemical Reviews, 41,* 441, (1947).

62. Jordan, K. J. *Levelling of Microprofiles in Electrodeposition,* PhD thesis, University of California, Berkeley, LBL report no. 29924, December, 1990.

63. Kruglikov, S. S., N. T. Kurdriavtsev, and A. Y. Antonov, *Electrochim. Acta., 10,* 253, (1965).

64. Barkey, D. and P. D. Laporte, *JES, 137,* 1655, (1990).

65. Barkey, D., P. Garik, E. Ben-Jacob, B. Miller, and B. Orr, *JES,* to be published.

66. Dukovic, J. O. and C. W. Tobias, *Studies on Current Distribution in Electrochemical Cells,* PhD thesis, University of California, Berkeley, LBL report no. 22084, August, 1986.

67. Blurton, K. F. and A. Sammels *J. Power Sources, 4,* 263, (1979).

68. Ross, P. N. Jr., *Feasibility Study of a New Zinc/Air Battery Concept Using Flowing Alkaline Electrolyte,* LBL report 21437, April, 1986.

69. Foller, P. *J. Appl. Electrochem., 16(4),* 527, (1986).

70. Marshall, A., N. A. Hampson and J. S. Drury *Electroanal. Chem. and Interfacial Electrochem., 59,* 19, (1975).

71. Jorne, J., *Amer. Scientist, 71(5),* 507, (1983).

72. Hattori, S., M. Yamaura, C. Kawamura and S. Yoshida, *A New Design for the Rechargeable Zinc/Air Battery,* in *Proceedings of the 31 st Power Sources Symposium,* 11-14 June, 1984, published by the Electrochemical Society,

73. Appelby, A. J. and M. Jacquier, *J. Power Sources, 1,* 17, (1976-77).

74. Powers, M. J., K. F. Blurton and A. Sammels, Extended Abstracts Electrochemical Society, 10/79, Los Angeles, Abstract 117.

75. Kinoshita, K., personal communication.

76. Dupperray, G., G. Marcellin and B. Pichon, *Recent Advances in Secondary Zinc/Air batteries,* in *Power Sources 8- Research and Development in Non-mechanical Electrical Power Sources,* J. Thompson, ed., Academic Press, New York, 1981.

77. Katan, T., P. J. Carlen, and S. Szpak, *JES, 133(7),* 1340, (1986).

78. Selman, J. R. and H. Wu, *Mass Transfer and Current Distribution in a Zinc/Redox Battery Flow Cell,* presented at the 1984 Annual meeting of the American Institute of Chemical Engineers, San Franscisco, Ca., November 28, 1984.

79. Mc Breen, J., *J. Electroanal. Chem., 168,* 415, (1984).

80. Weil, R., *Plating and Surface Finishing, 69(12),* 46, (1982).

81. Mc Breen, J., M. G. Chu and G. Adsic, *JES, 128(11),* 2287, (1981).

82. Lamb, V., C. E. Johnson, and D. R. Valentine, *JES 117(9),* 291C, (1970).

83. Franck, F. C., *Disc. Faraday Soc., 5,* 48, (1949).

84. Gilmer, G. H., *Science, 208(4442),* 355, (1980).

85. Bressan, J. and R. Wiart, *J. Appl. Electrochem., 9,* 4953, (1979).

86. Bockris, J. O'M., Z. Nagy and D. Drazic, *JES, 120(1),* 30, (1973).

87. Diggle, J. W., A. R. Despic and J. O'M Bockris, *JES, 116(11),* 1503, (1969).

88. Wranglen, G., *E. Acta. 2,* 130, (1960).

89. Budevski, E., *Deposition and Dissolution of Metals and Alloys,* in *Comprehensive Treatise on Electrochemistry,* volume 7, J. O'M Bockris, B. E. Conway, E. Yeager, R. E. White eds., Plenum Press, NY, 1984.

90. Barnard, R., G. S. Edwards, J. Holloway and F. L. Tye, *J. Appl. Electrochem., 13(6),* 756, (1983).

91. Popov, K. I., N. V. Krstajic, and S. R. Popov, *J. Appl. Electrochem., 15(1),* 151, (1985).

92. Henderson, I. H. S. and S. G. Ladan, *Can. J. Chem. Eng., 46(10),* 355, (1968).

93. Weast, R. C., ed. *The Handbook of Chemistry and Physics.* 65th edition, CRC Press, Boca Raton, FL, 1984.

94. Landau, U. and C. W. Tobias, *Distribution of Mass Transport Rates along Parallel Plane Electrodes in Forced Convection,* PhD Thesis, University of California, Berkeley, LBL report no. 2702, January, 1976.

LAWRENCE BERKELEY LABORATORY
UNIVERSITY OF CALIFORNIA
INFORMATION RESOURCES DEPARTMENT
BERKELEY, CALIFORNIA 94720